



Liu, Zhaowei (2018) *An isogeometric coupled boundary element method and finite element method for structural-acoustic analysis through loop subdivision surfaces*. PhD thesis.

<https://theses.gla.ac.uk/38988/>

Copyright and moral rights for this work are retained by the author

A copy can be downloaded for personal non-commercial research or study, without prior permission or charge

This work cannot be reproduced or quoted extensively from without first obtaining permission in writing from the author

The content must not be changed in any way or sold commercially in any format or medium without the formal permission of the author

When referring to this work, full bibliographic details including the author, title, awarding institution and date of the thesis must be given

Enlighten: Theses

<https://theses.gla.ac.uk/>
research-enlighten@glasgow.ac.uk

**An Isogeometric Coupled Boundary Element Method and
Finite Element Method for Structural-acoustic Analysis
through Loop Subdivision Surfaces**

Zhaowei Liu

Submitted in fulfilment of the requirements for the
Degree of Doctor of Philosophy

School of Engineering
College of Science and Engineering
University of Glasgow



University
of Glasgow

December 10, 2018

Abstract

This present thesis proposes a novel approach for coupling finite element and boundary element formulations using a Loop subdivision surface discretisation to allow efficient acoustic scattering analysis over shell structures. The analysis of underwater structures has always been a challenge for engineers because it couples shell structural dynamics and acoustic scattering. In the present work, a finite element implementation of the Kirchhoff-Love formulation is used for shell structural dynamic analysis and the boundary element method is adopted to solve the Helmholtz equation for acoustic scattering analysis. The boundary element formulation is chosen as it can handle infinite domains without volumetric meshes.

In the conventional engineering workflow, generating meshes of complex geometries to represent the underwater structures, e.g. submarines or torpedoes, is very time consuming and costly even if it is only a data conversion process. Isogeometric analysis (IGA) is a recently developed concept which aims to integrate computer aided design (CAD) and numerical analysis by using the same geometry model. Non-uniform rational B-splines (NURBS), the most commonly used CAD technique, were considered in early IGA developments. However, NURBS have limitations when used in analysis because of their tensor-product nature. Subdivision surfaces discretisation is an alternative to overcome NURBS limitation. The new method adopts a triangular Loop subdivision surface discretisation for both geometry and analysis. The high order subdivision basis functions have C^1 continuity, which satisfies the requirements of the Kirchhoff-Love formulation and are highly efficient for the acoustic field computations. The control meshes for the shell analysis and the acoustic analysis have the same resolution, which provides a fully integrated isogeometric approach for coupled structural-acoustic analysis of shells. The method is verified by the example of an acoustic plane wave

which scatters over an elastic spherical shell. The ability of the presented method to handle complex geometries is also demonstrated.

Contents

Abstract	i
List of Symbols	xiv
Acknowledgements	xvii
Declaration	xviii
1 Introduction	1
1.1 Acoustic scattering in engineering applications	1
1.2 Numerical methods for coupled structural-acoustic analysis	2
1.3 Integrated CAD and numerical analysis for underwater structures	4
1.4 Novel contributions	7
1.5 Manuscript organisation	7
2 A review of isogeometric analysis	9
2.1 Isogeometric concept	9
2.2 Challenges of isogeometric analysis	12
2.2.1 Complex geometry with arbitrary topology	13
2.2.2 Local refinement and adaptivity	13
2.2.3 Volumetric discretisation	13
2.3 Working with industrial CAD geometries	14
2.3.1 Conforming and non-conforming patches	15
2.3.2 Trimmed CAD surfaces	17

2.4	Analysis suitable CAGD techniques for IGA	18
2.4.1	T-splines	19
2.4.2	Hierarchical B-splines	21
2.4.3	PHT-splines	22
2.4.4	LR B-splines	23
2.4.5	Subdivision surfaces	23
2.5	Volume parameterisation and surface-based IGA formulations	24
2.5.1	Volumetric spline parameterisation	24
2.5.2	Isogeometric shell formulations	26
2.5.3	Isogeometric boundary element method	27
2.6	Summary	30
3	CAGD fundamental techniques	31
3.1	B-splines and NURBS	31
3.1.1	B-spline curves	31
3.1.2	Non-Uniform Rational B-Splines curves	34
3.1.3	NURBS surfaces	36
3.1.4	Refinement	37
3.1.5	Bézier extraction	40
3.2	Subdivision curves and surfaces	44
3.2.1	Curves	45
3.2.2	Catmull-Clark subdivision surfaces	49
3.2.3	Loop subdivision surfaces	53
3.2.4	Evaluation of Loop subdivision surfaces	55
3.2.5	Comparison of subdivision with NURBS surfaces	63
4	Boundary element method for acoustics	65
4.1	Fundamentals of linear acoustic analysis	67
4.1.1	Acoustic pressure and acoustic velocity	67
4.1.2	Helmholtz equation	68

4.1.3	Helmholtz fundamental solution	68
4.2	Acoustic boundary element method	71
4.2.1	Boundary integral equation for the Helmholtz equation	71
4.2.2	Acoustic boundary conditions	77
4.2.3	Discretisation of the boundary integral equation	77
4.3	Boundary element method with subdivision surfaces	79
4.3.1	Collocation approach	79
4.3.2	Derivation of system of equations	82
4.3.3	Acceleration methods	82
4.3.4	Evaluation of element integrals	83
4.3.5	Non-uniqueness problem and the Burton-Miller method	85
4.4	Singular integration	86
4.4.1	Weakly-singular integrals: polar coordinate transformation	86
4.4.2	Strongly-singular integrals	90
4.4.3	Hyper-singular integrals	91
4.5	Numerical verification	93
4.5.1	Plane wave scattered by a rigid sphere	93
4.5.2	Acoustic wave scattered by a mannequin model	100
5	A coupled isogeometric boundary element and finite element method for two-way structural-acoustic coupling analysis using subdivision surfaces	105
5.1	Shell structural dynamic analysis using Kirchhoff-Love theory	106
5.2	Coupled structural-acoustic formulation	110
5.3	Numerical examples	114
5.3.1	Plane wave scattered by an elastic spherical shell	114
5.3.2	Acoustic wave scattered by a submarine	129
5.3.3	Acoustic wave scattered by a geometry with complex topology	135
6	Conclusions	139
6.1	Summary	139

6.2	Key findings	140
6.3	Future work	141

List of Tables

- 4.1 Integral errors after polar coordinates transformation 90
- 4.2 Mesh properties for subdivision refinement 96
- 4.3 Mesh properties for subdivision refinement and subsequent L_2 projection . . . 96
- 4.4 Mesh properties for Lagrangian discretisation 99
- 4.5 Runtime and memory usage for assembling and storing matrix \mathbf{H} using hierarchical matrices in two mannequin model tests 103

- 5.1 Default material and geometry parameters settings in the structural-acoustics problem. 116
- 5.2 Maximum pointwise errors calculated through Equation 5.19 for a set of increasing normalised wavenumbers applied to the coupled sphere problem. The numbers in parentheses indicates the approximate number of elements per wavelength. A dash indicates a result with a large maximum pointwise error that indicates insufficient resolution of mesh for the given wavenumber. 124

List of Figures

2.1	(a) Conventional workflow. (b) Isogeometric analysis workflow.	10
2.2	An example B-spline mapping from parametric domain to physical domain. Figure is reproduced from [1].	12
2.3	(a) Example of non-conforming patches. (b) Example of conforming patches. . .	16
2.4	An example of a trimmed CAD surface.	18
2.5	An example T-spline control mesh.	20
2.6	(a) A complex CAD model of a hand. (b) Visible gaps existed between two NURBS control grids. (c) A watertight T-mesh conforms NURBS patches. Figure is reproduced from [2].	21
2.7	Construction of a hierarchical B-spline: initial basis functions (above), refined basis functions (middle) and combinations of two levels of basis functions (below). Figure is reproduced from [3].	22
2.8	An example hierarchical T-mesh.	23
2.9	(a) A triangular surface mesh of a CAD model. (b) The mapped parametric triangular mesh on a cube. (c) The subdivision result for the parametric cube. (d) Constructing the model with T-mesh and T-spline for the geometry. (e) Applying Bézier extraction on the T-splines. Figure reproduced from [4].	26
2.10	IGA workflow using BEM.	28
3.1	An example B-spline curve	33
3.2	Quadratic basis functions for the B-spline curve.	33
3.3	A comparison between a B-spline and a NURBS curve	36

3.4	An example of a NURBS surface.	37
3.5	An example of h -refinement of NURBS.	39
3.6	An example of p -refinement of NURBS.	40
3.7	An example Bézier extraction of a B-spline curve	41
3.8	Plots of piecewise Bézier basis functions of the curve shown in Figure 3.7.	41
3.9	Mapping from Bézier element integration domain to NURBS parametric domain.	44
3.10	Chaikin's Algorithm	46
3.11	Computing new control points through the Catmull-Clark algorithm.	47
3.12	Catmull-Clark Algorithm	48
3.13	Computing refined control mesh through the Catmull-Clark algorithm.	50
3.14	The weight distribution for computing different types of new control points.	52
3.15	Catmull-Clark subdivision algorithm applied to an initial cube control mesh.	52
3.16	Weight distributions for computing an extraordinary point with valence κ	53
3.17	Computing refined control mesh through the Loop subdivision algorithm for a regular vertex.	55
3.18	A regular patch for an element in Loop subdivision surfaces.	55
3.19	A regular patch with ghost points for an element in Loop subdivision surfaces.	56
3.20	Barycentric coordinate of a triangular element.	57
3.21	An irregular patch for an element in Loop subdivision surfaces.	59
3.22	Refinement of an element with one extraordinary vertex.	59
3.23	Refined element patch and sub-patches for the sub-element 1, 2 and 3.	60
3.24	Successive refinements of the parametric domain for evaluating an irregular element.	62
4.1	The source point is contained by a small sphere with radius ε to avoid singularity.	73
4.2	The source point is moved onto the boundary and it is surrounded by a semi-circle.	75
4.3	Definition of interior and exterior domains.	76

4.4	Illustration of a control mesh and associated limit surface for a regular patch using the Loop subdivision scheme. Control vertices are located in the control mesh at the intersection of edges and collocation points are defined as the corresponding points on the limit surface. The collocation points of the centre element specified by the set C_e are denoted by red circles. It is important to note that control vertices and collocation points do not coincide.	81
4.5	Mapping of the reference triangle to the triangle on the subdivision surface. x^e denotes the mapping operation.	84
4.6	Subdivision for Polar coordinate transformation (If the singular point is located at one of the corners, divide the element through the diagonal line (left). If the singular point lies on one of the edges, divide the element into three triangle elements (middle). If the singular point lies in the element, the element will be divided into four triangular elements (right)).	87
4.7	The definitions of the variables in polar coordinates transformation for a standard quadrilateral element (left) and a triangular element in the Loop subdivision surfaces (right).	89
4.8	Definition of plane wave impinging on a sphere.	93
4.9	The initial coarse Loop subdivision discretisation with 438 vertices used to generate control meshes (a) through to (d) in Table 4.2 and Table 4.3. The control vertices are placed such that they lie on a sphere with diameter $a = 1$	95
4.10	The Loop subdivision discretisation of a sphere geometry with 6978 vertices corresponding to control mesh (d) in Table 4.3. The control vertex positions are determined such that the limit surface approximates a sphere with diameter $a = 1$	95
4.11	Rigid sphere scattering a plane wave with $\bar{k}a = 10$: surface acoustic potential magnitude along x - y plane using control meshes (a) and (b). The inset image illustrates convergence to a solution which does not correspond to the analytical solution due to the non-negligible geometrical error of the limit surface.	97

4.12	Rigid sphere scattering a plane wave with $\bar{k}a = 10$: surface acoustic potential magnitude along x - y plane using control meshes (c) and (d). L_2 projection of control vertices onto the analytical sphere surface leads to a reduced geometrical error in the limit surface and convergence to the analytical solution.	98
4.13	Sample points in acoustic domain.	99
4.14	A comparison between Lagrangian discretisations and subdivision surfaces ($k = 8$).	99
4.15	Mannequin problem: control grid with 2, 834 vertices. The minimum bounding box for this model and the refined model in Figure 4.16 is defined by $[x_i^{min}, x_i^{max}]^3 = [-179.0, 51.0] \times [-81.6, 92.4] \times [10.3, 294.0]$	101
4.16	Mannequin problem: control grid with 11, 330 vertices.	101
4.17	The smooth limit surface of the mannequin model generated through Loop subdivision. This limits surface is common to the control grids shown in Figures 4.15 and 4.16.	102
4.18	Mannequin problem: acoustic pressure profiles for the two considered Loop subdivision discretisations.	103
4.19	The set of bounding boxes used to define the block cluster tree for \mathcal{H} -matrix construction of the dense matrices (11, 330 vertices).	104
4.20	The low-rank approximation of the dense matrix \mathbf{H} for the control grid with 11,330 vertices. Dense and sparse entries are denoted by red and green respectively.	104
5.1	An example thin shell illustrates the definitions of thickness, mid-surface and the parametric coordinate system.	107
5.2	Reference and deformed configuration of the shell. \bar{x} and x are two mapping operators map the parametric representation of the mid-surface to its reference and deformed configurations. Figure reproduced from [5].	109

5.3	Definition of the structural thin shell and fluid domains for the coupled structural-acoustic problem impinged by an incident plane wave p_{inc} . The mid-surface of the shell is denoted by a dashed line. The structural domain normal vectors \mathbf{n}_s and the fluid domain normal vector \mathbf{n}_f are pointing opposite directions.	110
5.4	Coupled structural-acoustic problem of a plane wave impinged on a spherical shell immersed in an infinite fluid domain.	115
5.5	Spherical shell scattering study: incident wave direction and polar coordinate system defined in the x - y plane	115
5.6	Coupled spherical shell problem, $\bar{k}a = 10$: surface acoustic potential magnitude along x - y plane using control meshes (a) and (b). The inset illustrates convergence to a solution which does not correspond to the analytical solution due to the non-negligible geometrical error of the limit surface.	118
5.7	Coupled spherical shell problem, $\bar{k}a = 10$: surface acoustic potential magnitude along x - y plane using control meshes (c) and (d). L_2 projection of control vertices onto the analytical sphere surface leads to a reduced geometrical error in the limit surface and convergence to the analytical solution.	118
5.8	Acoustic pressure plots for the coupled sphere scattering problem with acoustically hard surface, $\bar{k}a = 6$. Shell displacements are equal to zero in this case.	120
5.9	Acoustic pressure and displacement plots for the coupled sphere scattering problem with $h = 0.1m$, $\bar{k}a = 6$. The displacements are enlarged in the figure (c) and (d).	121
5.10	Acoustic pressure and displacement plots for the coupled sphere scattering problem with $h = 0.05m$, $\bar{k}a = 6$. The displacements are enlarged in the figure (c) and (d).	122
5.11	Coupled sphere study: surface acoustic potential magnitude profile along x - y plane for $\bar{k}a = 30$, control mesh (c).	124
5.12	Coupled sphere study: surface acoustic potential magnitude along x - y plane for $\bar{k}a = 40$, control mesh (c).	125

5.13	Coupled sphere study: surface acoustic potential magnitude along x - y plane for $\bar{k}a = 50$, control mesh (d).	126
5.14	Coupled sphere study: surface acoustic potential magnitude along x - y plane for $\bar{k}a = 60$, control mesh (d).	126
5.15	Coupled sphere study: surface acoustic potential magnitude along x - y plane for $\bar{k}a = 80$, control mesh (d).	127
5.16	Coupled sphere study: $\text{Re}(p)$ (real component of acoustic pressure) for $\bar{k}a = 80$, control mesh (d).	128
5.17	Coupled sphere study: $\text{Im}(p)$ (imaginary component of acoustic pressure) for $\bar{k}a = 80$, control mesh (d).	128
5.18	Submarine problem: control mesh with 9, 510 vertices.	129
5.19	The smooth limit surface of the submarine model generated through Loop subdivision.	130
5.20	Submarine model: acoustic pressure magnitude profiles for both an acoustically hard surface and coupled shell formulation with a normalised wavenumber of $\bar{k}a = 46.15$, perspective view.	131
5.21	Submarine model: acoustic pressure magnitude profiles for both an acoustically hard surface and coupled shell formulation with a normalised wavenumber of $\bar{k}a = 46.15$, x - y plane.	132
5.22	Submarine model: acoustic pressure magnitude profiles for both an acoustically hard surface and coupled shell formulation with a normalised wavenumber of $\bar{k}a = 46.15$, x - z plane.	133
5.23	Submarine model: acoustic pressure magnitude on a sliced curve for both an acoustically hard surface and coupled shell formulation with a normalised wavenumber of $\bar{k}a = 46.15$, x - y plane.	134
5.24	Complex topology example: Loop subdivision discretisation with 3,940 vertices.	136
5.25	Coupled structural-acoustic analysis over a Loop subdivision surface with complex topology: acoustic pressure magnitudes for $\bar{k}a = 3.0$	137

List of Symbols

κ	valence of a vertex
p_{inc}	incident acoustic pressures
\mathbf{n}_s	normal vector for structure domain
\mathbf{n}_f	normal vector for fluid domain
ξ	knot vector
n_p	polynomial order
n_c	number of control points
\mathbf{S}	coordinates of a surface point
\mathbf{P}	coordinates of a control point
w	weight
\mathbf{P}_{iH}	homogeneous coordinates of the i^{th} control point
\mathbf{S}_H	homogeneous coordinates of the surface point
R	rational basis function
$\bar{\xi}$	refined knot vector
$\bar{\xi}_j$	j^{th} inserting knot
m	total number of variables
\mathbf{C}^j	operator matrix computes j^{th} inserting knot
\mathbf{B}	Bernstein polynomial functions
\mathbf{C}	Bézier extraction operator
\mathbf{P}_i	set of control points in i^{th} level of refinement
\mathbf{S}	subdivision operator
\mathbf{P}	set of control points

D	selection matrix
u	first barycentric coordinate
v	second barycentric coordinate
w	third barycentric coordinate
\mathbf{v}	acoustic velocity
t	time
\mathbf{u}	displacement
p	acoustic pressure
c	thermodynamic speed of sound
ω	angular frequency
i	imaginary unit
\bar{k}	acoustic wavenumber
G	Green's function
δ	Dirac delta function
r	distance/ radius
ϵ	infinitesimal radius
Ω	space
Γ	surface
F	force vector
ψ	arbitrary function 1
ϕ	arbitrary function 2
ξ, η	parametric coordinates
G, H	BEM matrices
p	global vector of the acoustic pressure coefficients
q	global vector of the acoustic pressure normal derivative coefficients
\mathbf{p}_{inc}	global vector of the incident acoustic pressures
$\mathbf{v}_1, \mathbf{v}_2$	two tangent vectors at the surface point
$\bar{\mathbf{u}}$	virtual displacement

W_{mas}	virtual work contributions of the inertia force
W_{int}	virtual work contributions of the internal force
W_{ext}	virtual work contributions of the external force
ρ_s	density of shell
μ	Jacobian for integration across the thickness
\mathbf{E}	constitutive tensor
α	change of the metric tensor
h	shell thickness
β	change of the curvature tensor
\mathbf{K}	global stiffness matrix
\mathbf{M}	global mass matrix
\mathbf{f}	global force vector
\mathbf{f}_s	global structure force vector
\mathbf{f}_f	global fluid force vector
\mathbf{N}	global vector of subdivision basis functions
$\tilde{\mathbf{n}}_f$	global vector of subdivision basis functions
$\mathbf{e}_1, \mathbf{e}_2, \mathbf{e}_3$	three Cartesian orthogonal base vectors
\mathbf{C}_{sf}	coupling matrix: fluid to structure
v_f^n	normal component of the fluid velocities
v_s^n	normal component of the structural velocities
ρ_f	fluid density
\mathbf{C}_{fs}	coupling matrix: structure to fluid
\mathbf{u}	global vector of nodal displacements
c_w	speed of sound
E	Young's modulus
ν	Poisson's ratio
M	plane wave magnitude

Acknowledgements

First and foremost I want to express my deep gratitude to my two supervisors. Dr. Robert Simpson was my primary supervisor in the first three years of my PhD study. It has been an honour to be his first and only PhD student. I would like to thank him for encouraging my research and for helping me develop my abilities to become a researcher in engineering. His advices on both my research and career are priceless. I should also express my sincere gratitude to Dr. Andrew McBride. He agreed to be my primary supervisor after Dr Robert Simpson left university. His guidance helped me go through the toughest moments in my PhD study. His comments on writing of this thesis are extremely valuable. This manuscript will not be finished without his help.

Besides my supervisors, I would like to thank Dr. Fehmi Cirak in the Computational Structural Mechanics Lab at the University of Cambridge. He provided me a great opportunity to work with the most talented scientists in a cutting-edge research area. Thanks also go to his student Dr. Musabbir Majeed for his contributions and stimulating discussions. I would also express my sincere appreciation to my examiners, Professor Ferri Aliabadii and Dr Peter Grassl for an intellectually stimulating and enjoyable viva.

Last but not least, I must express my special thanks to my family. Words cannot express how grateful I am to my mother and father for all of the sacrifices that they have made on my behalf. I would also like to thank all of my friends who supported me in writing, and encouraged me to strive towards my goal.

Declaration

I declare that this thesis has been composed solely by myself and that the work has not be submitted for any other degree or professional qualification. I confirm that the work presented is entirely my own, except where work which has formed part of a jointly-authored publication has been included. My contribution and those of the other authors to this work have been explicitly indicated below. I confirm that appropriate credit has been given within this thesis where reference has been made to the work of others.

The work presented in Chapter 5 was previously published in *International Journal for Numerical Methods in Engineering* as "Isogeometric FEM-BEM coupled structural-acoustic analysis of shells using subdivision surfaces" by myself, Musabbir Majeed, Fehmi Cirak and Robert N. Simpson. This study was conceived by all of the authors. Musabbir Majeed and Fehmi Cirak provided the implementation of the finite element shell formulation. Robert N. Simpson was my primary supervisor for my PhD study. I carried out the majority of the implementation and all the numerical analysis.

Chapter 1

Introduction

1.1 Acoustic scattering in engineering applications

When a propagating sound wave encounters an obstacle, part of the wave will deviate and spread around the obstacle. This phenomenon is called acoustic scattering [6]. Acoustic scattering has many important applications. For example, it is used in medical ultrasound imaging techniques [7, 8]. Ultrasonic equipment produces a high frequency acoustic wave. The wave is transmitted in the human body and scattered by different tissues and viscera. Images of the internals of the human body are constructed based on received echoes, which can help doctors in diagnosis. Ultrasonic wave propagation in solids is also used in material testing [9]. For example, by analysing the ultrasonic wave scattering in metal, such as steel and aluminium, defects and cracks can be detected because they behaved as acoustic scatterers. This technique does not affect the performance of the subject under inspection and it is named non-destructive testing (NDT) [10].

The sonar system is based on acoustic wave propagating underwater [11]. Sound waves are transmitted into the water to detect underwater structures, such as torpedoes and submarines. By constantly transmitting and receiving the acoustic waves, the speed and direction of the travelling target can be inferred. By analysing the scattering behaviour, the sonar system can estimate the size of the object and determine the profile of the detected target. The majority of man-made underwater structures can be viewed as shell structures and they are more easily

excited than rigid objects when impinged by incident acoustic waves. The shell structure vibrates and becomes a secondary acoustic source, which also radiates additional acoustic waves. In this circumstance, the acoustic wave consists of three parts: the incident wave, the scattering wave and the radiated wave. Therefore, when designing underwater structures, the additional radiated wave must be considered as it may significantly influence the ability to conceal the structure. Analytical solutions for the acoustic scattering over simple geometries such as spheres and cylinders can be found in [12]. However, practical engineering structures always have complex geometries. These geometries must be modelled using CAD tools to show the design details. Acoustic scattering over these geometries cannot be solved analytically. Therefore, numerical methods are often used to analyse such complex geometries.

1.2 Numerical methods for coupled structural-acoustic analysis

The dynamic interaction between fluids and solids is an important concern for the engineering design of underwater structures. Due to the coupling effect, the structural dynamic response and acoustic performance of the underwater objects cannot be considered separately. An acoustic wave propagating in the water creates a fluid load on the surface of the structures, thereby exciting it. Furthermore the underwater structure scatters the acoustic wave and vibrates due to the excitation. The shell moves with a velocity which also radiates an additional acoustic wave to the fluid. This is termed an acoustic fluid-structure interaction (FSI) problem. To solve this problem numerically, two formulations (one for the fluid and one for the solid) must be coupled by finding the relationship between the relevant physics. The selection of appropriate numerical method for the two different problems is vital for stability and robustness analysis. The finite element method (FEM) is the dominant numerical method in structural analysis but the optimal computational method for acoustics is subject to debate. Commonly used numerical methods in computational acoustics include the finite element method, the finite difference method (FDM), the finite volume method (FVM) and the boundary element method (BEM). They all have their strengths and weaknesses depending on the type of problem. For the scattering problem with

an infinite domain, the boundary element method has a unique advantage as it only requires a discretisation of the boundary surface and it satisfies the Sommerfeld radiation conditions of Helmholtz equation [13], which requires the acoustic wave must scatter to infinity. Using the BEM to solve the Helmholtz equation for acoustic scattering problems is a common approach in engineering. Notable literature includes Shaw [14], Ciskowski and Brebbia [15], Bai [16] and Wrobel [17]. The BEM adopts the fundamental solution (Green's function) of the governing partial differential equation to establish an integral equation only on the boundary using Gauss's law. This integral equation is called the boundary integral equation and the boundary element method is also known as boundary integral method. Then, the boundary integral equation is discretised and the resulting system of equations with appropriate boundary conditions solved numerically. Because the BEM is a semi-analytical method, the numerical results are more accurate than those of other methods. However, the BEM has difficulties in dealing with non-linear acoustic scattering in fluid [18], as governed by the Westervelt equation. The fundamental solutions of such non-linear partial differential equation are impossible to obtain. Moreover, the Green's function of governing equation and its normal derivative often contain singular terms, which leads to difficulties in their integration. Regularisation methods subtract a static term from the original integration kernel which can decrease the strongly singular function into weakly singular function and transformation methods (eg. polar coordinates transformation, Telles' transformation [19] and Duffy transformation [20]) can be used to shift the positions of the quadrature points and thereby avoid the remaining singularity.

A number of methods are available to couple the finite element method for structural dynamics and boundary element method for acoustic analysis, to solve the acoustic FSI problem. The earliest work to adopt this idea is Everstine and Henderson [21]. In order to increase the computational efficiency, Fischer and Gaul [22] coupled the fast multipole boundary element method with the plate elements. However, they adopted a Galerkin approach to formulate the boundary element method. The Galerkin approach has a solid theoretical base but requires a costly double integration over the boundary elements. Schneider [23] improved the computational efficiency of the coupled method using a collocation approach to formulate the boundary element method. However, Chen et al. [24] stated that the efficiency of the fast

multipole boundary element method drops dramatically as the acoustic frequency increases. He used a coupled finite element method and wideband fast multipole boundary element method to overcome this problem.

1.3 Integrated CAD and numerical analysis for underwater structures

In order to minimise resistance when moving in a fluid, the geometry of many underwater structures, e.g. submarines, ships and torpedoes, are carefully designed as streamline bodies with smooth surfaces. The conventional finite element and boundary element methods employ a Lagrangian discretisation of the geometries. A Lagrangian discretisation often approximates the geometry with a number of low-order elements, which introduces geometry errors into the numerical results. Moreover, only C^0 continuity can be obtained between elements, which artificially create non-smoothness on the boundary and it increases the difficulty of performing singular integration by inducing unnecessary corners on the boundary. A common approach is to use discontinuous boundary element methods and locate the collocation points within the elements, but it sacrifices extra computational time.

There are two main formulations for shell analysis: Kirchhoff-Love theory and Reissner-Mindlin theory. The Kirchhoff-Love formulation has the requirement that the deflection field be C^1 continuous everywhere. Thus conventional finite element method for shell structures prefers to adopt Reissner-Mindlin theory due to Lagrangian discretisation can not satisfy this requirement. However, Each nodal point in the discretised Reissner-Mindlin shell has six degrees of freedom: three translational and three rotational. The three additional degrees of freedom greatly increase the size of the system of equations to be solved with an associated increase in computational time. Noels and Radovitzky [25] proposed a discontinuous Galerkin (DG) method for Kirchhoff-Love shell to avoid this expensive computation. The DG formulation [26] is also a finite element method derived from the weak formulation but uses only piecewise continuous functions for interpolation and add an enforcement to achieve inter-element C^1 continuity. Another alternative to overcome this problem is using meshless

method [27, 28].

Hughes et al. [29] proposed the concept of isogeometric analysis in 2005. The main objective is to use the same discretisation for both design and analysis. The geometry discretisation used in spline technology has a high degree of continuity between elements and can overcome both problems for boundary element method and Kirchhoff-Love shell formulation in an elegant way. Computer-aided design (CAD) and computer-aided engineering (CAE) are widely used for design and analysis in many engineering fields. However, design models and analysis models are usually generated in two different ways. The spline technology in CAD software can easily model smooth, streamlined surfaces and capture details of the designed geometries. Engineering analysis software however often use relatively simple schemes to discretise the geometry into a number of low order elements for analysis. In the current engineering workflow, the object is first designed with CAD software. The design model always consists of different components in order to capture the design features. For instance, the main body of a submarine can be modelled with fairly simple cylindrical and hemispherical geometries but the fins and propellers should be described in detail with advanced CAD techniques. A common approach is to model each component individually and assemble them at the end of the design, but this generally leads to gaps and overlaps between the different components. Engineers must then manually fix those conflicts to generate a mesh for analysis. After the numerical analysis, the results provide guidances for design updates. This process will repeat until the analysis results meet all the design criteria. The conversions between the design models and the analysis models often require massive extra efforts and also sacrifice design features in order to be analysis-suitable. In a practical engineering project, the works in meshing and CAD recovering stages may take more than 80% of the entire analysis time [30]. This inefficiency greatly limits the development of computer-aided engineering. IGA directly uses the spline functions from the design model for analysis. Since the design and the analysis use the same discretisation, the geometry remains unchanged in the entire analysis process and there are no geometric errors in the numerical results. So, this method is called "isogeometric analysis". It integrates design and analysis and skips the expensive data conversions.

The most commonly used technique in CAD software are Non-Uniform Rational B-Splines

(NURBS), which are a general extension of B-splines to provide great flexibility and accuracy to model specific geometries, such as spheres, cones and cylinders. Because NURBS dominated the CAD market, early IGA tended to use NURBS discretisation for analysis. However, NURBS surfaces have significant limitations for modelling complex geometries due to its tensor product nature. A CAD model always combines multiple NURBS patches with different resolutions to represent complex geometries with arbitrary topologies. In this case, it is difficult for the design geometry to maintain watertightness and continuity between patches, which is problematic to the analysis. Moreover, due to the tensor product nature, the NURBS model can not perform local refinement and adaptive meshing during the analysis process. This greatly limits the application of isogeometric analysis to practical problems. A number of analysis-suitable techniques have been developed and implemented into IGA to overcome these two limitations, the most notable being T-splines [2, 31]. Cirak and Ortiz [32] employed an alternative geometry representation technique, Loop subdivision surfaces, for Kirchhoff-Love shell structural analysis. Unlike T-splines, the subdivision surfaces is a mature geometry representing technique which are already widely used in gaming and animation industries. The Loop subdivision surfaces adopt a triangular linear control mesh to evaluate a smooth limit surface with quartic box-spline functions [33]. The control mesh of Loop subdivision surfaces allows extraordinary vertices, which means that the number of neighbouring vertices that each vertex can connect to is not limited to six. Except for the surface points related to extraordinary vertices, the subdivision limit surface has C^2 continuity everywhere. Where the surface points are related to extraordinary vertices they have C^1 continuity. The entire surface is smooth everywhere and the high level of continuity meet the requirement of Kirchhoff-Love shell theory. Extraordinary vertices enable subdivision surfaces to model watertight geometries with smooth surfaces and arbitrary topologies, and they also provide the possibility of local refinement and adaptive meshing.

In computer aided design, solid geometries are modelled using a boundary representation (B-rep) methods, where only the surfaces are represented using spline techniques. In engineering analysis however, the dominant numerical methods always require volumetric discretisation. The development of trivariate spline techniques that are compatible with analysis in CAD has become the most important and challenging work in isogeometric analysis [1]. Nevertheless,

both the boundary element method and shell formulation only require a boundary discretisation of the object which means it is possible to use a subdivision discretisation to fully integrate the design and analysis for the underwater structures which scatter acoustic waves.

1.4 Novel contributions

A new isogeometric boundary element method with subdivision surfaces is presented for acoustic analysis. It employs the Loop subdivision surfaces to discretise the Helmholtz boundary integral equation. By adopting the high order spline functions to perform Helmholtz analysis, a higher accuracy per degree of freedom is obtained over equivalent quartic Lagrangian discretisations. Inspired by the work done by Fritze et al. [34], this method is further combined with the Kirchhoff-Love shell theory using the same Loop subdivision surfaces. The implementation of the Kirchhoff-Love shell with Loop subdivision surfaces has been done by Cirak and Ortiz [32]. A novel coupled boundary element and Kirchhoff-Love shell formulation is presented based on their work to perform structural-acoustic analysis with Loop subdivision surfaces. The Loop subdivision surfaces provide a smooth boundary discretisation with high order spline functions which satisfy the C^1 continuity requirement of the Kirchhoff-Love theory and continuous boundary element method. Compared with methods in literature [23, 24, 34], the presented method has a much smaller system matrix for the same problem and is hence more computationally efficient. With the implementation of hierarchical matrices (\mathcal{H} -matrices) [35], this novel method can handle acoustic problems with higher frequency and complex practical geometries.

1.5 Manuscript organisation

This thesis summarises the background knowledge and theory for the coupled isogeometric boundary element and finite element method for structural-acoustic analysis with subdivision surfaces. Numerical examples are also presented to verify the method and demonstrate the advances of IGA in accuracy and efficiency. The goal of Chapter 2 is to review the literature

on some of the most important developments in the IGA after the seminal paper published in 2005. The focus is on the three limitations of NURBS and how to deal with them, including the methods of performing analysis with commercial CAD models, the developments of analysis-suitable splines and B-rep IGA methods. Chapter 3 presents the theories of fundamental CAD techniques, NURBS and subdivision surfaces, from two dimensional curves to three dimensional geometries. The acoustic boundary element method detailed in Chapter 4, where the fundamental solution of the Helmholtz equation, the governing equation for acoustic problems, is first introduced. After that, a step-by-step derivation of the boundary integral equation for acoustic scattering problem is presented. From Section 4.3.1, the novel boundary element method with Loop subdivision surfaces is presented. A collocation approach is introduced to formulate the boundary element method and the integration schemes for singular integrals are demonstrated. Numerical examples are then presented to verify the methods in Section 4.5. This thesis will not repeat the details of Kirchhoff-Love shell with Loop subdivision surfaces but a brief review will be presented in the first part of Chapter 5. This is followed by an illustration of the coupled boundary element and finite element formulation for structural-acoustic shell analysis. More practical geometries are used to demonstrate the advances of this coupled isogeometric method in Section 5.3.

Chapter 2

A review of isogeometric analysis

This chapter will first introduce the concept of isogeometric analysis (IGA) and illustrate its potential to change the traditional engineering workflow, followed by the three major challenges in the development of IGA and the reasons for them. Then, a literature review of methods which use industrial Computer Aided Design (CAD) geometries for IGA is given in Section 2.3. After that, Section 2.4 will review the developments of analysis suitable computer aided geometry design (CAGD) techniques including T-splines, Hierarchical B-splines, PHT-splines, LR B-splines and subdivision surfaces. The last section will state the developments of parameterisation methods to create volumetric splines discretisations for analysis and two surface-based IGA methods using shell formulation and boundary element formulation.

2.1 Isogeometric concept

In modern engineering workflows, manufacturing industries rely on CAD models to describe the geometry of a production object. During the creation of such models, numerical methods which provide insight into the physical behavior of an object are used extensively with the process often referred to as Computer Aided Engineering (CAE). Traditionally, engineering practice considers CAD and CAE as two separate stages in the engineering workflow. Figure 2.1a shows a flowchart of the conventional manufacturing design process. An initial design is always generated and passed to the analysis engineer together with a CAD model. Then, the engineer

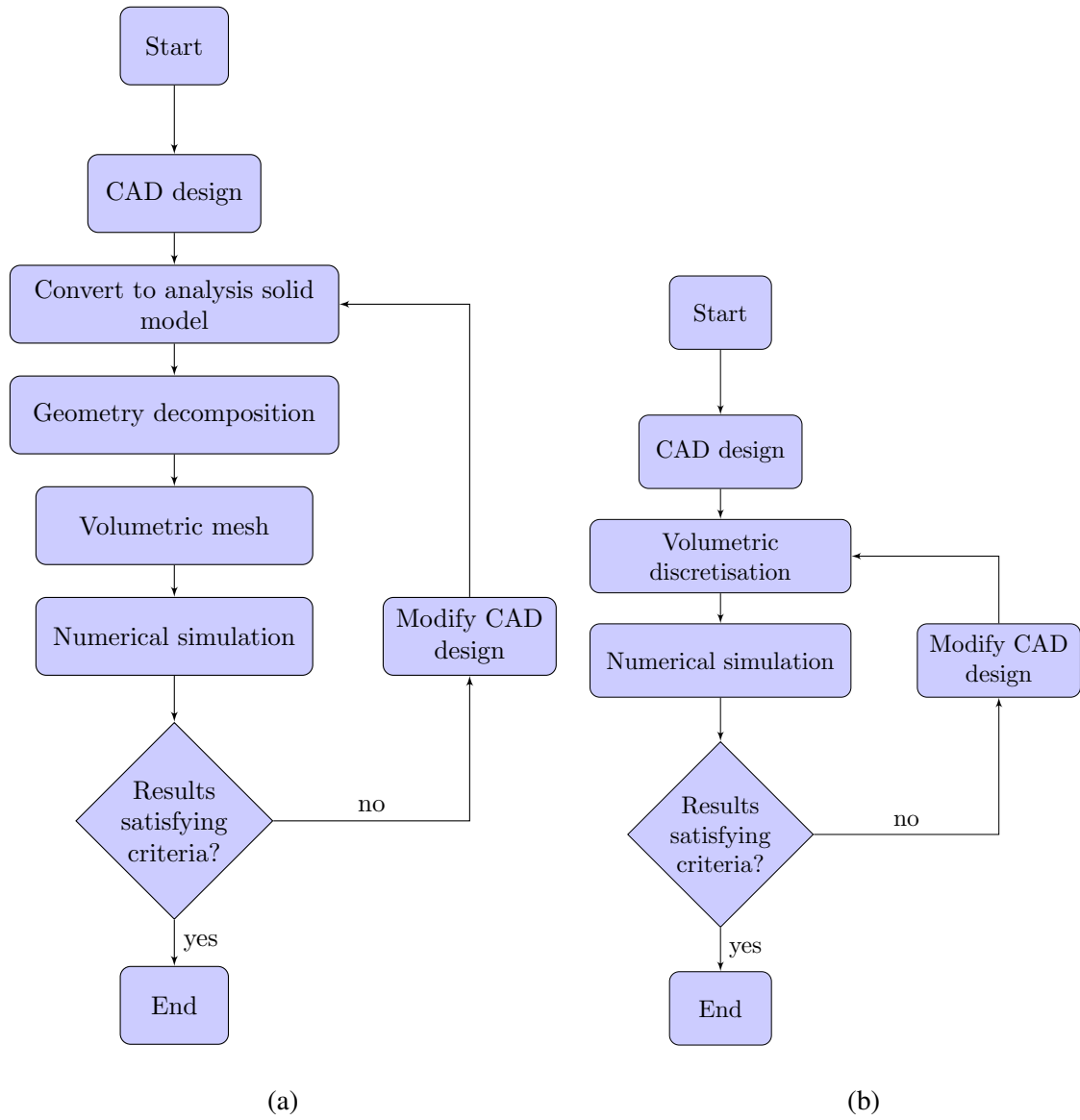


Figure 2.1: (a) Conventional workflow. (b) Isogeometric analysis workflow.

needs to convert the design model into a new model which is suitable for analysis. This step normally heals and repairs corruptions of the model through manually patching gaps, removing overlaps and defeaturing the complex detailed designs. After that, the model is volumetrically meshed for analysis. After numerical analysis, e.g. using finite element or boundary element analysis, engineers must adjust the CAD design model by updating corresponding design parameters based on the analysis results. These steps will repeat a number of times until the results satisfy all the design criteria. The CAD adjustments and mesh regenerating stages always involve manual interfaces which are time consuming. Moreover, the complexity of geometry in industries such as the automotive, aerospace and ship building is ever increasing, so that approximately 80% of the total time of CAE is taken up by those mesh regeneration and CAD recovery procedures [29]. Thus, the conversion between CAD models and analysis models is a severe bottleneck in CAE and leading to costly time delays.

Isogeometric analysis was generalised and proposed by Hughes et al. [29] in 2005. The IGA directly adopts the spline functions from design models to perform analysis. There is no geometric error in the results since the design geometry and analysis geometry are one and the same. The method is called "isogeometric analysis" because the geometry remains unchanged during the analysis process. IGA aims to improve engineering product design using the same discretisation to integrate design and analysis and skip the costly mesh regeneration stages. It is a potentially revolutionary approach to overturn the traditional engineering workflow and simplifies it into a more efficient version, as shown in Figure 2.1b. This IGA concept has been implemented in a number of engineering applications. Areas of research receiving considerable attentions include shell analysis [36], electromagnetics [37], structural vibrations [38], fluid-structure interaction [39] and shape optimisation [40–42].

The early IGA literatures focused on Non-Uniform Rational B-Splines (NURBS), which is derived from B-splines, simply because NURBS is the standard CAD geometry representation tool widely used in commercial software. However, NURBS and B-splines are both developed on a single patch rather than individual elements. As figure 2.2 shown, B-splines have a parametric domain which can be subdivided into sub-domains and mapped to the physical domain. Each basis function can span multiple sub-domains, which makes these sub-domains

not directly available as "elements" in finite element analysis. The Bézier extraction method was a milestone of IGA developments [43]. It mapped sub-domains into individual Bézier elements. With this mapping method, one can use different parametric domains for geometry and analysis, and the Bézier elements can be easily evaluated using Bernstein polynomials which are more amenable to computational methods.

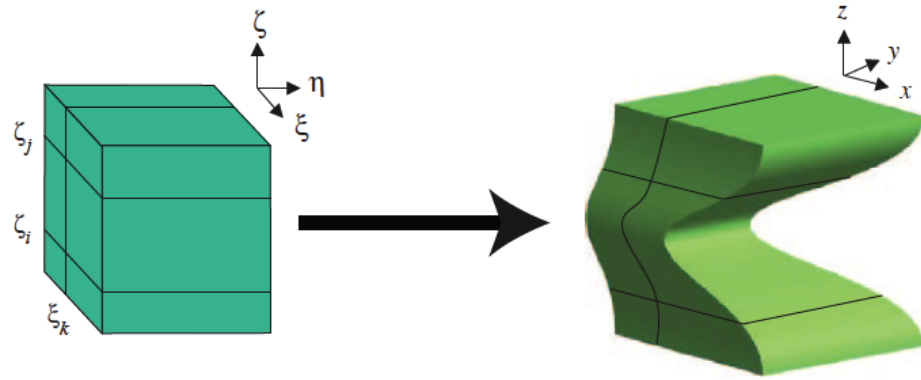


Figure 2.2: An example B-spline mapping from parametric domain to physical domain. Figure is reproduced from [1].

However, NURBS-based CAD models still have difficulties when used in IGA. The next section will state the three main challenges that IGA faces to integrate design and analysis. Section 2.3, 2.4 and 2.5 will further illustrate these three challenges and also review the works have been done to overcome them.

2.2 Challenges of isogeometric analysis

Although IGA has a number of attractive features, applying the IGA workflow in industry is not straightforward. The early IGA research focused on applying NURBS basis functions in analysis simply because it is the most commonly used computer aided design tool in commercial software. However, NURBS surfaces has three major limitations when they are used in analysis.

2.2.1 Complex geometry with arbitrary topology

The first limitation is that NURBS surfaces have difficulties in modelling complex geometries with arbitrary topologies. This is due to the tensor-products nature of NURBS surfaces. A conventional NURBS-based IGA model can only describe complex geometries using a number of tensor-product patches. The isogeometric analysis requires the patches to fit perfectly together to keep geometries watertight and also remain high geometry continuity across multiple patches. A geometry with arbitrary topology always requires significant number of patches jointed together. This will require additional modifications of the complex CAD model before analysis.

2.2.2 Local refinement and adaptivity

The second limitation is NURBS model can not be locally refined and adaptively meshed in analysis. This limitation is also caused by the tensor-product nature of NURBS surfaces. A number of alternative CAD techniques were developed to overcome this limitation and used in IGA, including Hierarchical B-splines [3, 44], T-splines [2, 31], PHT-splines [45, 46] and LR B-splines [47, 48]. These locally refinable techniques are introduced in section 2.4. Another alternative technology, subdivision surfaces, is also used in analysis [5]. Subdivision surface is a geometry representation tool derived from B-splines, which overcomes the tensor-product limitation of NURBS surfaces to enable local refinements. Subdivision surfaces can model complex geometries with arbitrary topologies with one mesh.

2.2.3 Volumetric discretisation

The aforementioned two limitations are both attributed to the tensor-product nature of the NURBS surfaces. This problem can be solved by using more advanced CAD tools. However, not only NURBS surfaces, but almost all the CAD techniques have a third limitation which is they are not volumetric representations. The spline-based CAD discretisation are all boundary-representation methods. They use curved surfaces to represent three dimensional objects. However, the dominant numerical method in computational engineering is the finite element method which requires a volumetric discretisation of the analysis object. The early IGA works

were limited to solving two dimensional problems. Comparing with the above two limitations, overcoming this limitation is more essential and vital for developments of IGA as a design tool. Therefore, a number of researchers are working to develop a robust and efficient method to generate trivariate geometrical representations for the interior solid from the surface models [4, 49–52].

The surface-based formulations are naturally attractive to the IGA community since they do not suffer from this limitation. IGA shell formulations are always popular because isogeometric analysis can provide smoothness of high order across elements which is essential for rotation-free shell theories, such as Kirchhoff-Love. Boundary element method (BEM) solves partial differential equations formulated as boundary integral equations. Compare with finite element method it has several advantages, the most distinct feature attractive to IGA is that BEM solves the three dimensional problems only using equations on boundaries which avoids the costly volume parameterisation process. BEM can be applied in a number of engineering areas and has particular advantages in exterior problems, such as acoustics and electromagnetics.

2.3 Working with industrial CAD geometries

The industrial CAD models often have gaps and overlaps and the computer aided geometry design (CAGD) community either ignored these flaws or adopted very crude methods to solve the problem as they mainly focused on creating smooth and accurate complex geometries. In order to construct complex geometries with arbitrary topology, industrial CAD models use trimming curves to remove parts of the surfaces. This is an efficient way for geometry representation but it is also a crude approach from an analysis perspective. After IGA becoming popular which linked CAGD and CAE communities, researchers started to pay attentions to finding methods to joint different NURBS patches and also perform analysis with trimmed surfaces.

2.3.1 Conforming and non-conforming patches

As one of the limitations of NURBS surfaces, commercial CAD models are always composed by a number of patches because of the tensor-product nature of NURBS. These patches often connect poorly because they are, in general, not on the same parametric level. When these models are used in analysis, the jointed boundaries of the non-match patches must be treated carefully to ensure the geometries are watertight. The common issues include existing gaps and overlapped surfaces. Costly manual interferences should be made to tide up the CAD models before conducting the analysis. Moreover, the difference of mesh resolutions between two jointed patches is a crucial challenge for a straightforward coupling. This problem is called "non-conforming" patches. The conventional way to overcome this problem is to conform the two patches by refining at least one of them to ensure the control points on the two jointed edges are one-to-one corresponded. Then, the model becomes a conforming discretisation, as shown in Figure 2.3b. Although applying analysis with conforming patches is relatively easy, there are also notable works focused on coupling non-conforming patches for analysis [53–57] because the non-conforming patches are more common in CAD models.

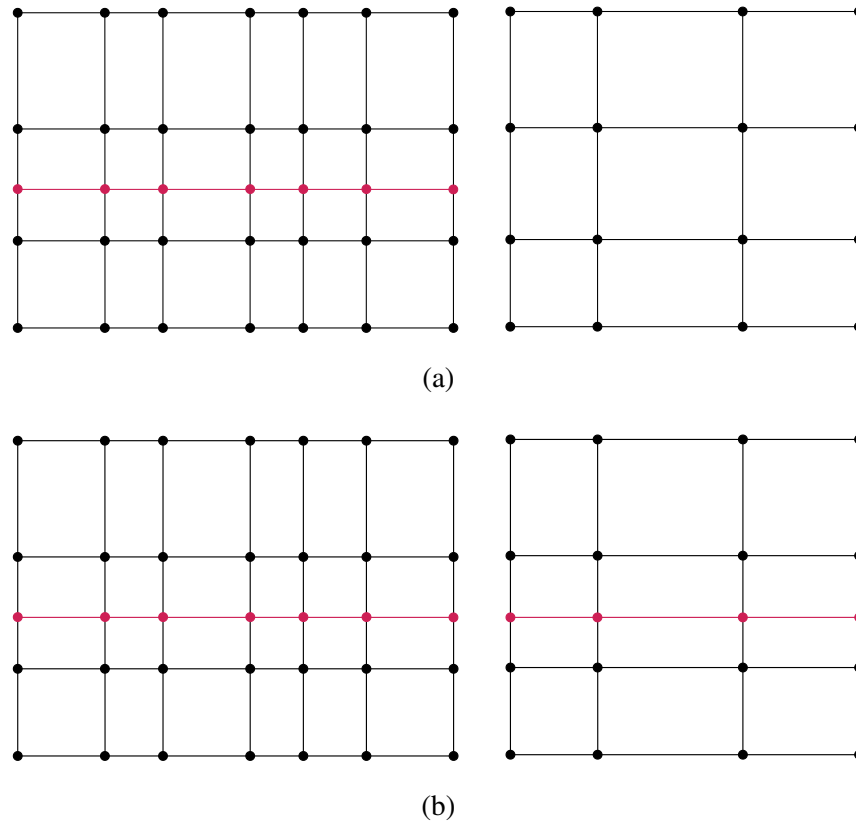


Figure 2.3: (a) Example of non-conforming patches. (b) Example of conforming patches.

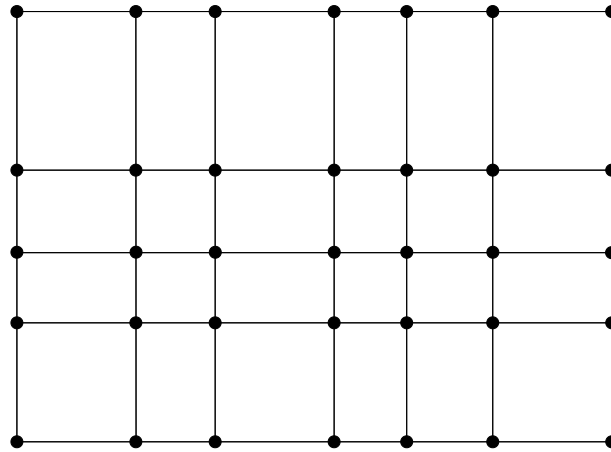
There are two different notations for continuity: parametric and geometric. A curve with a parametric continuity C^n means the first to the n^{th} derivatives of value at any point are continuous. Two curves can be combined into a new curve with geometry continuity G^n if the two segments have the same n^{th} order geometry smoothness at the joint point. One of the important advantages of IGA is that it can provide a high-order continuity discretisation. However, it is difficult to achieve this property across NURBS patches. A number of studies have been done to couple multiple patches and retain continuity across patches. Early studies of the continuity across multiple patches include Cottrell et al. [58] who showed C^0 continuity is easily achieved for conforming patches. However, the more interesting C^1 continuity across multiple patches needs special treatments to achieve. C^1 continuity is very important for isogeometric analysis because it is required by Kirchhoff-Love shell formulation. Kiendl et al. [59] proposed a method, called the bending strip, to perform shell analysis using an additional strip of fictitious material in the connecting places. This method coupled the patches with a geometric continuity G^1 , which means each pair of points on the jointed edge have a common tangent plane. Schmidt

et al. [60] employed trimmed NURBS surfaces for coupling patches with C^1 continuity to perform shell analysis. But these two methods are only valid with conforming patches or hierarchical meshes. Lei et al. [53] adopted a penalty formulation to couple non-conforming NURBS patches for Kirchhoff-Love shell analysis in an isogeometric approach which has C^0 and G^1 continuity across patches. Successful coupling methods are also used for the analysis of Reissner-Mindlin plates which also requires C^1 continuity [52, 55].

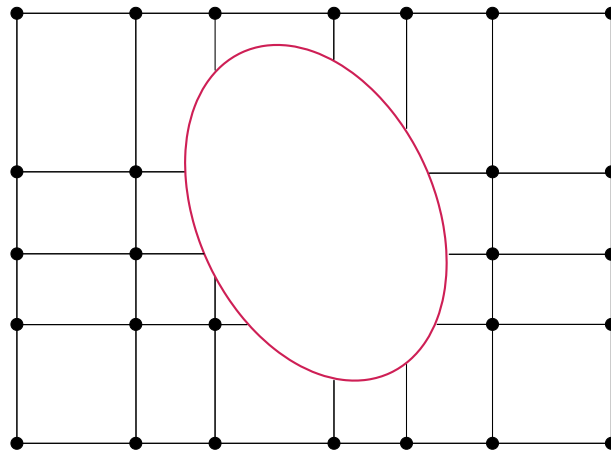
2.3.2 Trimmed CAD surfaces

Trimmed CAD surfaces are an efficient way to define complex geometries with arbitrary topologies in existing CAD software. Compared to conventional NURBS surfaces, trimmed NURBS surfaces avoid separating the geometry into multiple tensor-product NURBS patches by only use additional trimming curves to describe the trimmed regions, as Figure 2.4 shown. This saves a lot of manual works in the implementation of IGA. In the original work presented by Kim et al. [61], trimmed surfaces were used in an isogeometric finite element analysis for two dimensional elastic plate problems. They presented the formulation for constructing the system matrix with trimmed surfaces and showed the trimmed surfaces have better behaviour over conventional NURBS surfaces. Kim et al. [62] extended this work and used the trimming curves to describe both the outer boundaries and the inner trimmed regions of the geometry, which showed the abilities of trimmed surfaces in describing any arbitrary topologies. The data of the trimming curves are directly extracted from the CAD software for IGA analysis, which is an integration of CAD and numerical analysis. The same spline functions are used for both trimmed and non-trimmed regions, which maintained the isoparametric properties in the IGA analysis of trimmed CAD surfaces. Because of the flexibility in representing arbitrary topologies, the trimmed CAD surfaces was implemented in topology optimisations by Seo et al. [40]. Schmidt et al. [60] presented a different method to perform isogeometric shell analysis with surfaces coupled by several trimmed NURBS patches. Beer et al. [63] proposed a method for isogeometric analysis with trimmed CAD surfaces involving an additional mapping step, which provided a simple approach to perform IGA directly with the data from commercial CAD

software.



(a) A NURBS surface.



— Trimming Curve

(b) A NURBS surface trimmed by a NURBS curve.

Figure 2.4: An example of a trimmed CAD surface.

2.4 Analysis suitable CAGD techniques for IGA

The CAD community is a much larger than CAE community. Advanced geometry representation methods were designed for film, animation, gaming and advertising but seldom for engineering. The commercial CAD models are "dirty" geometries, which normally have gaps and overlapped surfaces and the traditional analysis models always have large geometry

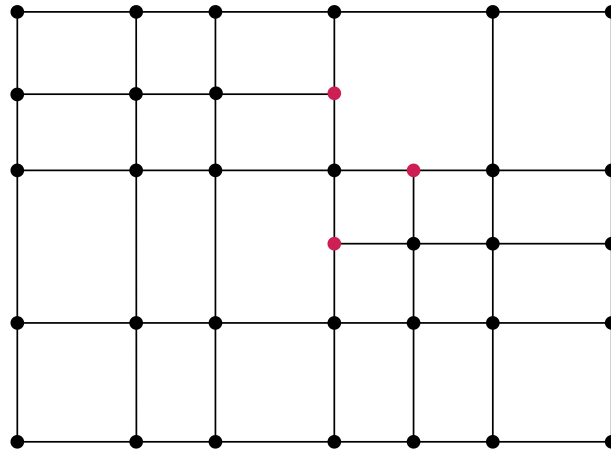
errors and the geometries will keep changing during the refinements in analysis. The rapidly evolving IGA has received attention from the CAD community. Development of analysis suitable geometry representation tools becomes a new and attractive research direction, which is to invent a good geometry representation technique for both design and analysis stages. This section will introduce five analysis suitable CAGD tools used in isogeometric analysis.

2.4.1 T-splines

T-splines can be seen as NURBS surfaces with T-junctions. They were invented to overcome the tensor-product limitation of the NURBS surfaces. They were first introduced in [31] and quickly implemented in isogeometric analysis [2] using the finite element method. T-splines are based on a new spline technology called point-based splines (PB-splines). PB-splines use unstructured point clouds instead of meshes to control the geometries. Every control point in the clouds has a local knot vector with arbitrary length and each control point is associated with a blending function. The PB-splines can locally add more control points to describe the complex part of the geometry and use sparse point cloud to represent the less important regions. It can be seen as a generalisation of the NURBS but it removes the limitation of the structured control meshes. However, PB-splines is not very compatible with other numerical methods, e.g. finite element method and boundary element method, because it does not have a clear element structure for analysis. Moreover, each of the blending functions is constructed independently so that the discretisation model is very difficult to be refined without changing the original geometry. Although PB-splines have a number of nice properties in adding flexibilities in designing complex geometries, the weaknesses are also very obvious. To date, no commercial software in the CAD market has used PB-splines to design geometries. T-splines adopt the idea of the PB-splines which use local knot vectors to define blending functions but retain the analysable elements structure of NURBS.

An example of a T-splines control mesh (T-mesh) is showed in Figure 2.5. Complex geometries modelled by NURBS surfaces always suffer from watertight problems, such as gaps and overlapping surfaces between two NURBS patches. T-splines allows hanging points to connect two non-conforming patches into one single mesh, see Figure 2.6. It can model the

geometry with a single smooth and watertight surface. In the conventional NURBS-based IGA, costly manual modifications should be conducted to conform multiple patches before the analysis stage. Using a T-splines discretisation in IGA can eliminate this time consuming stage. Moreover, the T-junctions enhance the capability of T-splines to model more complex geometries. It is easier to use a non-uniform mesh with higher densities for part of the geometry to show more design details and lower densities for less important regions. Compared with NURBS surfaces, T-splines can use far fewer control points to represent a geometry with the same level of complexity. When T-splines are used in IGA, it allows for local refinements and adaptive meshing of the geometry, which are essential for the design updates and circulative analysis in CAE workflow.



- control point
- T-junction point

Figure 2.5: An example T-spline control mesh.

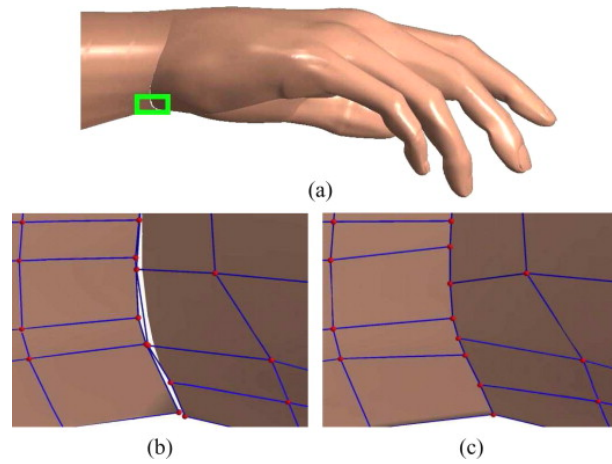


Figure 2.6: (a) A complex CAD model of a hand. (b) Visible gaps existed between two NURBS control grids. (c) A watertight T-mesh conforms NURBS patches. Figure is reproduced from [2].

2.4.2 Hierarchical B-splines

Hierarchical B-splines were introduced by Forsey and Bartels [44]. They refine parts of the basis functions and combine the refined basis functions with the original ones, as shown in Figure 2.7. The method adopts the refinable nature of B-splines and provides the ability to locally refinements and add geometric details in the required locations without changing the rest of the geometry. This is called multi-resolution editing. Vuong et al. [3] implemented hierarchical B-splines in isogeometric analysis. Schillinger et al. [64] explored adaptive hierarchical refinement for NURBS and used it to conduct fluid-structure analysis. Giannelli et al. [65] modified the classical hierarchical B-splines and developed a new technique which enables one to define locally supported basis functions, named truncated hierarchical B-splines (THB-splines). Hierarchical B-splines overcome the issue of modelling local shape details but because it still has a nested structure, it has difficulties in modelling geometries with arbitrary topologies.

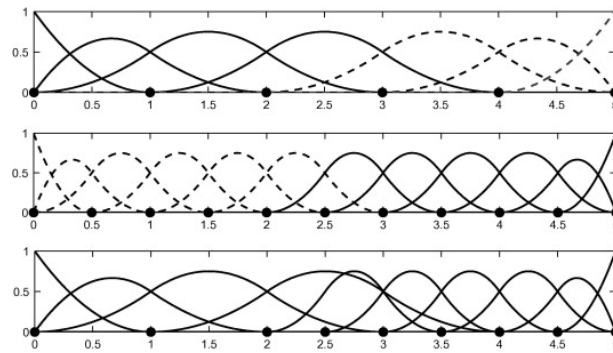


Figure 2.7: Construction of a hierarchical B-spline: initial basis functions (above), refined basis functions (middle) and combinations of two levels of basis functions (below). Figure is reproduced from [3].

2.4.3 PHT-splines

In Section 2.4.1, T-splines were introduced as an advanced CAD technique. It overcomes the tensor-product weakness of NURBS and has advantages in modelling complex topology and conducting adaptive analysis, but the basis functions of T-splines are locally defined and the sum of all the basis functions does not naturally equal to an unity. The basis functions of T-splines must be divided with the sum to ensure each basis is a partition of unity. Therefore, the basis functions of T-splines are rational functions. This feature makes T-splines complicated and also costly to implement. Deng et al. [45] introduced the polynomial splines over hierarchical T-meshes (PHT-splines) which extended the T-splines with hierarchical concepts which enhance T-splines in a number of aspects including that it uses polynomial functions instead of rational B-spline functions. PHT-splines can model more detailed features of geometries. However, in the term of analysis, PHT-splines, as an extension of T-splines, are developed on a relatively complicated theory and are hard to implement. By far, to the best knowledge of the author, no commercial software implemented the PHT-splines for geometry design.

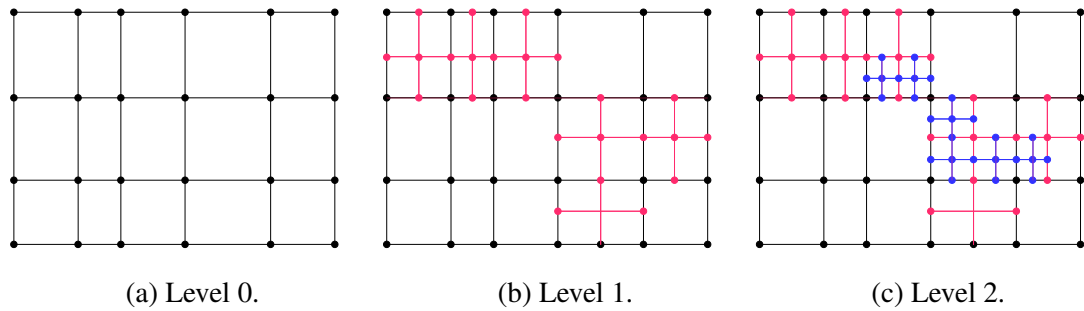


Figure 2.8: An example hierarchical T-mesh.

2.4.4 LR B-splines

Just as its name implies, Locally Refined B-splines (LR B-splines) have a very clear objective, which is to add local refinement abilities on B-splines. It was proposed by Dokken et al. [47] in 2013 to create a new CAGD technique which has advantages in both design and analysis and it was implemented into IGA in 2014 by Johannessen et al. [48]. The LR B-splines method is driven by the idea of refining the model directly in the parametric domain to locally create new elements for analysis. Refinement happens by inserting line segments to partition a tensor-product spline space into a T-mesh. Every inserted line segment will increase the dimension of mesh and the corresponding basis functions in the affected region are deleted and new basis functions are added back to complete the refinement process.

2.4.5 Subdivision surfaces

Subdivision surfaces is a good alternative to T-splines since it can also overcome the limitations of NURBS surfaces and it is also a mature method which is widely used in animation and gaming industries. A number of geometry design software for digital entertainment have implemented subdivision surfaces. Compare with T-splines and PHT-splines, subdivision surfaces uses a simpler data structure to represent complex geometries. One begins with a coarse polygon mesh and applies a certain subdivision algorithm to recursively refine this polygon mesh until refined meshes eventually converge to a smooth limit surface. The limit surface can be evaluated using spline functions from any level of refined meshes. The polygon mesh can be locally refined and adjusted to model any arbitrary topologies. The most well-known subdivision algorithm

for generating surfaces is Catmull-Clark developed in 1978. Due to the advantages of the subdivision surfaces in modelling geometries with arbitrary topologies, it gained popularity during the 1990s along with the development of digital entertainment industries [66, 67].

Subdivision surfaces only have uniform parametric domains for all elements and the degree of the surface is fixed, but it has the ability to represent complex geometries with simple meshes and simple evaluating methods. This unique feature of subdivision surfaces has recently gained the attention of the engineering community. Subdivision surfaces do not have the limitations of NURBS and are also easy to implement. It has already been available in a number of CAD commercial software including Autodesk Fusion 360[®][68], PTC Creo[®][69] and 3DS CATiA[™][70] which provide prerequisites for integrating design and analysis using this geometry representation technique. Loop [33] developed a subdivision scheme in 1987, which can generate smooth surfaces through triangular control meshes. The Loop subdivision surfaces can be evaluated using box splines basis functions. Cirak [5, 32] implemented Loop subdivision surfaces for Kirchhoff-Love shell analysis in 2000. Loop subdivision surfaces use linear triangular mesh as the control mesh which is easily refined and adjusted during the recursive analysis process. The analysis method with subdivision surface discretisation can analyse a complex engineering geometry with only a single linear mesh where NURBS-based IGA approach may need multiple patches to address the complex topologies. Subsequently, subdivision surfaces have been extended to applications including shape optimisation [71], and shells, including non-manifold shell geometries [72] and thick shells [73].

2.5 Volume parameterisation and surface-based IGA formulations

2.5.1 Volumetric spline parameterisation

Because the dominant numerical analysis methods require volumetric discretisations, trivariate splines have been developed in [74] and used in IGA. However, the CAD techniques used in

commercial design software are only surface representing tools (bivariate splines). In order to achieve a full integration of computer aided design and analysis, the parameterisation from a bivariate spline-based surface into trivariate spline based solid is crucially required. Cotrell et al. [1] stated that the development of three-dimensional spline parameterisations is "the most significant challenge" in IGA. The early attempts of volume parameterisation in IGA literature include [49, 75, 76]. Li et al. [75] used harmonic functions to conduct volumetric parameterisation, but their approach requires expensive trial-and-error optimising. It requires extensive manual interfaces which is not robust. Martin et al. [76] proposed an approach to generate a trivariate B-spline mesh through parameterisation with discrete harmonic functions from triangular surface mesh. However, this method can only be applied to genus-zero objects. At the same time, Aigner et al. [49] applied an alternative swept volume parameterisation to generate NURBS volume for isogeometric analysis. Shortly after the invention of T-splines, the volumetric parameterisation of T-splines becomes popular because it provides the attractive features of local refinements and adaptive meshing. Escobar et al. [50] developed a method to generate trivariate T-splines meshes from triangular surface meshes. The parameterisation through a fully automatic process. The method firstly maps the surface mesh to a three dimensional parametric cube. Then, it generates an adapted and structured tetrahedral mesh of the parametric cube and maps its boundary back to the surface. The inner nodes should be relocated to the optimised positions using an untangling and smoothing procedure. After that, it creates an adapted T-mesh by partitioning the parametric domain in cells according to the tetrahedral parametric cube and also moves the "T-junctions" to the optimal positions calculated from the volumetric parameterisation. Zhang et al. [4] proposed a more robust and efficient algorithm for constructing rational T-splines volumetric discretisation. The procedure is illustrated in Figure 2.9. They also developed the volumetric parameterisation method for objects of genus greater than zero in [77]. Zhang et al. [78] also proposed a method to generate conformal trivariate solid T-splines directly from a T-splines surface which reached an important stage of the integration of CAD and analysis.

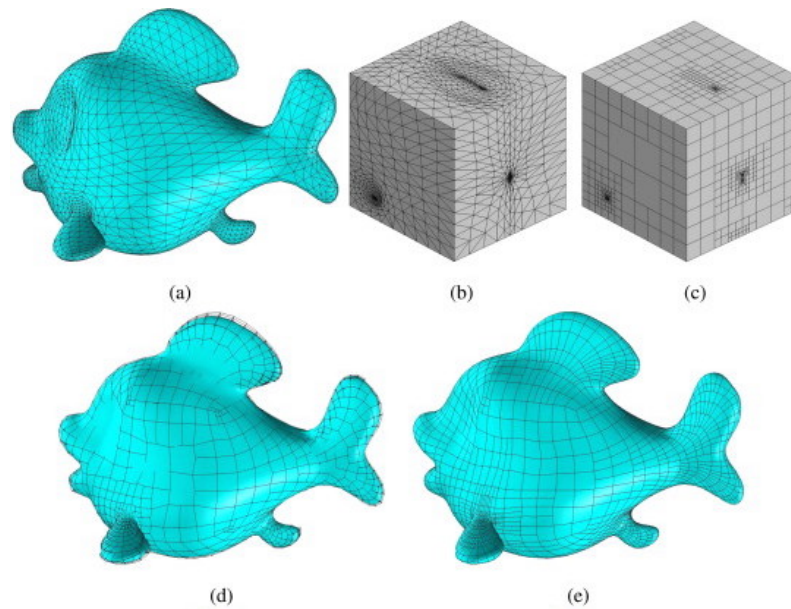


Figure 2.9: (a) A triangular surface mesh of a CAD model. (b) The mapped parametric triangular mesh on a cube. (c) The subdivision result for the parametric cube. (d) Constructing the model with T-mesh and T-spline for the geometry. (e) Applying Bézier extraction on the T-splines. Figure reproduced from [4].

2.5.2 Isogeometric shell formulations

Since volumetric parametrisation is the most challenging problem for isogeometric analysis, shell formulation, which does not require volume discretisation, is attractive to the IGA community. The IGA concept proposed in [29], uses the thin elastic shell as an example. The two-dimensional shell theory consider the structure as a curved two-dimensional surface with a relatively small shell thickness. There are two different shell theories: Kirchhoff-Love and Reissner-Mindlin. Shells are classified into "thin" and "thick" shells according to the ratio of the radius of curvature and the thickness (R/h). The Kirchhoff-Love shell theory, also referred as "classic shell model", can only describe thin shells, where $R/h \geq 20$. Reissner-Mindlin shell theory is an extension of Kirchhoff-Love theory with the shear deformations taken into account. The theory can be applied on both thin and thick shells. Reissner-Mindlin only requires C^0 continuity, while Kirchhoff-Love requires C^1 continuity of the shell surfaces. Conventional FE discretisation, such as Lagrangian discretisation, can only provides C^0 continuity across elements. So, even though most applications of shell analysis only use thin

shells, Reissner-Mindlin shell theory is more popular in finite element analysis. However, the Reissner-Mindlin shell formulation requires three additional rotational degrees of freedom at each node, which will form a larger system matrix than Kirchhoff-Love shell theory which only requires three translational degrees of freedom on each node. Therefore, Reissner-Mindlin shell formulation is more expensive than Kirchhoff-Love shell formulation. One of the advantages of the spline-based discretisations in IGA, is that they can provide at least C^1 continuity, which makes the rotation-free shell formulation (Kirchhoff-Love) easy to be implemented. The first spline-based Kirchhoff-Love shell formulation was developed by Cirak et al. [32] in 2000, which implemented the FE shell formulation with subdivision surfaces. The subdivision surfaces provide a fully C^1 conforming discretisation for Kirchhoff-Love shell formulation. After the IGA concept was proposed, Kiendl et al. [36] developed an isogeometric approach of Kirchhoff-Love shell formulation with multiple G^1 continuous NURBS patches and for conforming NURBS patches only have C^0 continuities, they also proposed a method to perform shell analysis using additional strips of fictitious material at the patch interfaces to achieve G^1 continuities across patches [59]. Benson et al. [79] developed the first isogeometric Reissner-Mindlin shell formulation for analysing large deformation problems and they also proposed an isogeometric Kirchhoff-Love theory [80]. Because the isogeometric shell formulation has various applications in manufacture industries and are also easy to implement, the shell theories are always used to test new IGA ideas. Uhm and Youn [81] implemented the T-splines in the shell analysis with the Reissner-Mindlin theory. Nguyen-Thanh et al. [46] extended the rotation-free Kirchhoff-Love thin shell analysis with PHT-splines to gain the abilities of h-adaptive refinements after they applied this advanced IGA discretisation tool on two-dimensional elastic solid analysis [82].

2.5.3 Isogeometric boundary element method

The early IGA works are predominately focused on the use of the finite element method because it is the most widely used numerical method in many applications. However, as stated in section 2.1, three dimensional finite element method requires volumetric discretisations for analysis where common CAD software normally only use boundary representation approaches,

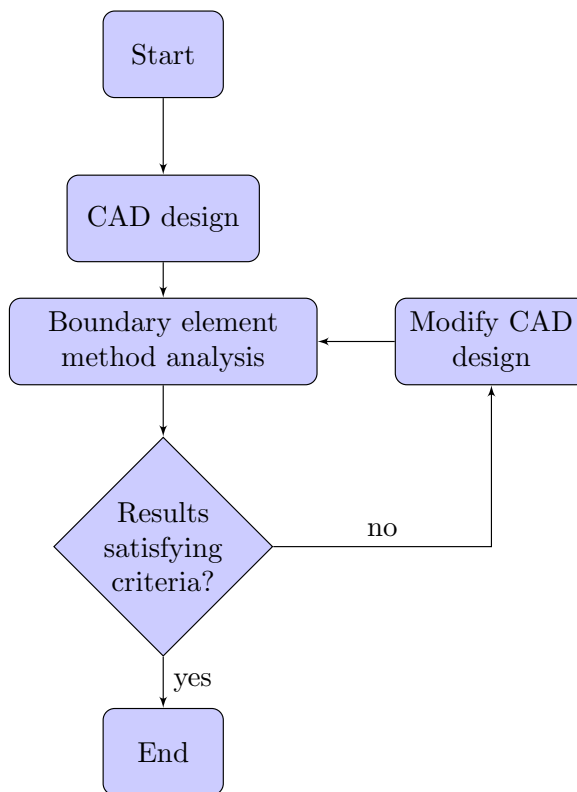


Figure 2.10: IGA workflow using BEM.

mostly NURBS surfaces, to model the geometry. The volume parameterisation of splines are complicated and costly. Boundary element method is a traditional numerical computational method which solves partial differential equations formulated as integral equations only on the boundaries. It can solve three dimensional problems in many engineering and science areas. Because boundary element method only requires the discretisation of the boundaries, it has advantages in solving external and unbounded problems, such as acoustics and electromagnetics, and it also can easily handle geometries with free or moving boundaries because its mesh regeneration algorithm is much simpler than finite element method. The aim of IGA is to integrate design and analysis using one model and BEM is the perfect match for achieving this goal. Using BEM for analysis, the engineering workflow is simplified as shown in Figure 2.10. Boundary discretisation normally has fewer degrees of freedom compared to volumetric discretisation and when the scale of the problem is relatively small, BEM can analyse the problem within a shorter period compared to the finite element method. When carrying out a conceptual design, BEM analysis can be quickly performed after each change of the

geometry. Based on this idea, Simpson et al. [83] proposed an isogeometric boundary element method, termed as IGABEM, to analyse two-dimensional elastostatic problems with NURBS basis functions. They showed that a seamless design-through-analysis process can be achieved by using isogeometric boundary element method (IGABEM). IGABEM is a full integration of CAD and analysis. Takahashi and Matsumoto [84] also implemented an isogeometric boundary element method for two dimensional Laplace problems. They adopted the fast multipole method to accelerate the matrix construction process. After that, Scott et al. [85] coupled unstructured T-splines with isogeometric boundary element method to perform three dimensional analysis of linear elastostatic problems. Peake et al. [86] extended the IGABEM for the application of acoustics. They employed partition-of-unity enriched NURBS functions into two dimensional Helmholtz problems. Simpson et al. [87] demonstrated three dimensional acoustic scattering simulations using isogeometric boundary element method with T-splines, which showed the superior accuracy of IGABEM in unbounded problems.

However, the weaknesses of boundary element method are also very obvious and insurmountable. The boundary element method requires the explicit fundamental solutions of the governing equations, which restrict the method to solve non-linear problems which analytical solution are hard to obtain. Recent works to couple isogeometric boundary element method with other method for solving complicated problems include [88]. The kernel functions in boundary element method are normally singular and are difficult to be integrated accurately. Regularisation methods are used to overcome this weakness but still have difficulties in extreme situations, such as hyper-singular kernels in Burton-Miller method [89]. A more serious limitation of boundary element method is that the matrices which construct the system of equations are fully populated. When the scale of the problem becomes larger, the time to construct the matrices and solve this system of equation increase more rapidly than finite elements which produces sparse system matrices. The IGA uses spline functions which are difficult to compute make the analysis more time-consuming. Accelerating methods, e.g. fast multipole method [90] and hierarchical matrices [91, 92] are used to reduce the total computational time. Boundary element method can also adopt a collocation approach to formulate the system of equations which massively reduce the time of constructing the matrices.

2.6 Summary

The developments of IGA focused on addressing the three limitations of current computer-aided design techniques. The NURBS surfaces are the dominant technology in the CAD market, but it is generated as a tensor-product of two NURBS curves which restricts the NURBS from modelling complex geometries with arbitrary topologies. Two research directions are derived in order to solve this problem. One is to use special treatments of NURBS surfaces to perform analysis, including trimmed NURBS surfaces and NURBS patch coupling method. The other research direction is to develop analysis-suitable CAGD techniques. Notable developments include T-splines, hierarchical B-splines, PHT-splines and LR B-splines. The subdivision surfaces is a mature CAD technique which is already widely used in animation and gaming industries. It is based on a relatively simple principle to represent smooth surfaces and the surfaces also can be evaluated with spline functions. The truncated subdivision surfaces can be locally refined and applied adaptive meshing schemes.

However, the most challenging issue in the developments of isogeometric analysis is that all the CAD models use boundary representative techniques but the numerical methods always require volumetric discretisations. In order to achieve a fully integration of design and analysis, the parameterisation from bivariate spline-based surface into trivariate spline based solid has been developed. Both shell formulation and boundary element method only require a surface discretisation of the geometries which can also overcome this challenge.

Chapter 3

CAGD fundamental techniques

This chapter will provide further details on the theory of two fundamental Computer Aided Geometry Design (CAGD) techniques introduced briefly in the previous chapter which are widely used in commercial software: Non-Uniform Rational B-Splines (NURBS) and subdivision surfaces. Section 3.1.1 will use B-spline curve as a starting point to introduce spline based geometry discretisations, followed by the theory of NURBS, which is a general extension of B-spline. Then the theory of two dimensional NURBS surfaces are illustrated. h - and p -refinement methods for NURBS are introduced in Section 3.1.4. Bézier extraction method provides a data structure of NURBS for analysis and will be explained in Section 3.1.5. Section 3.2.1 will introduce different subdivision algorithms for constructing curves and Section 3.2.2 and Section 3.2.3 will introduce Catmull-Clark and Loop subdivision surfaces respectively. The last section 3.2.4 will illustrate the evaluation method of Loop subdivision surfaces, which is used in present work.

3.1 B-splines and NURBS

3.1.1 B-spline curves

In the current Computer Aided Design market, the most commonly used geometry representation tool is NURBS, which is a general extension of B-splines to gain more control over the geometry. A spline is defined as a piecewise polynomial function which can interpolate

curves with a guaranteed level of continuity. The parametric domain of a spline is divided into segments by a knot vector ξ . A knot vector is a set of coordinates in the parametric space, written as $\xi = \{\xi_1, \xi_2, \dots, \xi_i, \dots, \xi_{n_c+n_p+1}\}$, where ξ_i is the i^{th} knot, i is the knot index, n_p refers to the polynomial order, and n_c is the total number of control points of the spline curve. The whole parametric space of a spline can be seen as a patch of elements and the sub-domains between two adjacent knots are the elements. A B-spline basis function N_{i,n_p} has a general form defined as:

for $n_p = 0$:

$$N_{i,0}(\xi) = \begin{cases} 1 & \text{if } \xi_i \leq \xi < \xi_{i+1}, \\ 0 & \text{otherwise,} \end{cases} \quad (3.1)$$

while for $n_p = 1, 2, 3, \dots$:

$$N_{i,n_p}(\xi) = \frac{\xi - \xi_i}{\xi_{i+n_p} - \xi_i} N_{i,n_p-1}(\xi) + \frac{\xi_{i+n_p+1} - \xi}{\xi_{i+n_p+1} - \xi_{i+1}} N_{i+1,n_p-1}(\xi), \quad (3.2)$$

where ξ is the parametric coordinate and N_{i,n_p} denotes the i^{th} basis function with order n_p B-spline. This formulation is called the *Cox-de Boor recursion formula* [93, 94]. To understand these basis functions, an example of B-spline curve is shown in Figure 3.1 and a plot of the basis functions is showed in Figure 3.2. In this example, the B-spline curve has a knot vector $\xi = \{0, 0, 0, 0.2, 0.4, 0.6, 0.8, 0.8, 1.0, 1.0, 1.0\}$ with $n_p = 2$. The point on the B-spline curve are evaluated as:

$$\mathbf{S}(\xi) = \sum_{i=1}^{n_c} N_{i,n_p}(\xi) \mathbf{P}_i,$$

where $\mathbf{S} \in \mathbb{R}^3$ is the physical coordinates of a surface point on the curve. $\mathbf{P}_i \in \mathbb{R}^3$ denotes the physical coordinates of i^{th} control point. This example curve has $n_c = 8$ control points where each associates with one basis function. The knot vector ξ has six non-repeated knots which divide the B-spline curve into five elements. The first and last knots ξ_1 and ξ_6 are repeated $n_p + 1$ times in the knot vector, which ensure that the vector is an open knot vector. An open knot vector defines a separated B-spline patch. Generally, the B-spline curve with order n_p has C^{n_p} continuity everywhere except C^{n_p-1} the locations of the knots. The continuities at the knot will decrease to C^{n_p-k} if the knot repeat k times in the knot vector. For example, the curve in

Figure 3.1 has two open end knots ξ_1 and ξ_6 . It has C^2 everywhere except the locations of knots ξ_2, ξ_3, ξ_4 and ξ_5 . The continuity at knot ξ_5 decreases to C^0 because it repeated twice in the vector while the other knots can keep C^1 continuities.

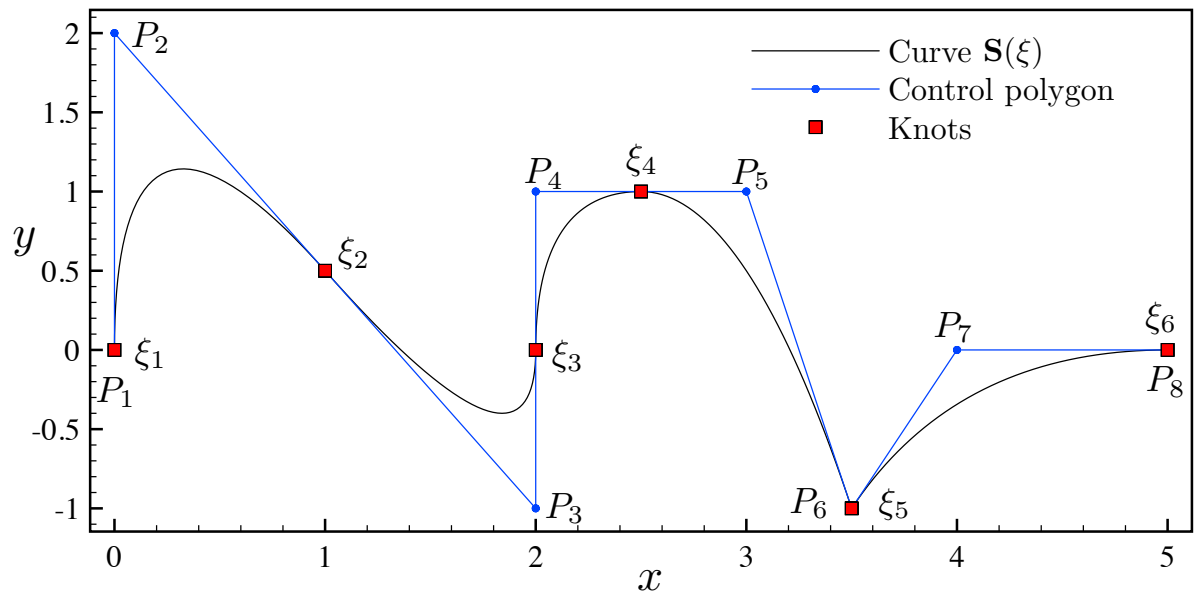


Figure 3.1: An example B-spline curve with $\xi = \{0, 0, 0, 0.2, 0.4, 0.6, 0.8, 0.8, 1.0, 1.0, 1.0\}$, $n_c = 8$ and $n_p = 2$.

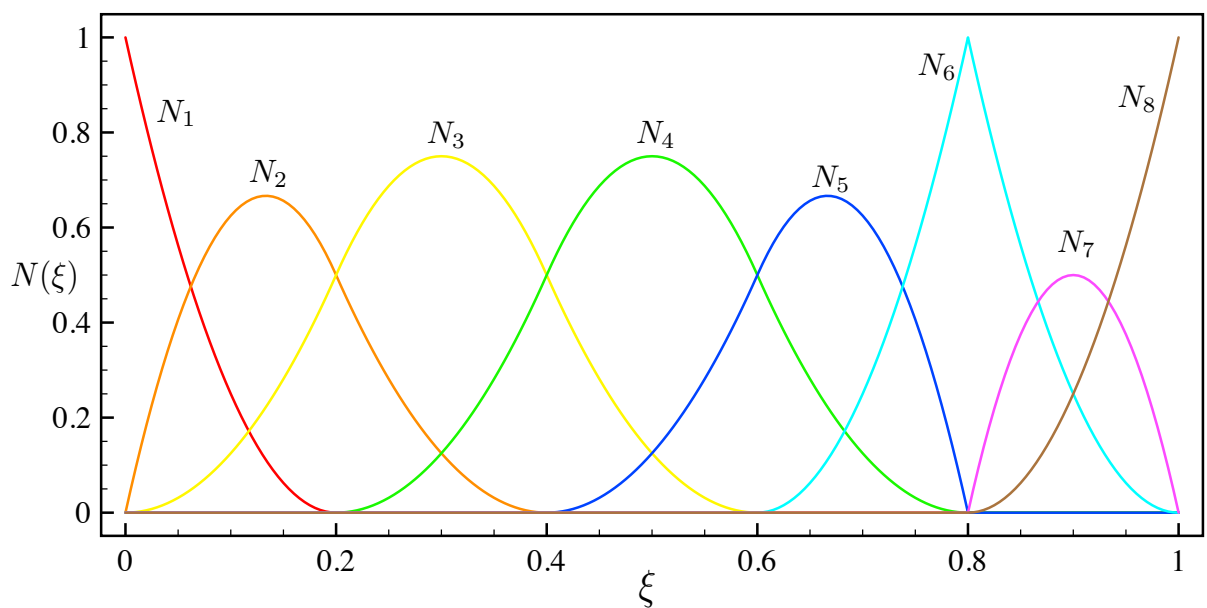


Figure 3.2: Quadratic basis functions for the B-spline curve.

The B-spline basis function, shown in Figure 3.2, N_{i,n_p} is only non-zero in the span between knots ξ_i and ξ_{i+n_p+1} . It means the basis functions locally support the curve. By changing one of the control points, it only affects a specific region of the curve and other parts will remain the same. For a parametric coordinate ξ in any location, the sum of the basis functions equal to 1.0, i.e. $\sum_{i=1}^n N_{i,n_p} = 1.0$, and all the basis functions are non-negative. However, different from Lagrange polynomials, B-splines can have more than one non-zero basis functions at knots (element boundary points).

3.1.2 Non-Uniform Rational B-Splines curves

'Non-uniform' means the knots of the spline are not equally-spaced in the parametric domain. This allows for special local adjustments in specific regions of the curve which is essential for modelling a complex geometry. The basis functions defined in Equation 3.2 is a non-uniform B-spline function. In Section 3.1.4, the method of inserting new knots will be introduced. The knots can be inserted in any parametric location without changing the geometry to create non-uniform B-spline curves. Uniform B-spline curves are a special case of non-uniform B-spline curves.

The non-uniform B-spline gives more controls over the curve than uniform B-spline, but it is still impossible to model exact geometries, such as circles and ellipses, that can not be modelled with low-order B-spline curves. One of the solutions to model these geometries is to use "rational B-spline curves". "Rational B-spline curves" means the objects modelled by the spline can be expressed by rational polynomials. It associates a "weight" with each control point allowing the flexibility to drag and push the curve closer or further away from the corresponding control point by changing the weight. This method does not create additional control points and also preserve the original continuity. For a control point $\mathbf{P}_i = [x_i, y_i, z_i]$, a "weight" w_i is associated. The homogeneous coordinates (one order higher than normal Cartesian coordinates) of the control point \mathbf{P}_{iH} are defined by

$$\mathbf{P}_{iH} = [x_i w_i, y_i w_i, z_i w_i, w_i]^T.$$

Then, the B-spline curve point \mathbf{S}_H is expressed as

$$\mathbf{S}_H(\xi) = \sum_{i=1}^{n_c} N_{i,n_p}(\xi) \mathbf{P}_{iH}.$$

It can be converted back to Cartesian coordinate system by dividing $\mathbf{S}_H(\xi)$ by the fourth coordinate $w(\xi)$, where

$$w(\xi) = \sum_{i=1}^{n_c} w_i N_{i,n_p}(\xi).$$

The expression for \mathbf{S} becomes

$$\mathbf{S}_H(\xi) = \sum_{i=1}^{n_c} \frac{N_{i,n_p}(\xi) w_i}{\sum_{j=1}^{n_c} N_{j,n_p}(\xi) w_j} \begin{bmatrix} x_i \\ y_i \\ z_i \\ 1 \end{bmatrix}. \quad (3.3)$$

or in terms of the first three components

$$\mathbf{S}(\xi) = \frac{1}{\sum_{j=1}^{n_c} N_{j,n_p}(\xi) w_j} \sum_{i=1}^{n_c} N_{i,n_p}(\xi) w_i \mathbf{P}_i,$$

and the equation can be simplified to

$$\mathbf{S}(\xi) = \sum_{i=1}^{n_c} R_{i,n_p}(\xi) \mathbf{P}_i,$$

where

$$R_{i,n_p}(\xi) = \frac{N_{i,n_p}(\xi) w_i}{\sum_{j=1}^{n_c} N_{j,n_p}(\xi) w_j}.$$

The sum of rational basis functions $\sum R_i = 1.0$, and one can control the curve by changing the weight of the corresponding control point (basis function). If all weights are equal to one, the NURBS curve will reduce to a B-spline curve. Figure 3.3 shows a comparison between B-spline curve and a NURBS curve. The NURBS has a weight vector $\{1, 2, 1, 2, 1, 1, 2, 1\}$ and is therefore moved closer to the corresponding control points \mathbf{P}_2 , \mathbf{P}_4 and \mathbf{P}_7 .

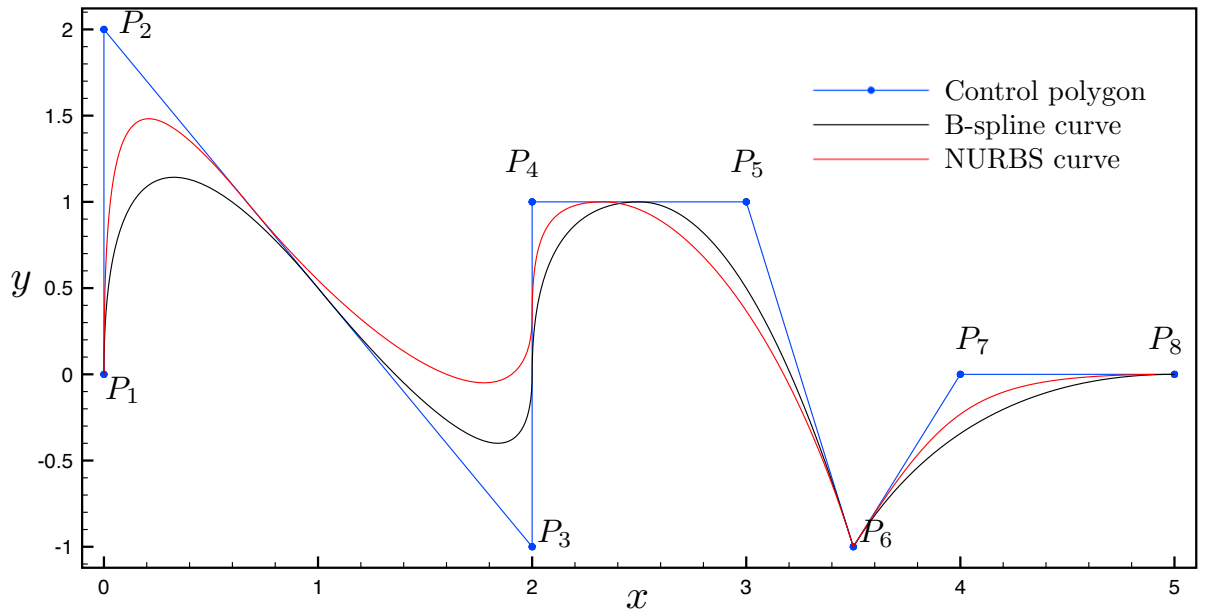


Figure 3.3: A comparison between a B-spline and a NURBS curve with a weight vector $\{1, 2, 1, 2, 1, 1, 2, 1\}$.

3.1.3 NURBS surfaces

CAD software often uses a surface representation for three dimensional modelling. The most widely adopted surface representation is the NURBS. The NURBS surfaces are based on the concept of bilinear patches, which is the simplest CAD surface and can be seen as a unique case of NURBS surface. The surface has a simple expression given by

$$\mathbf{S}(u, v) = \mathbf{P}_1(1 - u)(1 - v) + \mathbf{P}_2(1 - u)v + \mathbf{P}_3u(1 - v) + \mathbf{P}_4uv, \quad (3.4)$$

where \mathbf{S} is a surface point on a bilinear patch and \mathbf{P}_1 , \mathbf{P}_2 , \mathbf{P}_3 and \mathbf{P}_4 are the coordinate vectors of the four control points, and u and v are the parametric coordinate components. The NURBS surface also has parametric directions but the surface points are interpolated with B-spline basis functions including an additional fourth component, known as a weight, which allows geometries, such as cones, spheres and ellipsoids to be represented exactly. A NURBS surface point is defined by

$$\mathbf{P}(u, v) = \frac{\sum_{i=1}^m \sum_{j=1}^n w_{i,j} \mathbf{P}_{i,j} N_i^m(u) N_j^n(v)}{\sum_{i=1}^m \sum_{j=1}^n w_{i,j} N_i^m(u) N_j^n(v)}, \quad (3.5)$$

where m and n are the numbers of control points in the two directions, and N^m and N^n are two sets of B-splines basis functions in two directions expressed using Equation 3.1 and Equation 3.2, i and j are the indices for the control points in two directions, and $w_{i,j}$ is the weight of point $P_{i,j}$. Figure 3.4 shows an example of NURBS surface with 16 control points.

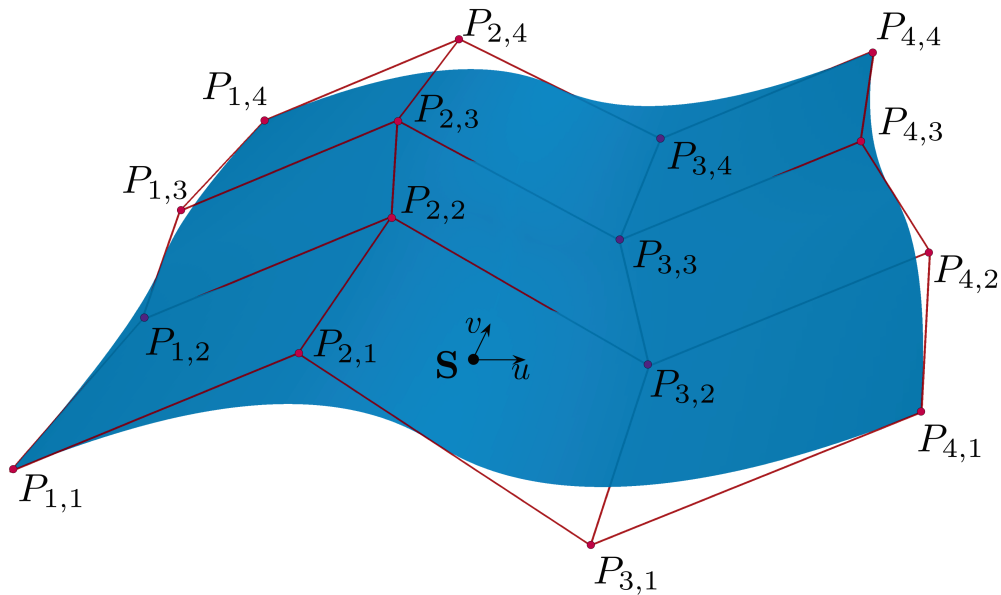


Figure 3.4: An example of a NURBS surface.

3.1.4 Refinement

In Section 3.1.1, the commonly used CAD tool non-uniform rational B-splines was introduced. One of the interesting properties of NURBS is that it allows subdivision and order elevation of the spline without changing the geometry through inserting a number of new knots into the knot vector. A curve can be defined by various combinations of knot vectors and control points. It is very useful in analysis as it easily allows for h - and p -refinement of the discretisation of the

geometry.

Knot insertion We first introduce how to insert a knot into the parametric domain of a B-spline or NURBS curve. Assume a B-spline curve has a knot vector $\xi = \{\xi_1, \xi_2, \dots, \xi_{n_c+n_p+1}\}$. Insert a knot $\bar{\xi}$ into the knot vector ξ and assume the knot is located between ξ_k and ξ_{k+1} . The new knot vector will thus be $\xi = \{\xi_1, \xi_2, \dots, \xi_k, \bar{\xi}, \xi_{k+1}, \dots, \xi_{n_c+n_p+1}\}$. The number of new control points will be increased by one, i.e. $n_c + 1$. The new set of control points is computed as

$$\bar{\mathbf{P}}_i = \begin{cases} \mathbf{P}_1, & i = 1. \\ \alpha_i \mathbf{P}_i + (1 - \alpha_i) \mathbf{P}_{i-1}, & 1 < i < n_c + 1. \\ \mathbf{P}_{n_c}, & i = n_c + 1. \end{cases} \quad (3.6)$$

$$\alpha_i = \begin{cases} 1, & 1 \leq i \leq k - n_p. \\ \frac{\bar{\xi} - \xi_i}{\xi_{i+n_p} - \xi_i}, & k - n_p + 1 \leq i \leq k. \\ 0, & i \geq k + 1. \end{cases} \quad (3.7)$$

***h*-refinement** The "*h*" in "*h*-refinement" refers the sizes of elements, hence "*h*-refinement" means subdivide the elements into smaller elements. Uniformly inserting new knots will uniformly subdivide the parametric domain of the NURBS curve. NURBS allows to be non-uniformly refined, which is a generalisation of B-splines introduced in Section 3.1.1. Figure 3.5 shows an example of applying uniform *h*-refinement on a NURBS curve. The initial knot vector is $\xi = \{0, 0, 0, 0.2, 0.4, 0.6, 0.8, 0.8, 1, 1, 1\}$ and the refined knot vector is $\bar{\xi} = \{0, 0, 0, 0.1, 0.2, 0.3, 0.4, 0.5, 0.6, 0.7, 0.8, 0.8, 0.9, 1, 1, 1\}$. The number of control points has increased from 8 to 13.

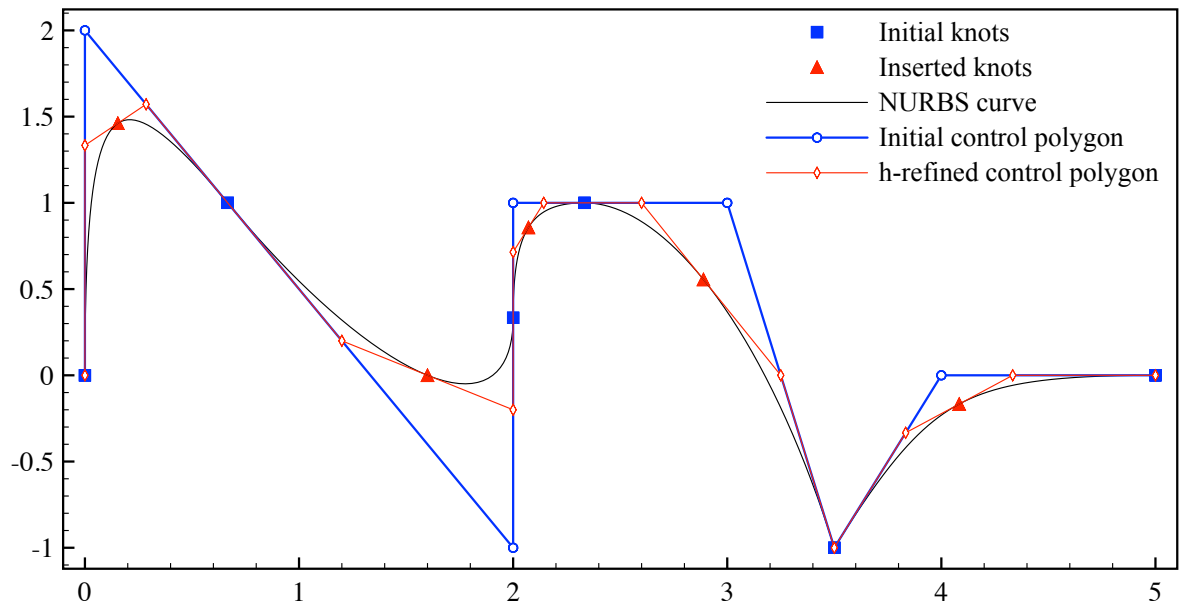
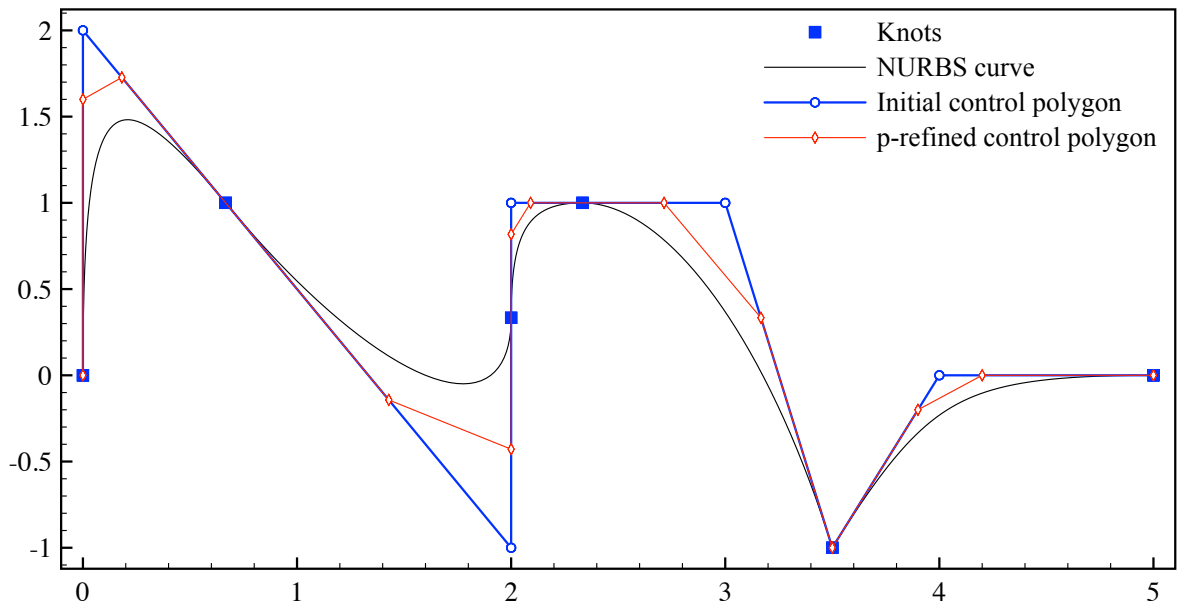


Figure 3.5: An example of h -refinement of NURBS.

p -refinement p -refinement elevates the polynomial order of the NURBS curve without changing the geometry and the number of elements. The method firstly subdivides the curve into a number of Bézier curves by repeating knots (this method will be introduced in Section 3.1.5) and elevating the order of these individual Bézier curves. After that, it combines these curves into one new NURBS curve of higher order by removing the unnecessary knots. Figure 3.6 use the same curve to show the effect of p -refinement. After elevating the polynomial order by one, the refined knot vector becomes $\bar{\xi} = \{0, 0, 0, 0, 0.2, 0.2, 0.4, 0.4, 0.6, 0.6, 0.8, 0.8, 0.8, 1, 1, 1, 1\}$. Every unique knot in the vector has been repeated once to retain the original continuities. The number of control points is increased from 8 to 13, but the element number stays the same.

Figure 3.6: An example of p -refinement of NURBS.

3.1.5 Bézier extraction

Bézier decomposition Bézier decomposition repeats all interior knots to discretise the spline curve into piecewise Bézier elements. The interior knots are repeated to have multiplicities equal to n_p .

Take a B-spline as an example, a cubic B-spline has a knots vector $\xi = \{0, 0, 0, 0, 1, 2, 3, 4, 4, 4, 4\}$. The interior knots should have multiplicities equal to 3. In order to apply Bézier composition on this B-spline, the knots 1, 2 and 3 will be repeated twice to achieve a new knot vector $\bar{\xi} = \{0, 0, 0, 0, 1, 1, 1, 2, 2, 2, 3, 3, 3, 4, 4, 4, 4\}$ using the method introduced in Section 3.1.4. Repeating the interior knot once will reduce the continuity of the basis by one but the continuity of the resulting curve will be unchanged. The method creates additional control points at the positions of the knots to break the patch into Bézier elements. Figure 3.7 shows a B-spline is decomposed into a number of Bézier curves and Figure 3.8 shows an example of the piecewise basis functions.

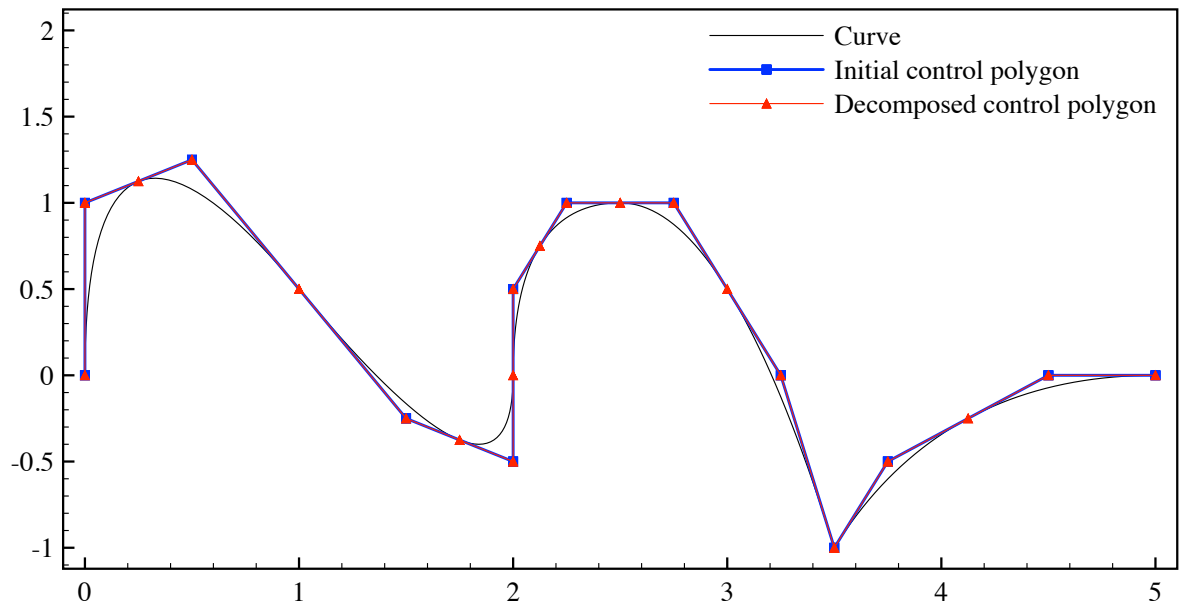


Figure 3.7: An example Bézier extraction of a B-spline curve with knot vector $\xi = \{0, 0, 0, 0.1, 0.2, 0.3, 0.4, 0.5, 0.6, 0.7, 0.8, 0.8, 0.9, 1, 1, 1\}$.

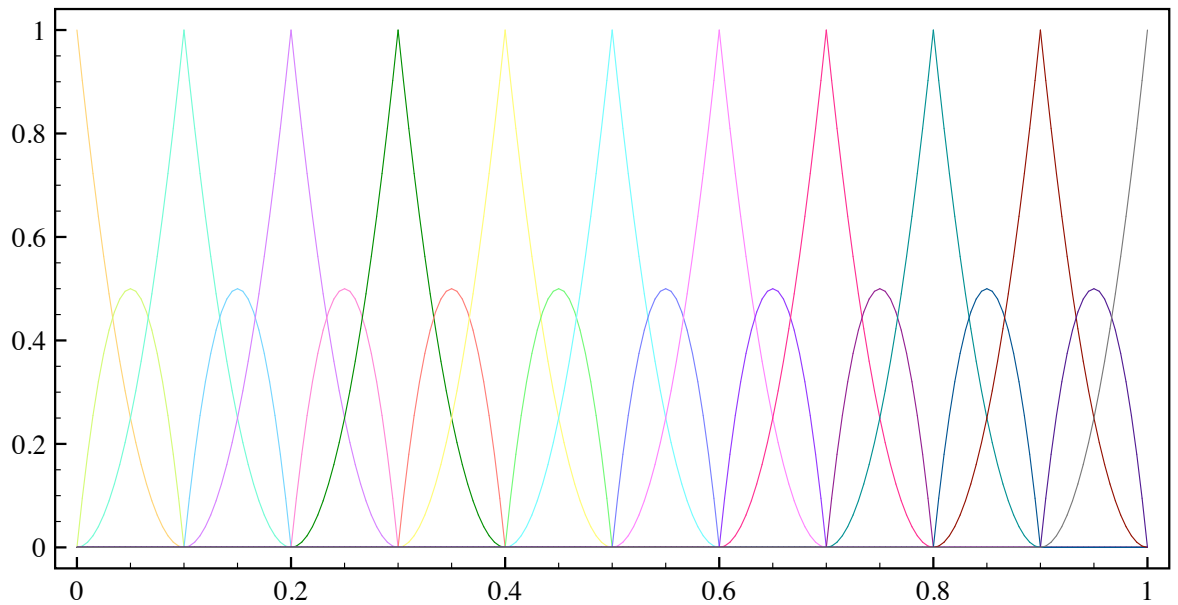


Figure 3.8: Plots of piecewise Bézier basis functions of the curve shown in Figure 3.7.

Computing the Bézier extraction operator Given a NURBS curve with a knot vector $\xi = \{\xi_1, \xi_2, \dots, \xi_{n_c+n_p+1}\}$ and the set control points is $\mathbf{P} = \{\mathbf{P}_i\}_{i=1}^{n_c}$. To achieve the Bézier

decomposition, a set of new knots, $\{\bar{\xi}_1, \bar{\xi}_2, \dots, \bar{\xi}_m\}$, should be inserted into the initial knot vector. Denote the j^{th} new knot as $\bar{\xi}_j$, where $j = 1, 2, \dots, m$. Then, for j^{th} inserting knot, the new control points after the knot insertion can be generated from the old control points as

$$\bar{\mathbf{P}}^{j+1} = [\mathbf{C}^j]^T \bar{\mathbf{P}}^j,$$

where the matrix \mathbf{C}^j can be generated as

$$\mathbf{C}^j = \begin{bmatrix} \alpha_1 & 1 - \alpha_2 & 0 & \dots & & 0 \\ 0 & \alpha_2 & 1 - \alpha_3 & 0 & \dots & 0 \\ 0 & 0 & \alpha_3 & 1 - \alpha_4 & 0 & \dots & 0 \\ \vdots & & & & & & \\ 0 & \dots & & & 0 & \alpha_{(n+j-1)} & 1 - \alpha_{n+j} \end{bmatrix},$$

where the coefficient α_i^j can be calculated using Equation 3.7 for the i^{th} inserting knot.

After inserting m knots, the final set of control points $\bar{\mathbf{P}}^{m+1}$ will represent the result of Bézier decomposition. Let $\mathbf{P}^b = \bar{\mathbf{P}}^{m+1}$ and define $\mathbf{C}^T = [\mathbf{C}^m]^T [\mathbf{C}^{m-1}]^T \dots [\mathbf{C}^1]^T$ and the resulting control points of the Bézier decomposition are written as

$$\mathbf{P}^b = \mathbf{C}^T \mathbf{P}. \quad (3.8)$$

The geometry of the curve remain the same during the knot inserting process, thus we have

$$[\mathbf{P}^b]^T \mathbf{B}(\xi) = \mathbf{P}^T \mathbf{N}(\xi),$$

where \mathbf{B} is a vector form of Bernstein polynomial functions. Rewrite $[\mathbf{P}^b]^T \mathbf{B}(\xi)$ with Equation 3.8 yields

$$[\mathbf{P}^b]^T \mathbf{B}(\xi) = [\mathbf{C}^T \mathbf{P}]^T \mathbf{B}(\xi) = \mathbf{P}^T \mathbf{C} \mathbf{B}(\xi).$$

Then, the B-spline basis function can be written as a product of matrix \mathbf{C} and Bernstein basis

functions.

$$\mathbf{N}(\xi) = \mathbf{CB}(\xi).$$

The matrix \mathbf{C} is called the *Bézier extraction operator*.

Evaluation of NURBS surfaces using Bézier elements Although a NURBS curve is naturally divided into a number of elements by the knot vector, the NURBS basis functions are not efficient for analysis. The NURBS basis functions, introduced in Section 3.1.1, are based on B-spline basis functions. A NURBS curve normally has a number of basis functions which are continuous on different elements, see Figure 3.2. When evaluating one of the elements in a NURBS patch, the B-spline basis functions should be computed using recursive functions (see Equations 3.1 and 3.2) which means they are very expensive when used for analysis. Bézier extraction operator maps a NURBS into a number of Bézier elements. Bézier elements are considered more efficient for analysis because they can be evaluated with Bernstein polynomial basis functions which are simple and consistent in all the elements. All elements have the same $n_p + 1$ basis functions and the i^{th} Bernstein polynomial basis of an order n_p Bézier curve is computed with a simpler formulation by

$$B_i(\xi) = \binom{n_p}{i-1} \xi^{i-1} (1-\xi)^{n_p-(i-1)}, i = 1, 2, 3, \dots, n_p + 1,$$

where the binomial coefficients are calculated as

$$\binom{n_p}{i-1} = \begin{cases} \frac{n_p!}{(i-1)!(n_p+1-i)!} & \text{if } 1 \leq i \leq n_p + 1, \\ 0 & \text{else.} \end{cases}$$

There are $n_p + 1$ polynomial basis functions for a Bézier curve with degree n_p . The Bézier extraction provides a good element structure for numerical analysis. Figure 3.9 shows the mapping between Bézier element and a NURBS surface. The Bézier element is an analysis element with a parametric domain $[-1, 1] \times [-1, 1]$. Every point in this domain can be mapped onto a parametric point on a NURBS surface which has a domain $[0, 1] \times [0, 1]$. This mapping

method allows one to use two different discretisations to separate the geometry representation and analysis. The geometry can be represented using lower-order NURBS surfaces, and the analysis model can consist of a number of Bézier elements which use Bernstein polynomial basis functions for evaluation. The analysis model can easily apply h - and p -refinements without changing the geometry.

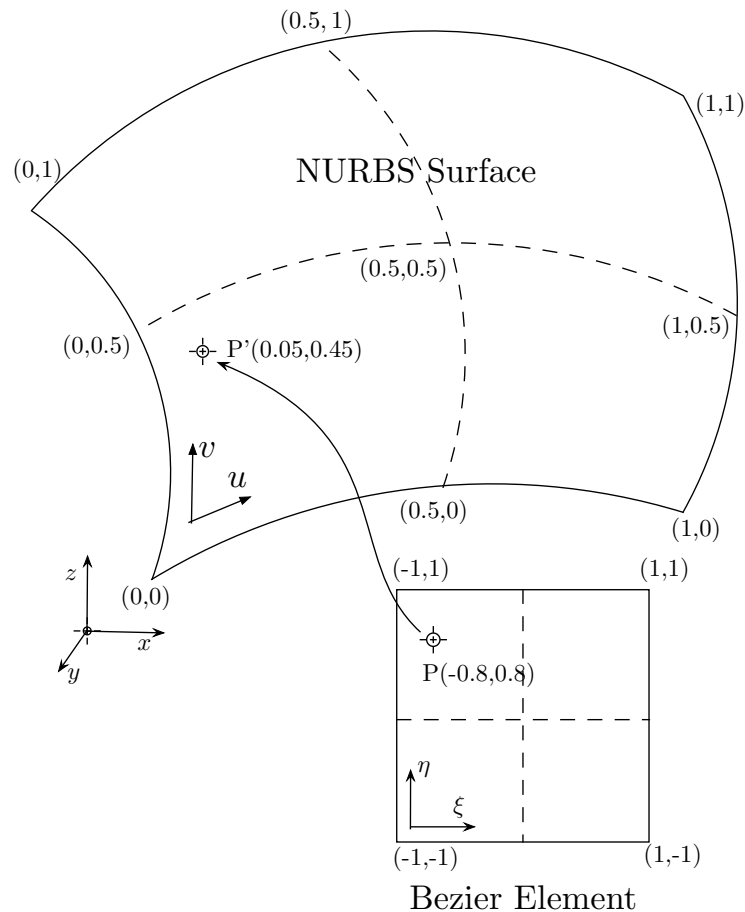


Figure 3.9: Mapping from Bézier element integration domain to NURBS parametric domain.

3.2 Subdivision curves and surfaces

Subdivision surfaces is a mature geometry discretisation technology with history dating back to the late 1970s. It is also derived from B-splines but in a different way to NURBS. There exist a variety of subdivision schemes, but the basic idea is to use a subdivision scheme to generate a smooth surface through a limiting procedure of repeated refinement steps starting from an initial polygon grid. Compared with NURBS, subdivision surfaces has the advantage of using a single

polygonal mesh to represent complex geometries with arbitrary topology.

3.2.1 Curves

Chaikin's algorithm The concept of subdivision surfaces can be explained starting with a basic subdivision curve, Chaikin's curves. Constructing a subdivision curve requires a control polygon and a subdivision algorithm. A recursive refinement scheme is used to generate new polygons from the initial control polygon. The result of the limiting process is a smooth subdivision curve. Chaikin's algorithm is a corner cutting scheme which successively cut the corner with a fixed ratio. The algorithm is given as:

- Given an initial control polygon $(\mathbf{P}_0^0, \mathbf{P}_1^0, \mathbf{P}_2^0, \mathbf{P}_3^0, \dots, \mathbf{P}_n^0)$.
- Apply first level of refinement by calculating:

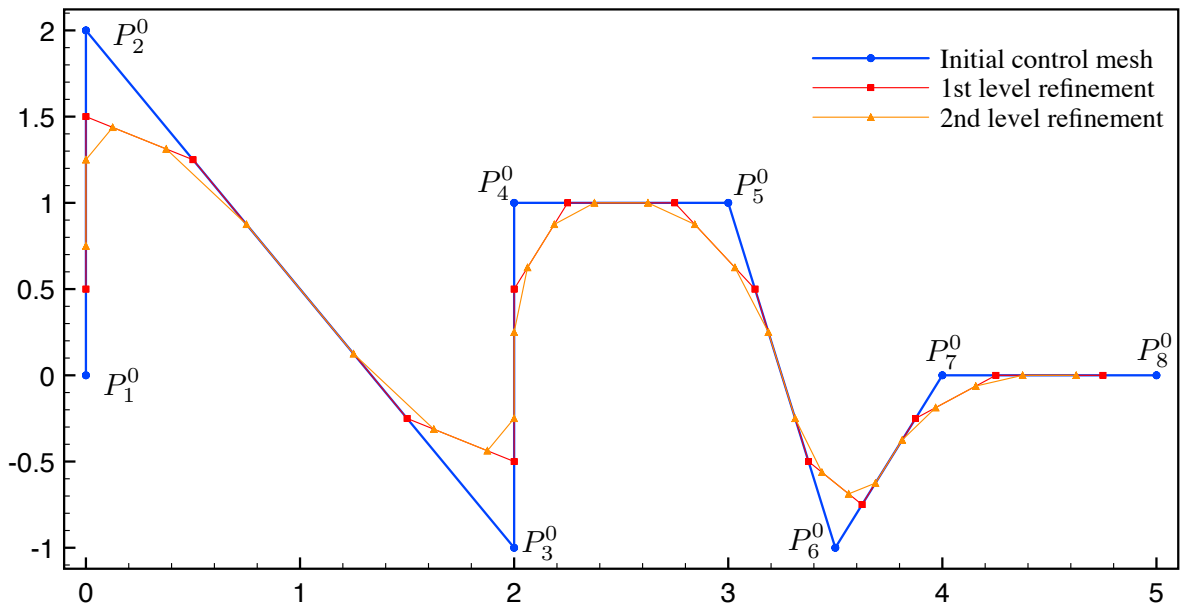
$$\left\{ \begin{array}{l} \mathbf{P}_0^1 = \frac{3}{4}\mathbf{P}_0^0 + \frac{1}{4}\mathbf{P}_1^0, \mathbf{P}_1^1 = \frac{1}{4}\mathbf{P}_0^0 + \frac{3}{4}\mathbf{P}_1^0, \\ \mathbf{P}_2^1 = \frac{3}{4}\mathbf{P}_1^0 + \frac{1}{4}\mathbf{P}_2^0, \mathbf{P}_3^1 = \frac{1}{4}\mathbf{P}_1^0 + \frac{3}{4}\mathbf{P}_2^0, \\ \dots \\ \mathbf{P}_{2n-2}^1 = \frac{3}{4}\mathbf{P}_{n-1}^0 + \frac{1}{4}\mathbf{P}_n^0, \mathbf{P}_{2n-1}^1 = \frac{1}{4}\mathbf{P}_{n-1}^0 + \frac{3}{4}\mathbf{P}_n^0. \end{array} \right.$$

- Apply i^{th} level of refinement on j^{th} segment using equations:

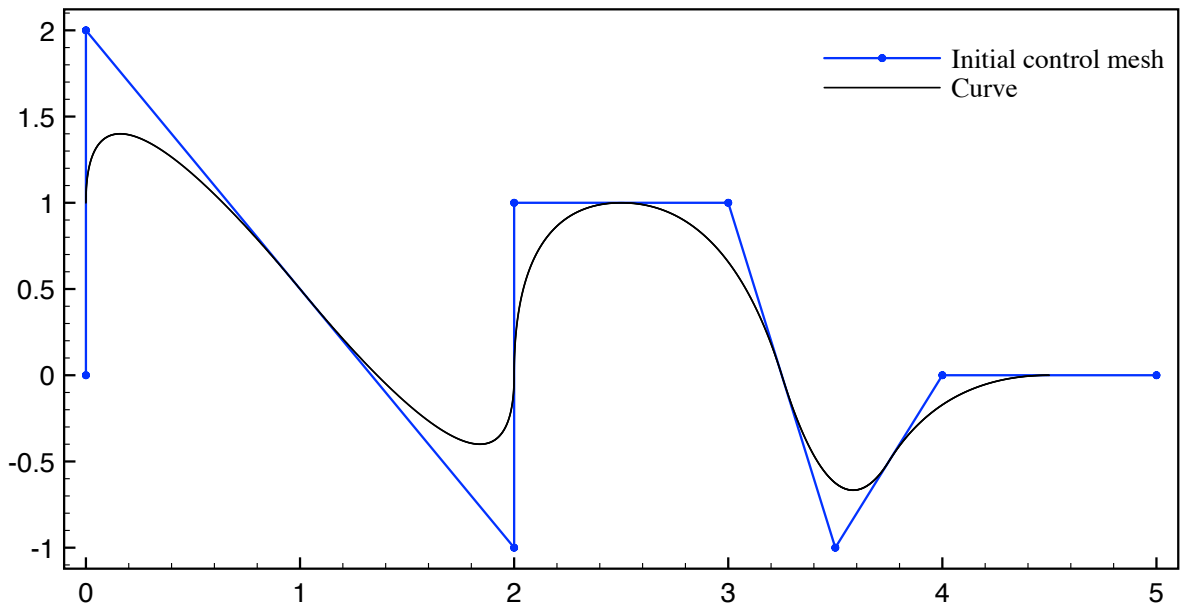
$$\left\{ \begin{array}{l} \mathbf{P}_{2j}^i = \frac{3}{4}\mathbf{P}_j^{i-1} + \frac{1}{4}\mathbf{P}_{j+1}^{i-1}, \\ \mathbf{P}_{2j+1}^i = \frac{1}{4}\mathbf{P}_j^{i-1} + \frac{3}{4}\mathbf{P}_{j+1}^{i-1}. \end{array} \right.$$

- The limit of the algorithm is Chaikin's curve.

Figure 3.10a shows the successive refinement process and Figure 3.10b shows the curve which is the limit result of the algorithm. The work [95] has shown that the limiting curve of a Chaikin's curve is identical to a quadratic B-spline curve.



(a) Successive refinements for constructing subdivision curves.



(b) A Chaikin's Curve with its control polygon.

Figure 3.10: Chaikin's Algorithm

Catmull-Clark algorithm Motivated by Chaikin's curve, Catmull and Clark [96] developed the bicubic B-spline patch subdivision algorithm for describing smooth three dimensional objects. Catmull-Clark subdivision surfaces are widely used in the animation and gaming

industries. Catmull-Clark subdivision surfaces are derived as tensor-products of Catmull-Clark curves, but do not have the limitations of tensor-product-based NURBS surfaces. Using the same idea of the Chaikin's algorithm, Catmull-Clark algorithm successively refines a curve starting from an initial set of control points and the curve is limited to a cubic B-spline curve.

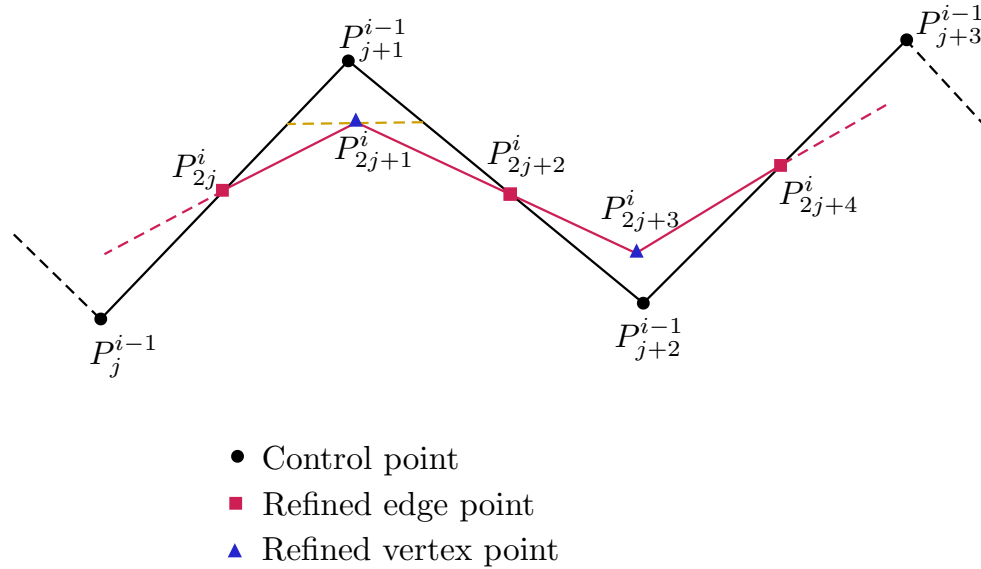


Figure 3.11: Computing new control points through the Catmull-Clark algorithm.

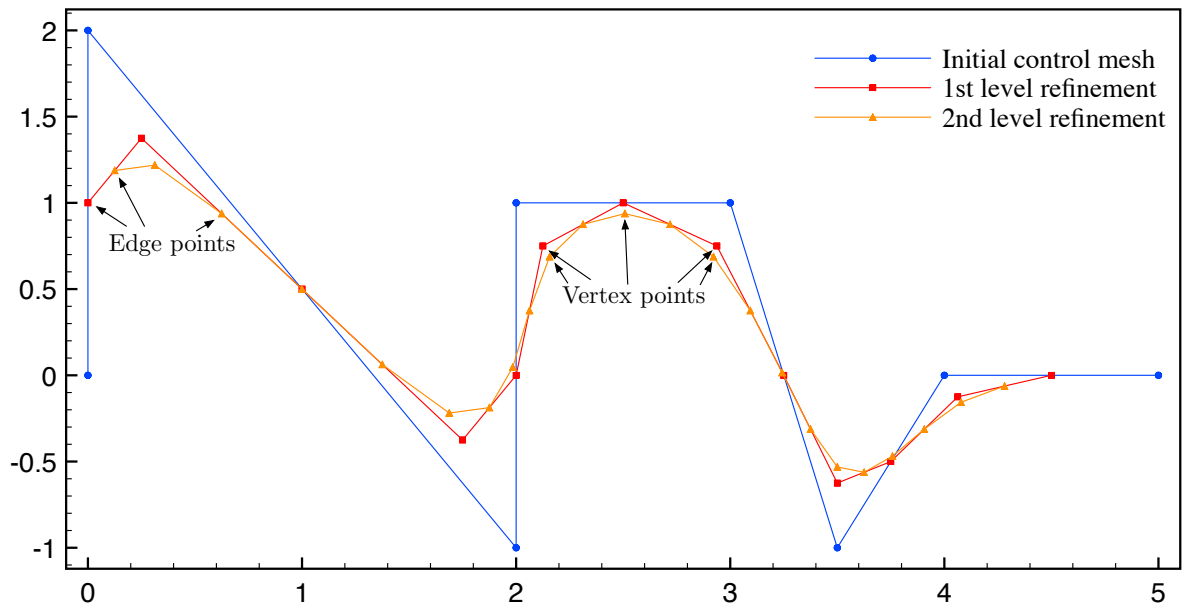
Figure 3.11 shows an example of Catmull-Clark algorithm. The control point \mathbf{P}_{2j}^i in the i^{th} level of refinement is computed as:

$$\mathbf{P}_{2j}^i = \frac{1}{2}\mathbf{P}_j^{i-1} + \frac{1}{2}\mathbf{P}_{j+1}^{i-1}.$$

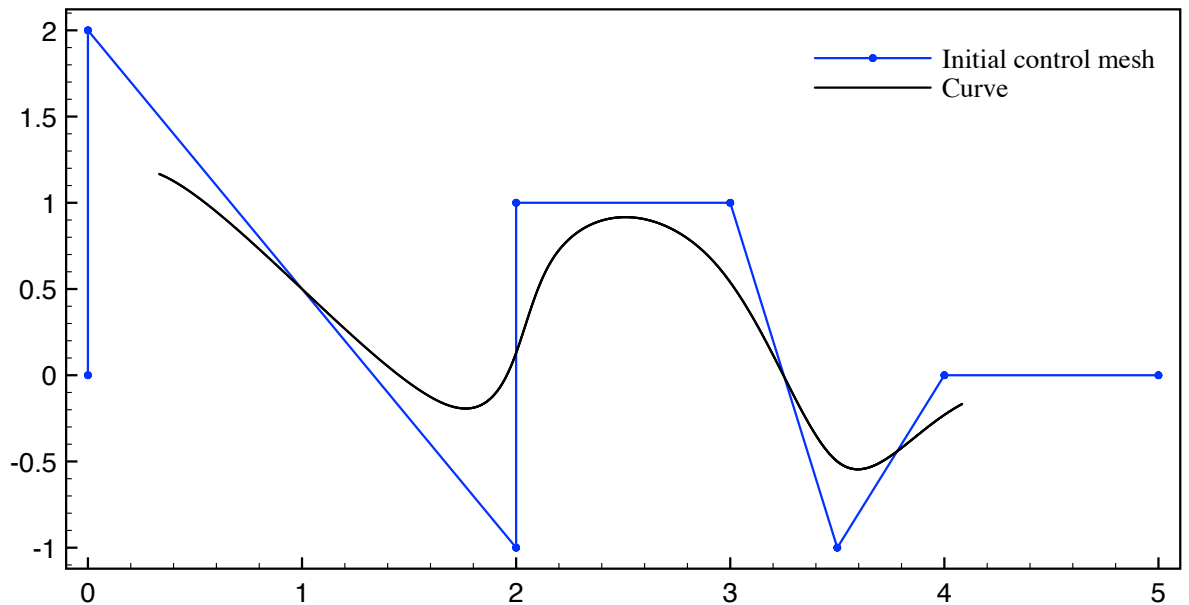
Point \mathbf{P}_{2j}^i is the middle point of $\mathbf{P}_j^{i-1}-\mathbf{P}_{j+1}^{i-1}$. It is called "edge point". The control point \mathbf{P}_{2j+1}^i is computed as:

$$\mathbf{P}_{2j+1}^i = \frac{1}{8}\mathbf{P}_j^{i-1} + \frac{3}{4}\mathbf{P}_{j+1}^{i-1} + \frac{1}{8}\mathbf{P}_{j+2}^{i-1}.$$

To compute this point, one needs to connect the middle points of $\mathbf{P}_{2j}^i-\mathbf{P}_{2j+1}^i$ and $\mathbf{P}_{2j+1}^i-\mathbf{P}_{2j+2}^i$ and the point \mathbf{P}_{2j+1}^i is the middle point of the connecting line. This type of point is called "vertex point". Each "vertex point" is associated with an upper level control point. Figure 3.12a shows two levels of refinements using Catmull-Clark algorithm for constructing a curve and Figure 3.12b shows the limiting result which is a Catmull-Clark curve.



(a) Successive refinements for constructing curve.



(b) A Catmull-Clark Curve with its control polygon.

Figure 3.12: Catmull-Clark Algorithm

Quartic subdivision curves The Chaikin’s algorithm and the Catmull-Clark algorithm are two well-known recursive subdivision schemes which can generate quadratic and cubic B-spline subdivision curves respectively. There are also algorithms for higher order B-spline subdivision

curves. For example, the algorithms for quartic B-spline subdivision curves [97] is given by

$$\begin{cases} \mathbf{P}_{2j}^i = \frac{5}{16}\mathbf{P}_j^{i-1} + \frac{5}{8}\mathbf{P}_{j+1}^{i-1} + \frac{1}{16}\mathbf{P}_{j+2}^{i-1}, \\ \mathbf{P}_{2j+1}^i = \frac{1}{16}\mathbf{P}_j^{i-1} + \frac{5}{8}\mathbf{P}_{j+1}^{i-1} + \frac{5}{16}\mathbf{P}_{j+2}^{i-1}. \end{cases} \quad (3.9)$$

3.2.2 Catmull-Clark subdivision surfaces

With the concept of the bilinear patch, NURBS surfaces are generated as the tensor products of two one-dimensional NURBS. Surfaces can also be generated as the tensor products of two one-dimensional subdivision curves. Subdivision surfaces based on the Chaikin's subdivision algorithm are called Doo-Sabin surfaces [98] (or Chaikin's surfaces). A more well known subdivision surfaces algorithm is the Catmull-Clark subdivision surfaces which can generate bi-cubic B-spline surfaces. To the Catmull-Clark algorithm, one face in the original control mesh is split into four new faces. For a closed surface, the numbers of faces and control points are doubled. Figure 3.13 shows an example of generating new control mesh through the Catmull-Clark algorithm.

Similar with one-dimensional Catmull-Clark curve, the new refined control points can be classified into three types: 'face point', 'edge point' and 'vertex point'. The 'face points' in i^{th} refinement is computed as:

$$\mathbf{P}_{2j,2k}^i = \frac{1}{4}\mathbf{P}_{j,k}^{i-1} + \frac{1}{4}\mathbf{P}_{j,k+1}^{i-1} + \frac{1}{4}\mathbf{P}_{j+1,k}^{i-1} + \frac{1}{4}\mathbf{P}_{j+1,k+1}^{i-1},$$

where j and k are indices of control points for two perpendicular directions. The 'face point' is the central point of the original face. The 'edge point' is computed as

$$\begin{aligned} \mathbf{P}_{2j+1,2k}^i &= \frac{1}{16}\mathbf{P}_{j,k}^{i-1} + \frac{3}{8}\mathbf{P}_{j,k+1}^{i-1} + \frac{1}{16}\mathbf{P}_{j,k+2}^{i-1} \\ &\quad + \frac{1}{16}\mathbf{P}_{j+1,k}^{i-1} + \frac{3}{8}\mathbf{P}_{j+1,k+1}^{i-1} + \frac{1}{16}\mathbf{P}_{j+1,k+2}^{i-1}, \end{aligned}$$

or

$$\begin{aligned} \mathbf{P}_{2j,2k+1}^i &= \frac{1}{16}\mathbf{P}_{j,k}^{i-1} + \frac{1}{16}\mathbf{P}_{j,k+1}^{i-1} + \frac{3}{8}\mathbf{P}_{j+1,k}^{i-1} + \frac{3}{8}\mathbf{P}_{j+1,k+1}^{i-1} \\ &\quad + \frac{1}{16}\mathbf{P}_{j+2,k}^{i-1} + \frac{1}{16}\mathbf{P}_{j+2,k+1}^{i-1}. \end{aligned}$$

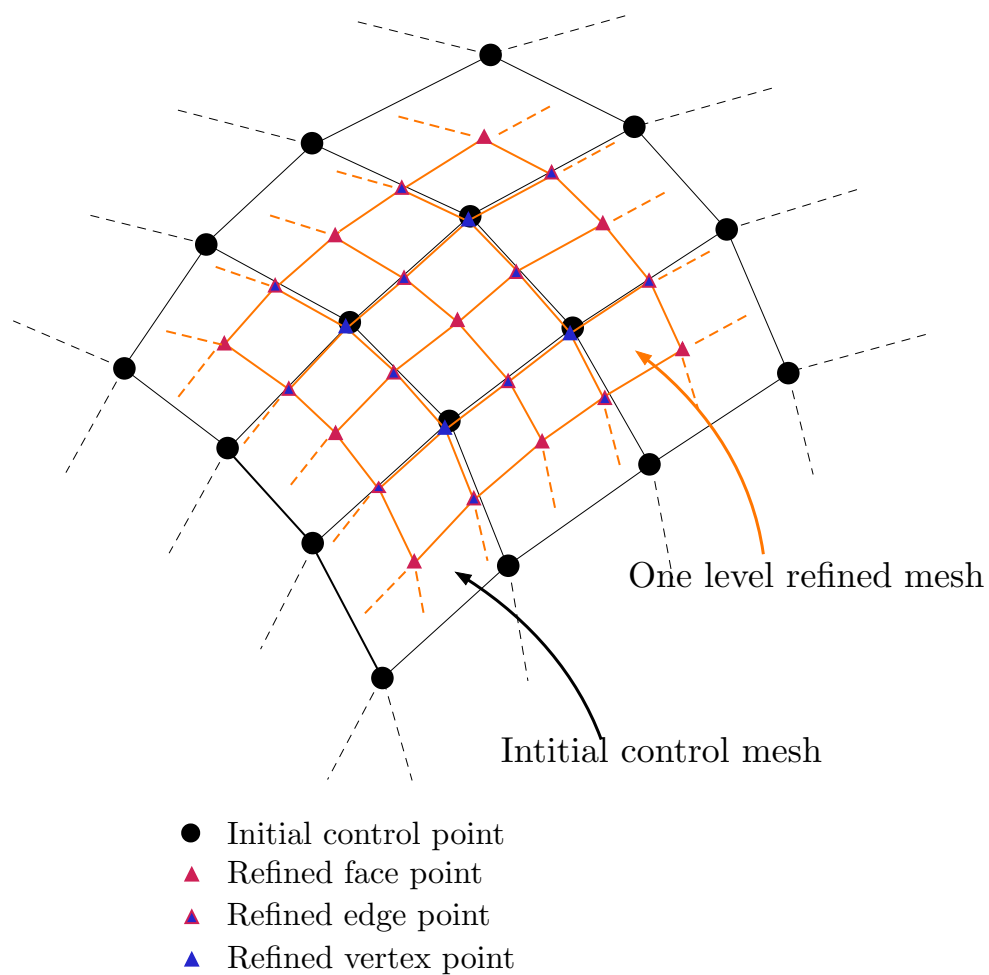


Figure 3.13: Computing refined control mesh through the Catmull-Clark algorithm.

The ‘vertex point’ is computed as

$$\begin{aligned} \mathbf{P}_{2j+1,2k+1}^i &= \frac{1}{64}\mathbf{P}_{j,k}^{i-1} + \frac{3}{32}\mathbf{P}_{j,k+1}^{i-1} + \frac{1}{64}\mathbf{P}_{j,k+2}^{i-1} \\ &\quad + \frac{3}{32}\mathbf{P}_{j+1,k}^{i-1} + \frac{9}{16}\mathbf{P}_{j+1,k+1}^{i-1} + \frac{3}{32}\mathbf{P}_{j+1,k+2}^{i-1} \\ &\quad + \frac{1}{64}\mathbf{P}_{j+2,k}^{i-1} + \frac{3}{32}\mathbf{P}_{j+2,k+1}^{i-1} + \frac{1}{64}\mathbf{P}_{j+2,k+2}^{i-1}. \end{aligned}$$

With these formulas, the new control mesh in the i^{th} level of refinement can be computed using the matrix operator:

$$\mathbf{P}^i = \mathbf{S}\mathbf{P}^{i-1},$$

where \mathbf{P}_i refers the set of control points in i^{th} level of refinement and \mathbf{S} is a subdivision operator which is a matrix consisting of a set of weights. Each weight associates with a control point in \mathbf{P}^{i-1} . The weight distributions for different types of control points are shown in Figure 3.14. After a successive levels of refinements, a smooth B-spline surfaces can be obtained. Figure 3.15 shows a smooth spherical surface generated through levels of refinement starting with a cubic control mesh.

Extraordinary points As mentioned, the Catmull-Clark subdivision surface is similar in nature to NURBS surface as both of them are the tensor products of two one-dimensional curves. As a result, each vertex point in subdivision surface control mesh is connected with only four faces. We define the number of faces connected with the point as the ‘valence’ of the vertex. A regular vertex in a Catmull-Clark surface mesh has a valence of 4. However, contrary to NURBS surfaces, Catmull-Clark subdivision surface can handle irregular cases where the valence of vertex is not equal to 4. Thus allows it to handle arbitrary topologies. In the seminal paper on Catmull-Clark surfaces [96], they proposed a way to modify the weight distributions for a vertex with a valence not equal to 4 in order to achieve complex geometries. Those irregular points are called extraordinary points. Figure 3.16 shows the weight distributions for computing an extraordinary point. With this easy solution, Catmull-Clark surfaces can use a single mesh to present surfaces of arbitrary geometries while other spline-based CAD tools, such as NURBS surface, need to link up multiple patches. Peters and Reif [99] have proven that the limiting

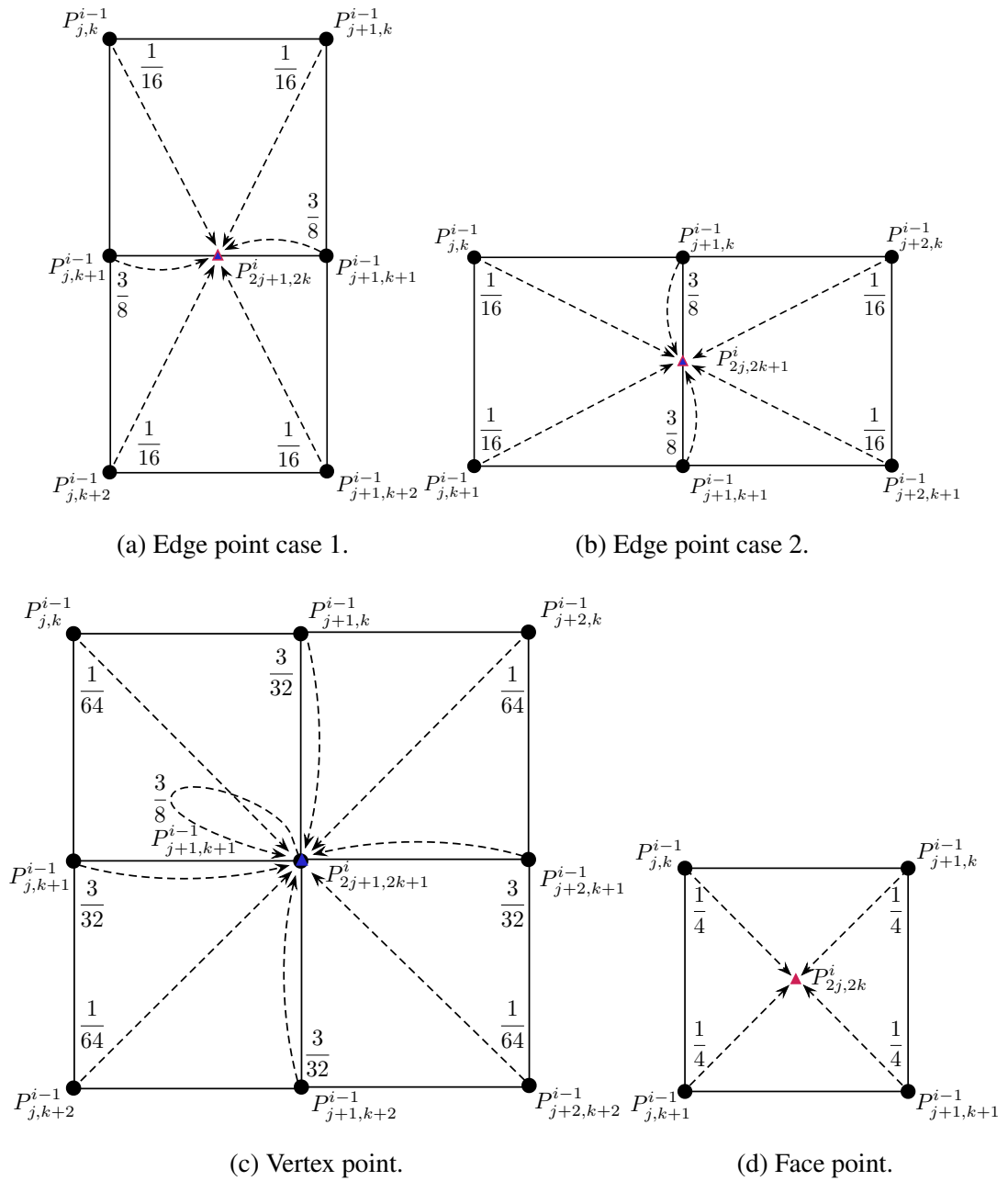


Figure 3.14: The weight distribution for computing different types of new control points.

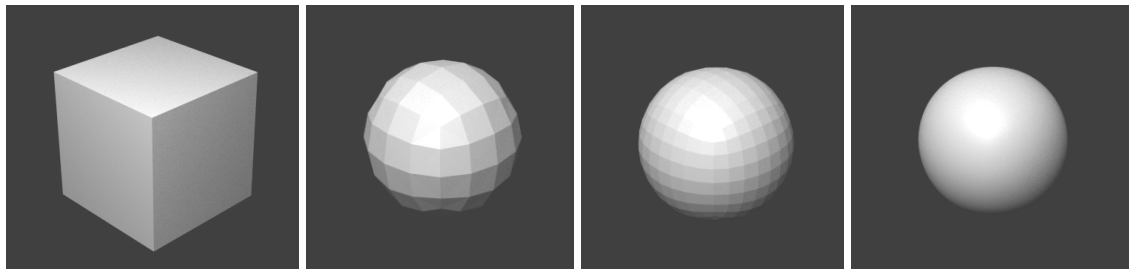


Figure 3.15: Catmull-Clark subdivision algorithm applied to an initial cube control mesh.

surface of Catmull-Clark subdivision algorithm has C^2 continuity all over the surface except at the extraordinary vertices. But the corresponding surface locations of the extraordinary vertices retain C^1 continuity.

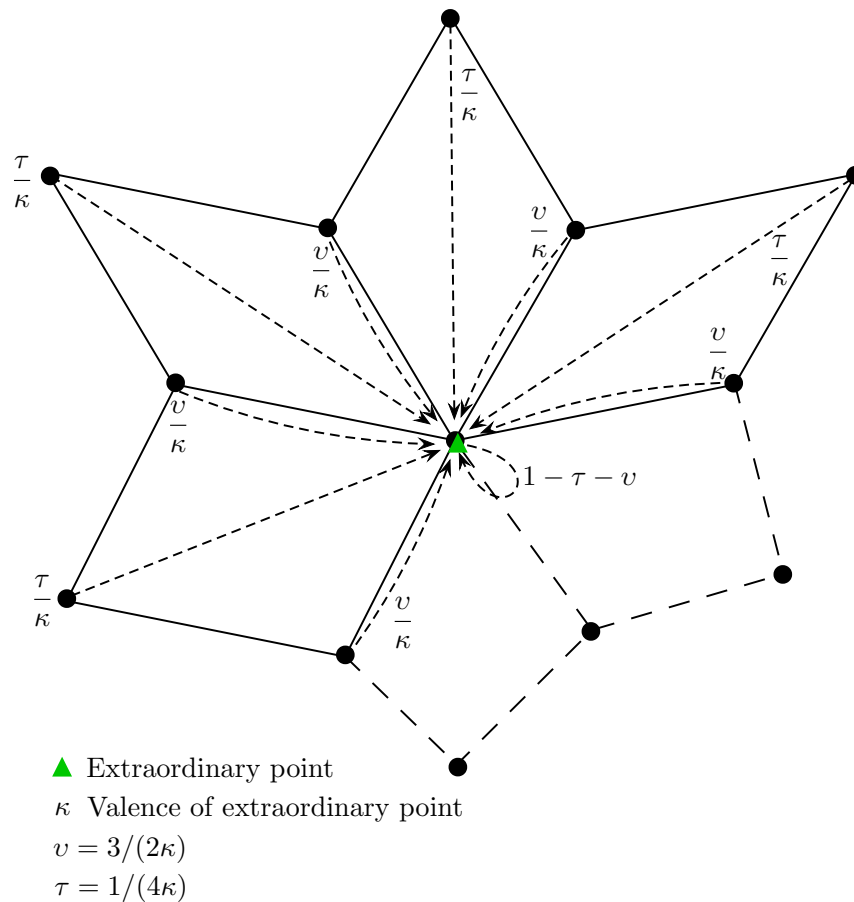


Figure 3.16: Weight distributions for computing an extraordinary point with valence κ .

3.2.3 Loop subdivision surfaces

In the 1990s, Catmull-Clark subdivision surfaces based on quadrilateral elements became the most widely-used geometry representation method in the animation and gaming industries. However, a triangular mesh has advantages in modelling arbitrary geometries with complex topologies. In 1987, Loop presented an approximating subdivision scheme in his Master's thesis [33] which can generate smooth surfaces with triangular control meshes. Similar with the Catmull-Clark subdivision scheme, the smooth surface is defined as the limit of an infinite number of subdivisions of the initial polygon control mesh. In each subdivision, all the elements are quadrisedected into four new sub-elements and new points are computed at the middle points

of all edges. Then, the new edge points and the original vertex points are adjusted by a weight which smooths the original mesh. Figure 3.17 shows the refinement of a triangular mesh using the Loop subdivision scheme. For a vertex point with a valence of κ , the new edge points can be computed as:

$$\mathbf{P}_j^{i+1} = \begin{cases} \frac{3}{8} [\mathbf{P}_0^i + \mathbf{P}_j^i] + \frac{1}{8} [\mathbf{P}_\kappa^i + \mathbf{P}_{j+1}^i], & j = 1, \\ \frac{3}{8} [\mathbf{P}_0^i + \mathbf{P}_j^i] + \frac{1}{8} [\mathbf{P}_{j-1}^i + \mathbf{P}_{j+1}^i], & j = 2, 3, \dots, \kappa - 1, \\ \frac{3}{8} [\mathbf{P}_0^i + \mathbf{P}_j^i] + \frac{1}{8} [\mathbf{P}_{j-1}^i + \mathbf{P}_1^i], & j = \kappa. \end{cases}$$

Because of the quadrisecting scheme, every new refined edge point will be a vertex with a valence 6 in the refined mesh. The old vertex point is relocated with a weight w as:

$$\mathbf{P}_0^{i+1} = [1 - \kappa w] \mathbf{P}_0^i + w \sum_{j=1}^{\kappa} \mathbf{P}_j^i. \quad (3.10)$$

The new vertex point will remain the same valence as the original vertex has. In Loop's thesis, the w_0 is given as:

$$w = \frac{1}{\kappa} \left[\frac{5}{8} - \left[\frac{3}{8} + \frac{1}{4} \cos \frac{2\pi}{\kappa} \right]^2 \right].$$

But it was proven that a simpler choice proposed by Warren [100] can also define smooth surfaces:

$$w = \begin{cases} \frac{3}{8\kappa} & \text{for } \kappa > 3, \\ \frac{3}{16} & \text{for } \kappa = 3. \end{cases}$$

Extraordinary points In a Loop subdivision control mesh, the regular vertex has a valence equal to 6. A vertex whose valence not equal to 6 is called an extraordinary point. Equation 3.10 is a general function which defines the refinement rules of computing new extraordinary vertex points. Evaluating points in an element with extraordinary point is possible, details are given in Section 3.2.4. Similar to Catmull-Clark subdivision surfaces, the Loop subdivision surfaces have C^2 continuity every except the extraordinary points. The corresponding surface locations of the extraordinary vertices have C^1 continuity.

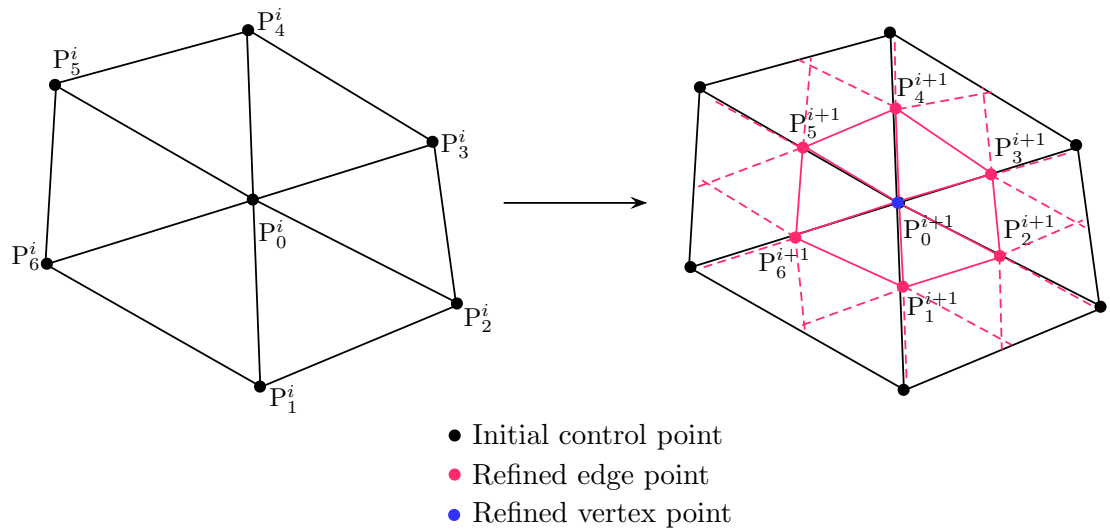


Figure 3.17: Computing refined control mesh through the Loop subdivision algorithm for a regular vertex.

3.2.4 Evaluation of Loop subdivision surfaces

Without the extraordinary points in the mesh, the limiting surface of a Loop subdivision surface can be evaluated from a number of triangular Bézier element patches. The basis functions are derived from box splines. Furthermore, Stam [101] developed a method to evaluate the extraordinary points on Loop subdivision surfaces. This section will first introduce the evaluation method for elements with no extraordinary points in Loop subdivision surfaces. Then the method for evaluating elements with extraordinary will be discussed.

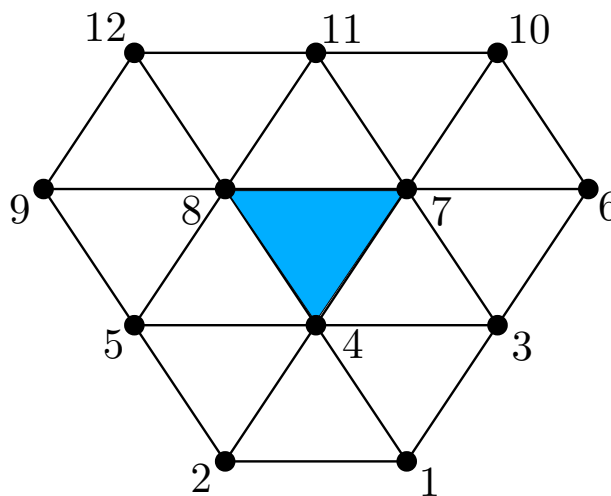


Figure 3.18: A regular patch for an element in Loop subdivision surfaces.

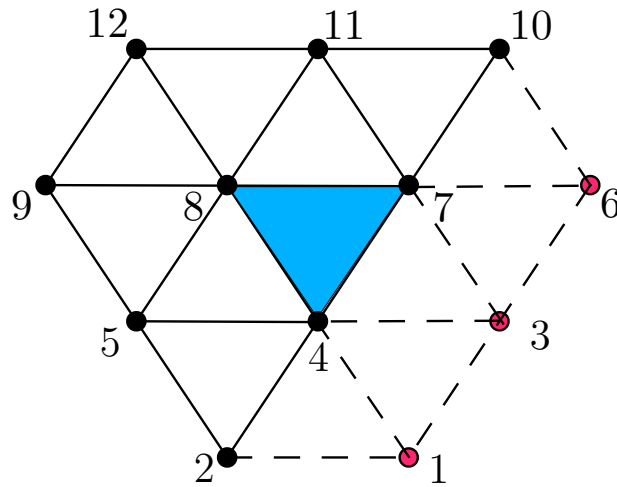


Figure 3.19: A regular patch with ghost points for an element in Loop subdivision surfaces.

Regular patch An element with no extraordinary point (all vertices have valences equal to 6) can form a regular patch with 12 control points as shown in Figure 3.18. If one of the edges of the element is on the boundary, e.g. Edge 4-7 in Figure 3.19 is on the boundary, The points 5, 8 and 11 should be mirrored to 1, 3 and 6. The three points are named ghost points. Using the method proposed by Lai [102], the physical coordinates \mathbf{S} of a point in the triangular Bézier element can be interpolated with box spline functions by

$$\mathbf{S} = \sum_{i=1}^{12} N(u, v, w)_i \mathbf{P}_i,$$

where $N_i(u, v, w)$ is the i^{th} box spline function and \mathbf{P}_i is the coordinates of the i^{th} control point. The box spline function $N(u, v, w)_i$ is calculated with a barycentric coordinates (u, v, w) . The coordinates system is shown in Figure 3.20. Vertex 4 has a coordinates $(1, 0, 0)$, vertex 7 has a coordinates $(0, 1, 0)$ and vertex 8 has a coordinates $(0, 0, 1)$.

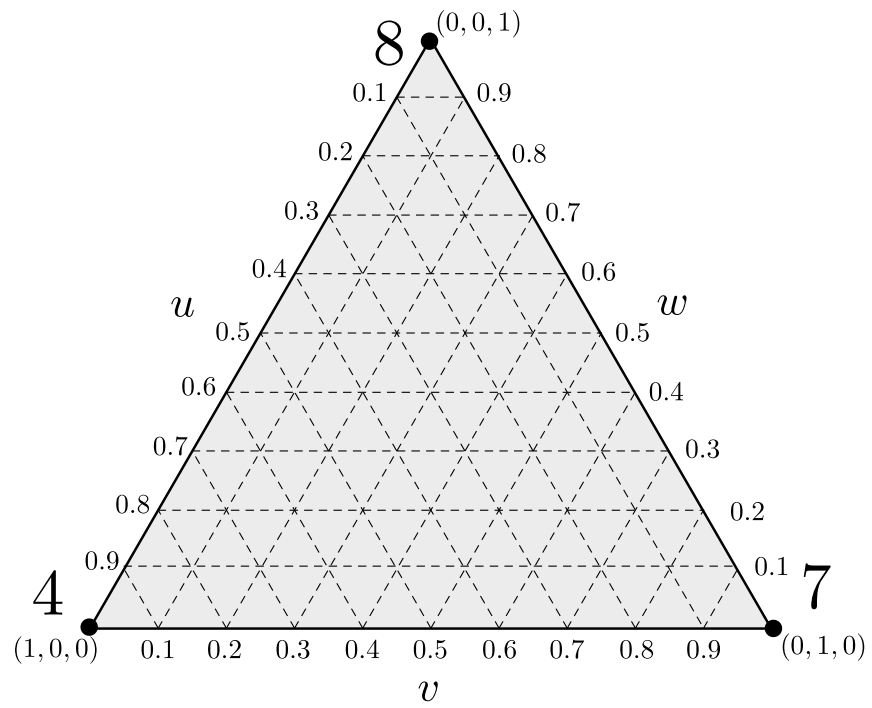


Figure 3.20: Barycentric coordinate of a triangular element.

The set of basis functions $\{N_i(u, v, w)\}_{i=1}^{12}$ are specified as

$$\begin{aligned}
N_1 &= \frac{1}{12}(u^4 + 2u^3v) \\
N_2 &= \frac{1}{12}(u^4 + 2u^3w) \\
N_3 &= \frac{1}{12}(u^4 + 2u^3w + 6u^3v + 6u^2vw + 12u^2v^2 + 6uv^2w + 6uv^3 + 2v^3w + v^4) \\
N_4 &= \frac{1}{12}(6u^4 + 24u^3w + 24u^2w^2 + 8uw^3 + w^4 + 24u^3v + 60u^2vw + 36uvw^2 \\
&\quad + 6vw^3 + 24u^2v^2 + 36uv^2w + 12v^2w^2 + 8uv^3 + 6v^3w + v^4) \\
N_5 &= \frac{1}{12}(u^4 + 6u^3w + 12u^2w^2 + 6uw^3 + w^4 + 2u^3v + 6u^2vw + 6uvw^2 + 2vw^3) \\
N_6 &= \frac{1}{12}(2uw^3 + v^4) \\
N_7 &= \frac{1}{12}(u^4 + 6u^3w + 12u^2w^2 + 6uw^3 + w^4 + 8u^3v + 36u^2vw + 36uvw^2 + 8vw^3 \\
&\quad + 24u^2v^2 + 60uv^2w + 24v^2w^2 + 24uv^3 + 24v^3w + 6v^4) \\
N_8 &= \frac{1}{12}(u^4 + 8u^3w + 24u^2w^2 + 24uw^3 + 6w^4 + 6u^3v + 36u^2vw + 60uvw^2 + 24vw^3 \\
&\quad + 12u^2v^2 + 36uv^2w + 24v^2w^2 + 6uv^3 + 8v^3w + v^4) \\
N_9 &= \frac{1}{12}(2uw^3 + w^4) \\
N_{10} &= \frac{1}{12}(2v^3w + v^4) \\
N_{11} &= \frac{1}{12}(2uw^3 + w^4 + 6uvw^2 + 6vw^3 + 6uv^2w + 12v^2w^2 + 2uv^3 + 6v^3w + v^4) \\
N_{12} &= \frac{1}{12}(2vw^3 + w^4).
\end{aligned} \tag{3.11}$$

The set of basis function is denoted in vector form by \mathbf{N} .

Irregular patch If an element has an extraordinary vertex, the corresponding element patch is called an irregular patch as shown in Figure 3.21. Vertex 1 is an extraordinary vertex with a valence $\kappa \neq 6$. The total number of control vertices in this element patch equals $\kappa + 6$, numbered as shown in the figure. To evaluate the shaded triangular element, a subdivision scheme should be applied on the three vertices of the element to divide the element into four sub-elements as Figure 3.22 and a new element patch with control vertices as shown in Figure 3.23 is formed from the original element. The new sub-elements 1, 2 and 3 do not have any extraordinary

vertices. The new patches for these three new sub-elements are regular and the surface points can be evaluated using box-spline functions and the new control vertices. However, the new sub-element 4 still has an extraordinary vertex. If the target point is in this element, we must repeatedly refine the element until the target point fall into a new sub-element without an extraordinary vertex. This method can only handle the case that the element has only one extraordinary vertex.

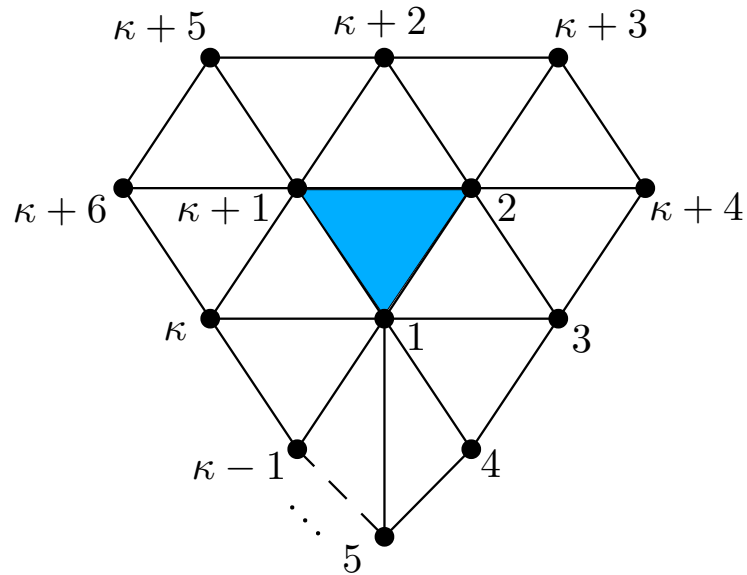


Figure 3.21: An irregular patch for an element in Loop subdivision surfaces.

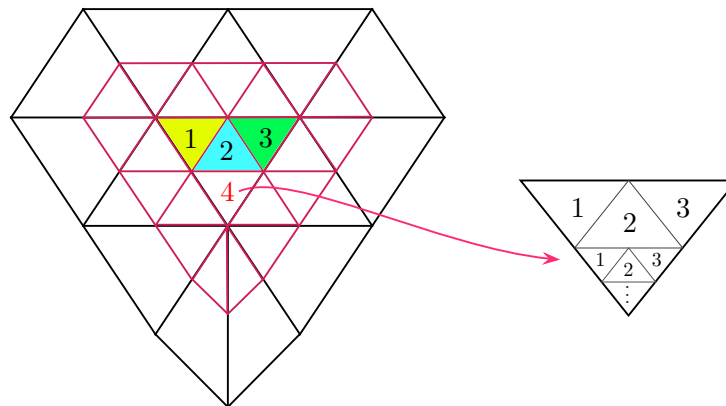


Figure 3.22: Refinement of an element with one extraordinary vertex.

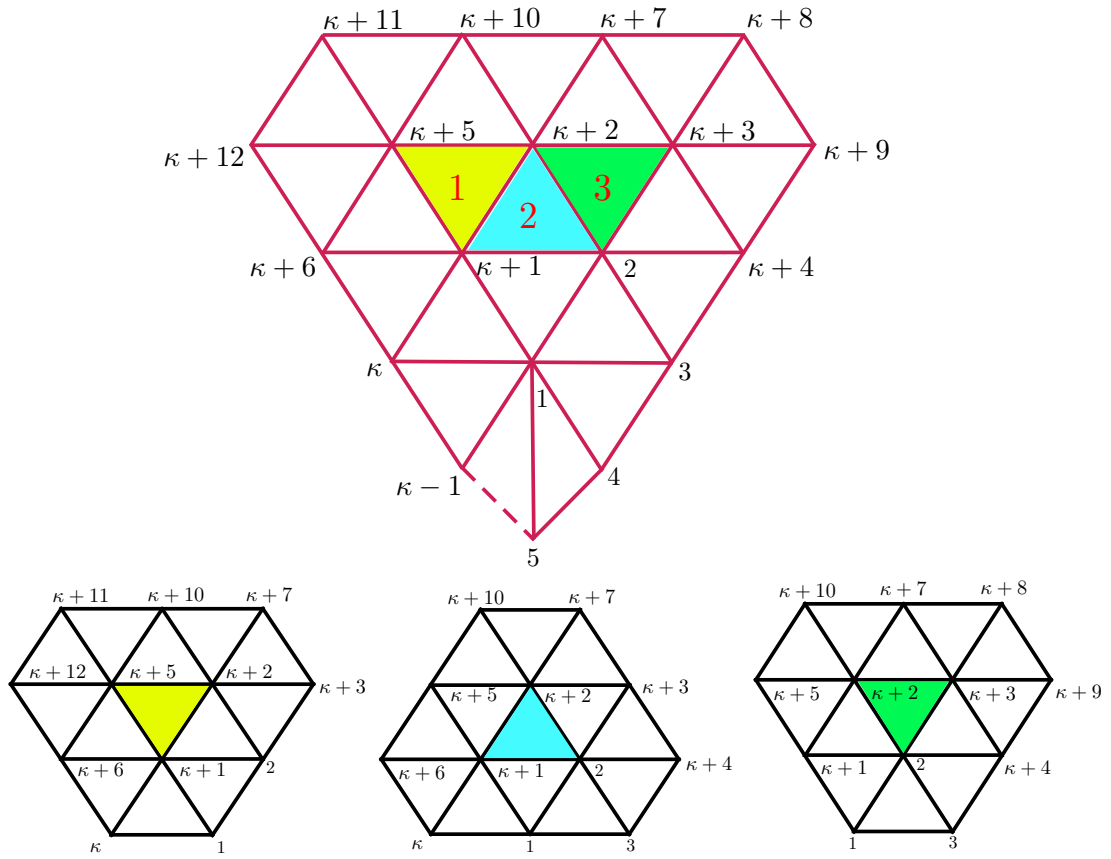


Figure 3.23: Refined element patch and sub-patches for the sub-element 1, 2 and 3.

We denote the control points of an irregular patch in Figure 3.21 as a matrix form \mathbf{P} and the initial control points of the patch is expressed as

$$\mathbf{P}_0 = [\mathbf{P}_{0,1}, \mathbf{P}_{0,2}, \dots, \mathbf{P}_{0,\kappa+6}]^T.$$

Through one level of subdivision we generate new $\kappa + 6$ control points as shown in Figure 3.22, denote by

$$\mathbf{P}_1 = [\mathbf{P}_{1,1}, \mathbf{P}_{1,2}, \dots, \mathbf{P}_{1,\kappa+12}]^T.$$

The subdivision step is represented as

$$\mathbf{P}_1 = \mathbf{A}\mathbf{P}_0,$$

where

$$\mathbf{A} = \begin{bmatrix} \mathbf{S} & \mathbf{0} \\ \mathbf{S}_{11} & \mathbf{S}_{12} \\ \mathbf{S}_{21} & \mathbf{S}_{22} \end{bmatrix}.$$

The term \mathbf{S} , \mathbf{S}_{11} , \mathbf{S}_{12} , \mathbf{S}_{21} and \mathbf{S}_{22} are defined in [101]. To evaluate the sub-element 1, 2 and 3 in Figure 3.23, only requires $\kappa + 6$ new control points out of the new $\kappa + 12$ control point patch. A selection matrix \mathbf{D} for sub-element $k = 1, 2, 3$ is using to select the necessary control points from \mathbf{P}_1 :

$$\mathbf{P}_{1,k} = \mathbf{D}_k \mathbf{P}_1.$$

Then the surface point can be evaluate with the box-spline basis functions as

$$\mathbf{S} = \mathbf{P}_{1,k}^T \mathbf{N}.$$

Element 4 in Figure 3.22 can not yet be evaluated because it still has an extraordinary vertex. Through successive refinements, as shown in Figure 3.22, the non-evaluable region can be limited into a negligible area. Using this method, the extraordinary vertex can be evaluated with a very small offset. However, the extraordinary vertex only has a C^1 continuity.

Assume the surface point \mathbf{S} has a parametric coordinates (u, v, w) , where $u = 1 - v - w$, one first determines the number of refinements required to evaluate this surface point. If u of the surface point requires n refinement to satisfies the criterion:

$$\left[\frac{1}{2}\right]^{n+1} < u \leq \left[\frac{1}{2}\right]^n,$$

the surface point can be evaluated. After each refinement, the element is partitioned into four elements and three of them are evaluable. One denotes the evaluable sub-elements as Δ_k^j , where sub-element Δ_k^j is generated after the j^{th} refinement and k is the sub-element index ($k = 1, 2, 3$). The successive refinement procedure is shown in Figure 3.24. After determining

the number of refinements n, k should also be determined as

$$k = \begin{cases} 1 & \text{if } \left[\frac{1}{2}\right]^{n+1} < v \leq \left[\frac{1}{2}\right]^n, \\ 2 & \text{if } v \leq \left[\frac{1}{2}\right]^{n+1} \quad \text{and} \quad w \leq \left[\frac{1}{2}\right]^{n+1}, \\ 3 & \text{if } \left[\frac{1}{2}\right]^{n+1} < w \leq \left[\frac{1}{2}\right]^n. \end{cases}$$

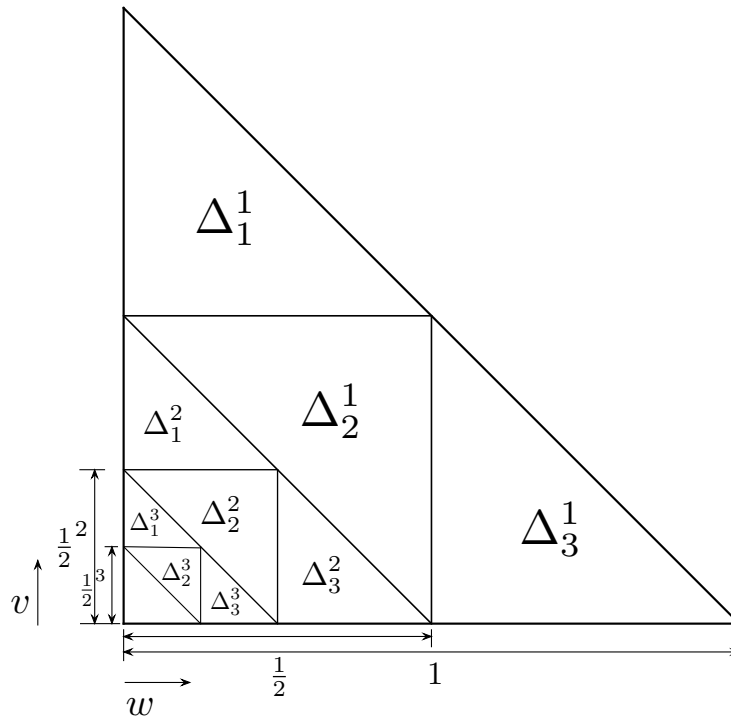


Figure 3.24: Successive refinements of the parametric domain for evaluating an irregular element.

Now, the surface point S is located in the regular sub-element k after n th refinement. The patch for this element is picked with the selection matrix \mathbf{D}_k as follows.

$$\mathbf{P}_{n,k} = \mathbf{D}_k \mathbf{P}_n.$$

The enlarged matrix \mathbf{P}_n contains $\kappa + 12$ control vertices, which is generated from the subdivision of $\bar{\mathbf{P}}_{n-1}$:

$$\mathbf{P}_n = \mathbf{A} \bar{\mathbf{P}}_{n-1}.$$

The patch $\bar{\mathbf{P}}_{n-1}$ has $\kappa + 6$ control vertices. It is successively refined from the initial patch \mathbf{P}_0 as follows.

$$\bar{\mathbf{P}}_{n-1} = \bar{\mathbf{A}}^{n-1} \mathbf{P}_0,$$

where $\bar{\mathbf{A}}$ is a square matrix which subdivides the patch for computing the new patch for the irregular element, and is defined by

$$\bar{\mathbf{A}} = \begin{bmatrix} \mathbf{S} & \mathbf{0} \\ \mathbf{S}_{11} & \mathbf{S}_{12} \end{bmatrix}.$$

Then the patch for new sub-element $\mathbf{P}_{n,k}$ is expressed as

$$\mathbf{P}_{n,k} = \mathbf{D}_k \mathbf{A} \bar{\mathbf{A}}^{n-1} \mathbf{P}_0.$$

The surface point in the element with an extraordinary vertex can be computed as

$$\mathbf{S} = \mathbf{P}_{n,k}^T \mathbf{N} = \mathbf{P}_0^T \underbrace{[\mathbf{D}_k \mathbf{A} \bar{\mathbf{A}}^{n-1}]^T}_{\mathbf{N}_L} \mathbf{N}, \quad (3.12)$$

where \mathbf{N}_L is the Loop subdivision surfaces basis function.

3.2.5 Comparison of subdivision with NURBS surfaces

NURBS and subdivision surfaces both have their strengths and weaknesses in geometric modelling and analysis. The traditional method uses polygons to represent geometries piecewise. They require a large amount of memory to store the information associated with points. NURBS is an efficient technique which can model precise geometries with smooth surfaces using only few control points since the surface is interpolated mathematically. But one NURBS patch can only represent simple geometries due to its tensor product nature. Subdivision surfaces combine the advantages of polygons and NURBS. It can generate smooth surfaces with flexible coarse polygon meshes.

In terms of analysis, Because NURBS can model exact geometries, It performs better in

idealised benchmark problems such as the sphere examples in Section 4.5.1 and Section 5.3.1. There is no geometric error involved in the entire analysis. So, we note that the NURBS surfaces and subdivision surfaces will not be compared using such numerical examples. Furthermore, NURBS curve can be easily p -refined but a specific subdivision algorithm can only provide a certain polynomial degree. However, subdivision surfaces have their own advantages in analysis. NURBS uses B-splines which are recursive functions. They are more expensive to compute during analysis while the basis functions used in subdivision surfaces are computed as polynomials. The Bézier extraction process converts the NURBS surfaces into Bézier elements but also loose the high continuity across elements. However subdivision surfaces have C^1 continuities everywhere. We also note that subdivision surfaces are not ideal for problems involving discontinuities such as cracks and fractures.

Chapter 4

Boundary element method for acoustics

The dominant numerical methods used in engineering include the finite element method, the finite difference method and the boundary element method. Each of these approaches convert continuous formulations into a discrete setting for amenable computer implementation. In the case of the finite difference method and finite element method, a partial differential equation is used as the starting point to formulate the system equations. However, in the case of boundary element method, the governing partial differential equation must first be converted into an integral equation. A fundamental requirement of the boundary element method is that a Green's function is defined to allow the integral equation to be formulated. Because the integral equations are built only on the boundary, the method can only be applied to problems where the governing differential equations are linear equations.

The history of using integral equations to formulate the fundamental boundary value problems can dates back to 1903. Fredholm [103] used a discretisation procedure to calculate the solutions with integral equations. However, the early development of this method was restricted by the large demands of calculations. With the development of computer technology, discretisation procedures were implemented for integral equations in the 1950s. The first application of integral equations using computers is Massonnet [104], where elasticity problems were solved. In the early 1960s, the applications of discretisation procedures were used to solve boundary integral equations in different engineering fields with some famous contributions by Jaswon [105] and Symm [106].

Lachat and Watson [107] introduced a formulation to discretise the boundary integral equations using isoparametric elements. They stated the advantages of using quadratic isoparametric elements and illustrated a way to evaluate the singular integrals. The term boundary element method was first proposed in the literature by Brebbia [108] in 1978 which is the first book on the BEM. The weighted residual approach for deriving boundary integral equations was used for the first time in Brebbia's book. Further applications of the BEM have included fracture [109–111], potential problems [112], elasticity [113–115], acoustics [17, 114] and electromagnetics [116].

Acoustic analysis is almost needed in all the aspects of modern engineering designs involving the noise control. The computational acoustic analysis contributes to the development of many manufacturing industries including aeronautics and astronautics, electronic and electrical equipments, ship, automotive and building industries. Moreover, numerical simulations of acoustics are also widely applied in the built environment, biomedical and marine sciences. The modelling of exterior acoustic radiation and scattering problems have unbounded (infinite) fluid domains. The finite element method and finite difference method must create arbitrary bounds of the domain and apply special boundary conditions to simulate the acoustic phenomenon, which sometimes can be very complex in terms of implementation [117, 118]. The boundary element method solve the integral equation built only on the boundaries which have advantages in handling these kind of problems. Therefore, the boundary element method is the ideal computational method to simulate acoustic behaviour. Section 4.1 will introduce the fundamentals of acoustics and illustrate the Helmholtz equation – the governing equation of linear acoustic problems. The Green's function of the Helmholtz equation is also solved in this section. In Section 4.2, a boundary integral equation is formulated with the Helmholtz Green's function for solving the acoustic scattering problem. Then, a subdivision surfaces IGA discretisation is applied to the boundary integral equation and a collocation boundary element method is illustrated. Section 4.4 introduces different methods to deal with the singular integrals in the boundary element method.

4.1 Fundamentals of linear acoustic analysis

In engineering, acoustics is considered as a study of mechanical waves propagation in fluids which cause pressure fluctuations. The acoustic waves are longitudinal waves which vibrate in the same direction as they travel. Thus acoustic waves are relatively simple waves which do not have any polarisation, but similar to other kinds of waves, acoustic waves can diffract, reflect and interfere with each other. It is a very complex phenomenon when the acoustic wave is scattered by one or multiple objects. This section first introduces two important acoustic properties – acoustic pressure and acoustic velocity. Then, it illustrates why the Helmholtz equation is the governing equation for linear acoustic problems. Then, the fundamental solution of the Helmholtz equation is derived, which is essential for the implementation of the acoustic boundary element method.

4.1.1 Acoustic pressure and acoustic velocity

The two important parameters of a acoustic wave are acoustic pressure and acoustic velocity. The acoustic pressure describes the local pressure deviation in the propagating medium caused by the acoustic wave. The acoustic velocity \mathbf{v} , also termed as particle velocity, indicates the speed of sound propagating in the medium. It is defined by

$$\mathbf{v} = \frac{\partial \mathbf{u}}{\partial t},$$

where t is the time and \mathbf{u} is the particle displacement. The linear wave equation is the fundamental equation which describes the sound propagation in terms of either p or \mathbf{u} . For the acoustic pressure p , the equation is expressed as

$$\nabla^2 p - \frac{1}{c^2} \frac{\partial^2 p}{\partial t^2} = 0, \quad (4.1)$$

where ∇^2 is the Laplace operator, c is the thermodynamic speed of sound which depends on the property of the propagating medium. A similar formulation is also valid for acoustic velocity

magnitude \bar{v} , given as

$$\nabla^2 \bar{v} - \frac{1}{c^2} \frac{\partial^2 \bar{v}}{\partial t^2} = 0.$$

4.1.2 Helmholtz equation

For a harmonic time-dependent acoustic wave, the acoustic pressure $\tilde{p}(\mathbf{x}, t)$ can be expressed as

$$\tilde{p}(\mathbf{x}, t) = p(\mathbf{x})e^{-i\omega t},$$

where $p(\mathbf{x})$ is the amplitude of the acoustic pressure at point \mathbf{x} , ω is the angular frequency and i is the imaginary unit defined as $i := \sqrt{-1}$. Substituting the expression of acoustic pressure into the linear wave equation (4.1) yields

$$\nabla^2 p(\mathbf{x})e^{-i\omega t} - p(\mathbf{x})\frac{1}{c^2}\frac{\partial^2(e^{-i\omega t})}{\partial t^2} = 0.$$

This can be simplified as

$$\nabla^2 p(\mathbf{x})e^{-i\omega t} + \frac{\omega^2}{c^2}p(\mathbf{x})e^{-i\omega t} = 0,$$

where $\omega/c = \bar{k}$ can be replaced by the wave number, which is the spatial frequency of the wave.

After eliminating the term $e^{-i\omega t}$, the equation reduces to the Helmholtz equation given by

$$\nabla^2 p(\mathbf{x}) + \bar{k}^2 p(\mathbf{x}) = 0. \quad (4.2)$$

Here, $p(\mathbf{x})$ satisfies the expression of the Helmholtz equation, so that the time harmonic linear acoustic wave problem can be governed by the Helmholtz equation.

4.1.3 Helmholtz fundamental solution

In the previous section, the Helmholtz equation is showed which is the governing equation for time harmonic linear acoustic problem. In order to solve this equation with boundary element method, the fundamental solution of the Helmholtz equation is required. The fundamental solution of Helmholtz equation G is a function of the field point \mathbf{y} and source point \mathbf{x} which

is denoted as $G(\mathbf{x}, \mathbf{y})$ and it is also known as Green's function. The Green's function satisfies the differential equation

$$\nabla^2 G(\mathbf{x}, \mathbf{y}) + \bar{k}^2 G(\mathbf{x}, \mathbf{y}) = -\delta(\mathbf{x}, \mathbf{y}), \quad (4.3)$$

where δ denotes the Dirac delta function. In \mathbb{R}^1 , it can be defined as:

$$\delta(x', x) = \lim_{N \rightarrow \infty} \frac{\sin[N(x - x')]}{\pi(x - x')}.$$

It is also known as the unit impulse symbol and has the property:

$$\int_{-\infty}^{\infty} \delta(x', x) dx = \int_{x' - \bar{h}}^{x' + \bar{h}} \delta(x', x) dx = 1,$$

where \bar{h} is any positive number. A simple definition in \mathbb{R}^3 is given as

$$\delta(\mathbf{x}, \mathbf{y}) = \begin{cases} \infty & \text{if } \mathbf{x} = \mathbf{y}, \\ 0 & \text{otherwise.} \end{cases}$$

When the field point and source point are not identical, the Green's function satisfied the Helmholtz equation:

$$\nabla^2 G(\mathbf{x}, \mathbf{y}) + \bar{k}^2 G(\mathbf{x}, \mathbf{y}) = 0, \text{ for } \mathbf{x} \neq \mathbf{y}. \quad (4.4)$$

To solve the Green's function, one constructs a spherical coordinate system centred at source point \mathbf{x} and the field point \mathbf{y} has coordinates (r, θ_1, θ_2) , where $r := |\mathbf{x} - \mathbf{y}|$ and θ_1 and θ_2 are two angular coordinates. Then, the Equation 4.4 is reformulated as

$$\frac{1}{r^2} \frac{d}{dr} \left[r^2 \frac{dG}{dr} \right] + \bar{k}^2 G = 0, \text{ for } r \neq 0,$$

which can be written in the form of an ordinary differential equation in terms of r as

$$G'' + \frac{2}{r} G' + \bar{k}^2 G = 0, \text{ for } r \neq 0.$$

The general solution for this ordinary differential equation is given by

$$G = A \frac{e^{i\bar{k}r}}{r} + B \frac{e^{-i\bar{k}r}}{r}, \quad (4.5)$$

where A and B are unknown constant coefficients which need to be determined. The two terms on the right-hand side represent two waves propagating in two opposite directions. Let $B = 0$ to just consider one of them. Assume the source point \mathbf{x} is surrounded by a small sphere with a infinitesimal radius ϵ and the point \mathbf{y} is on the surface of the small sphere, the left-hand side of Equation 4.3 has the property of the Dirac delta function expressed as

$$\int_{V_\epsilon} [\nabla^2 G(\mathbf{x}, \mathbf{y}) + \bar{k}^2 G(\mathbf{x}, \mathbf{y})] dV_\epsilon = -1.$$

Because the radius is infinitesimal, the Helmholtz equation is yielding to the Laplace equation and

$$\int_{V_\epsilon} \nabla^2 G(\mathbf{x}, \mathbf{y}) dV_\epsilon = -1.$$

Apply the divergence theorem:

$$\int_{V_\epsilon} \nabla^2 G(\mathbf{x}, \mathbf{y}) dV_\epsilon = \int_{\Gamma_\epsilon} \frac{\partial G(\mathbf{x}, \mathbf{y})}{\partial n} d\Gamma_\epsilon = -1. \quad (4.6)$$

The Green's function is now a static function, $G = \bar{G} = a/r$, where $r = |\mathbf{x} - \mathbf{y}| = \epsilon$. The normal direction is the same direction with the radius. $\partial G / \partial n = -a/\epsilon^2$ and the integral becomes:

$$a \frac{1}{\epsilon^2} \int_{\Gamma_\epsilon} d\Gamma_\epsilon = 1, \quad (4.7)$$

where the surface area of the small circle is $4\pi\epsilon^2$, so $a = 1/4\pi$ and the Green's function for Helmholtz equation is thus

$$G(\mathbf{x}, \mathbf{y}) = \frac{e^{i\bar{k}r}}{4\pi r}. \quad (4.8)$$

The normal derivative of the Green's function for Helmholtz equation is:

$$\frac{\partial G(\mathbf{x}, \mathbf{y})}{\partial n} = \frac{e^{i\bar{k}r}}{4\pi r^2} [i\bar{k}r - 1] \frac{\partial r}{\partial n}. \quad (4.9)$$

4.2 Acoustic boundary element method

This section will derive the boundary integral equation starting with the Helmholtz equation. After obtaining the boundary integral equation, different boundary conditions for the acoustic problems will be discussed. The boundary integral equation is discretised with the subdivision surfaces IGA approach and a collocation scheme is used to formulate the boundary element system of equations.

4.2.1 Boundary integral equation for the Helmholtz equation

The acoustic boundary integral equation is to solve the Helmholtz equation (4.2). For a point source of unit strength, the Helmholtz equation is expressed as

$$\nabla^2 p(\mathbf{P}, \mathbf{Q}) + \bar{k}^2 p(\mathbf{P}, \mathbf{Q}) = 0 \text{ when } \mathbf{P} \neq \mathbf{Q},$$

where the \mathbf{P} is the source point and \mathbf{Q} is the field point. The fundamental solution of the Helmholtz equation is $e^{i\bar{k}r}/4\pi r$. Recall r is the absolute value of distance between field point \mathbf{P} to the source point \mathbf{Q} . The solution is denoted as the Green function $G(\mathbf{P}, \mathbf{Q})$. Assume a space region Ω with closed surface Γ with outward unit normal vector \mathbf{n} and a force \mathbf{F} is acting on Ω . The total flux of the force on the surface Γ must be equal to the volume integral of the divergence of \mathbf{F} , which is the divergence theorem expressed as

$$\int_{\Omega} \nabla \cdot \mathbf{F} \, d\Omega = \int_{\Gamma} \mathbf{F} \cdot \mathbf{n} \, d\Gamma. \quad (4.10)$$

Assume two arbitrary functions ψ and ϕ and their first derivatives are continuous in the space domain Ω . Replace \mathbf{F} in Equation 4.10 with $\psi\nabla\phi$ and the Green's first identity shown as

$$\int_{\Omega} [\psi\nabla^2\phi + \nabla\psi \cdot \nabla\phi] d\Omega = \int_{\Gamma} \psi\nabla\phi \cdot \mathbf{n} d\Gamma. \quad (4.11)$$

Interchange ψ and ϕ with each other in Equation 4.11 and the resulting equation is still valid. Then subtract the new equation from Equation 4.11 to give the Green's second identity as

$$\int_{\Omega} [\psi\nabla^2\phi - \phi \cdot \nabla^2\psi] d\Omega = \int_{\Gamma} [\psi\nabla\phi - \phi\nabla\psi] \cdot \mathbf{n} d\Gamma.$$

Then, substitute the fundamental solution of Helmholtz equation G and into the Green's second identity and use the acoustic pressure p to replace ϕ . The Green's second identity becomes

$$\int_{\Omega} [G\nabla^2p - p\nabla^2G] d\Omega = \int_{\Gamma} \left[G \frac{\partial p}{\partial n} - p \frac{\partial G}{\partial n} \right] d\Gamma, \quad (4.12)$$

where p satisfies the Helmholtz equation, $\nabla^2p = -\bar{k}^2p$. Thus

$$\int_{\Omega} (\nabla^2G + \bar{k}^2G) p d\Omega = \int_{\Gamma} \left[p \frac{\partial G}{\partial n} - G \frac{\partial p}{\partial n} \right] d\Gamma. \quad (4.13)$$

Thus fundamental solution Green function G has the property

$$\nabla^2G(\mathbf{P}, \mathbf{Q}) + \bar{k}^2G(\mathbf{P}, \mathbf{Q}) = -\delta(\mathbf{P}, \mathbf{Q}),$$

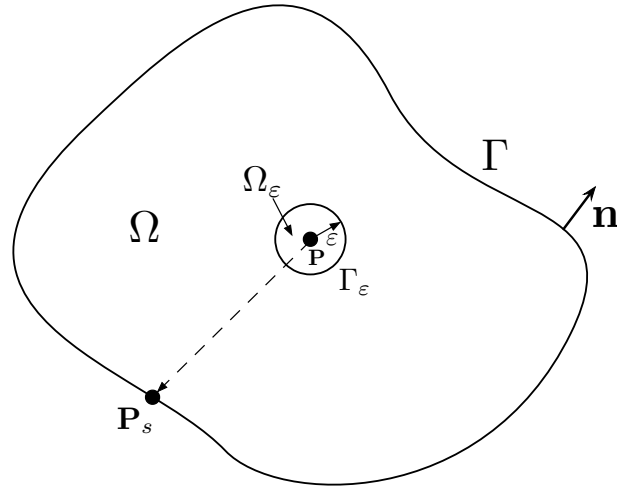


Figure 4.1: The source point is contained by a small sphere with radius ϵ to avoid singularity.

The Dirac delta function is infinite when \mathbf{Q} is identical to \mathbf{P} , which leads to a singular problem in integration. One introduces a circle of radius ϵ centred at source point \mathbf{P} into this domain to avoid the singularity and extend Equation 4.13 as

$$\int_{\Omega \setminus \Omega_\epsilon} [\nabla^2 G + \bar{k}^2 G] p \, d\Omega = \int_\Gamma \left[p \frac{\partial G}{\partial n} - G \frac{\partial p}{\partial n} \right] d\Gamma + \int_{\Gamma_\epsilon} \left[p \frac{\partial G}{\partial n} - G \frac{\partial p}{\partial n} \right] d\Gamma.$$

Taking the limit $\epsilon \rightarrow 0$ and this equation will be identical to Equation 4.13. Due to the property of the Dirac delta function, the left-hand integral over $\Omega \setminus \Omega_\epsilon$ vanishes. And

$$0 = \int_\Gamma \left[p(\mathbf{Q}_s) \frac{\partial G(\mathbf{P}, \mathbf{Q}_s)}{\partial n(\mathbf{Q}_s)} - G(\mathbf{P}, \mathbf{Q}_s) \frac{\partial p}{\partial n}(\mathbf{Q}_s) \right] d\Gamma + \int_{\Gamma_\epsilon} \left[p(\mathbf{Q}_s) \frac{\partial G(\mathbf{P}, \mathbf{Q}_s)}{\partial n(\mathbf{Q}_s)} - G(\mathbf{P}, \mathbf{Q}_s) \frac{\partial p}{\partial n}(\mathbf{Q}_s) \right] d\Gamma, \quad (4.14)$$

where \mathbf{Q}_s denotes the field point on the boundary.

Then, interpreting the part $\int_{\Gamma_\epsilon} p(\mathbf{Q}_s) [\partial G(\mathbf{P}, \mathbf{Q}_s) / \partial n(\mathbf{Q}_s)] d\Gamma$ as a first-order Taylor series expansion of the function $p(\mathbf{Q}_s)$ in terms of $p(\mathbf{P})$. One obtains

$$\int_{\Gamma_\epsilon} p(\mathbf{Q}_s) \frac{\partial G(\mathbf{P}, \mathbf{Q}_s)}{\partial n(\mathbf{Q}_s)} d\Gamma = \int_{\Gamma_\epsilon} [p(\mathbf{Q}_s) - p(\mathbf{P})] \frac{\partial G(\mathbf{P}, \mathbf{Q}_s)}{\partial n(\mathbf{Q}_s)} d\Gamma + p(\mathbf{P}) \int_{\Gamma_\epsilon} \frac{\partial G(\mathbf{P}, \mathbf{Q}_s)}{\partial n(\mathbf{Q}_s)} d\Gamma.$$

When $\epsilon \rightarrow 0$, \mathbf{Q}_s is approaching \mathbf{P} . It is obvious that

$$\lim_{\epsilon \rightarrow 0} \int_{\Gamma_\epsilon} [p(\mathbf{Q}_s) - p(\mathbf{P})] \frac{\partial G(\mathbf{P}, \mathbf{Q}_s)}{\partial n(\mathbf{Q}_s)} d\Gamma = 0.$$

Following the same approach with Equation 4.6, but the direction of the normal vector opposite to the radius vector because the source point is now exclusive of the space domain, one obtains

$$\lim_{\epsilon \rightarrow 0} \int_{\Gamma_\epsilon} \frac{\partial G(\mathbf{P}, \mathbf{Q}_s)}{\partial n(\mathbf{Q}_s)} d\Gamma = 1. \quad (4.15)$$

Thus

$$\lim_{\epsilon \rightarrow 0} \int_{\Gamma_\epsilon} p(\mathbf{Q}_s) \frac{\partial G(\mathbf{P}, \mathbf{Q}_s)}{\partial n(\mathbf{Q}_s)} d\Gamma = p(\mathbf{P}). \quad (4.16)$$

Using the same approach, the other part of the integral $\int_{\Gamma_\epsilon} G(\mathbf{P}, \mathbf{Q}_s) [\partial p / \partial n(\mathbf{Q}_s)] d\Gamma$ can also be expanded as

$$\int_{\Gamma_\epsilon} G(\mathbf{P}, \mathbf{Q}_s) \frac{\partial p}{\partial n}(\mathbf{Q}_s) d\Gamma = \int_{\Gamma_\epsilon} G(\mathbf{P}, \mathbf{Q}_s) \left[\frac{\partial p}{\partial n}(\mathbf{Q}_s) - \frac{\partial p}{\partial n}(\mathbf{P}) \right] d\Gamma + \frac{\partial p}{\partial n}(\mathbf{P}) \int_{\Gamma_\epsilon} G(\mathbf{P}, \mathbf{Q}_s) d\Gamma.$$

When the $\epsilon \rightarrow 0$, the first term in the right-hand side is zero and the integral of the Green's function in the second term is also zero and the entire integral vanishes, here

$$\int_{\Gamma_\epsilon} G(\mathbf{P}, \mathbf{Q}_s) \frac{\partial p}{\partial n}(\mathbf{Q}_s) d\Gamma = 0. \quad (4.17)$$

Substitute Equation 4.16 and Equation 4.17 into Equation 4.14, to obtain

$$\int_{\Gamma} \left[p(\mathbf{Q}_s) \frac{\partial G(\mathbf{P}, \mathbf{Q}_s)}{\partial n(\mathbf{Q}_s)} - G(\mathbf{P}, \mathbf{Q}_s) \frac{\partial p}{\partial n}(\mathbf{Q}_s) \right] d\Gamma + p(\mathbf{P}) = 0.$$

Rearranging, one obtains Green's third identity as

$$p(\mathbf{P}) = \int_{\Gamma} \left[G(\mathbf{P}, \mathbf{Q}_s) \frac{\partial p}{\partial n}(\mathbf{Q}_s) - \frac{\partial G(\mathbf{P}, \mathbf{Q}_s)}{\partial n(\mathbf{Q}_s)} p(\mathbf{Q}_s) \right] d\Gamma. \quad (4.18)$$

Once the Green's third identity is obtained, one uses the same strategy by using a small sphere containing \mathbf{P} , on $p(\mathbf{P})$ to obtain

$$\begin{aligned} p(\mathbf{P}) &= \int_{\Gamma} \left[G(\mathbf{P}, \mathbf{Q}_s) \frac{\partial p}{\partial n}(\mathbf{Q}_s) - \frac{\partial G(\mathbf{P}, \mathbf{Q}_s)}{\partial n(\mathbf{Q}_s)} p(\mathbf{Q}_s) \right] d\Gamma \\ &+ \int_{\Gamma_\epsilon} \left[G(\mathbf{P}, \mathbf{Q}_s) \frac{\partial p}{\partial n}(\mathbf{Q}_s) - \frac{\partial G(\mathbf{P}, \mathbf{Q}_s)}{\partial n(\mathbf{Q}_s)} p(\mathbf{Q}_s) \right] d\Gamma. \end{aligned} \quad (4.19)$$

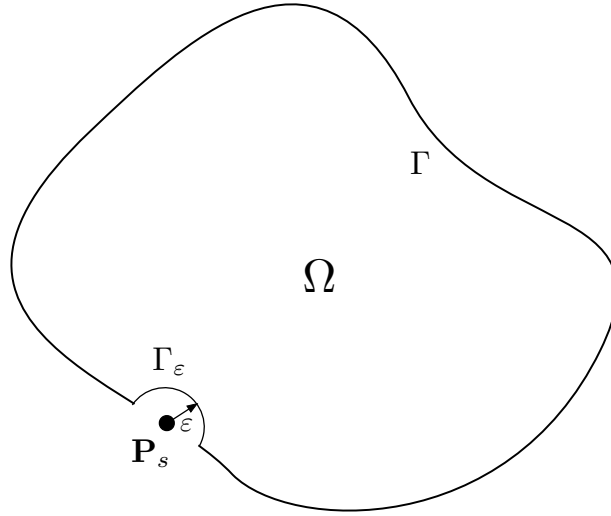


Figure 4.2: The source point is moved onto the boundary and it is surrounded by a semi-circle.

Applying the sphere approach the boundary and \mathbf{P} and \mathbf{P}_s will be identical. Assume the boundary is smooth, then Γ_ϵ becomes a semicircle as shown in Figure 4.2. The Equation 4.19 is expressed as

$$b(\mathbf{P}_s)p(\mathbf{P}_s) = \int_{\Gamma} \left[G(\mathbf{P}_s, \mathbf{Q}_s) \frac{\partial p}{\partial n}(\mathbf{Q}_s) - \frac{\partial G(\mathbf{P}_s, \mathbf{Q}_s)}{\partial n(\mathbf{Q}_s)} p(\mathbf{Q}_s) \right] d\Gamma,$$

where

$$b(\mathbf{P}_s) = 1 - \lim_{\epsilon \rightarrow 0} \int_{\Gamma_\epsilon} \frac{\partial \bar{G}(\mathbf{P}_s, \mathbf{Q}_s)}{\partial n(\mathbf{Q}_s)} d\Gamma = \frac{1}{2}.$$

If the point \mathbf{P} is in the acoustic domain, then $b = 1$, while $b = 0$ if \mathbf{P} is not in the domain. Now, both the source point and the field point in this equation are on the boundary. In order to simplify the expression of the boundary integral equation, one uses \mathbf{x} and \mathbf{y} to denote the source point and field point on the boundary, respectively. The boundary integral equation is expressed as

$$b(\mathbf{x})p(\mathbf{x}) = \int_{\Gamma} \left[G(\mathbf{x}, \mathbf{y}) \frac{\partial p}{\partial n}(\mathbf{y}) - \frac{\partial G}{\partial n}(\mathbf{x}, \mathbf{y}) p(\mathbf{y}) \right] d\Gamma.$$

The definition of interior and exterior acoustic problem is shown in Figure 4.3. In this work, the exterior acoustic problems are considered. The acoustic domain is the outside region of the physical boundaries. The boundary integral equation is still valid. For the acoustic scattering problem the total acoustic pressure is the sum of the acoustic pressure caused by the scattered acoustic wave and the incident wave, (p_{inc}), thus

$$b(\mathbf{x})p(\mathbf{x}) = \int_{\Gamma} \left[G(\mathbf{x}, \mathbf{y}) \frac{\partial p}{\partial n}(\mathbf{y}) - \frac{\partial G}{\partial n}(\mathbf{x}, \mathbf{y}) p(\mathbf{y}) \right] d\Gamma + p_{inc}(\mathbf{x}), \quad (4.20)$$

where $b(\mathbf{x}) = 1 - \lim_{\epsilon \rightarrow 0} \int_{\Gamma_\epsilon} \frac{\partial \bar{G}(\mathbf{x}, \mathbf{y})}{\partial n} d\Gamma$. This boundary integral equation can be used to solve the incident acoustic wave problem.

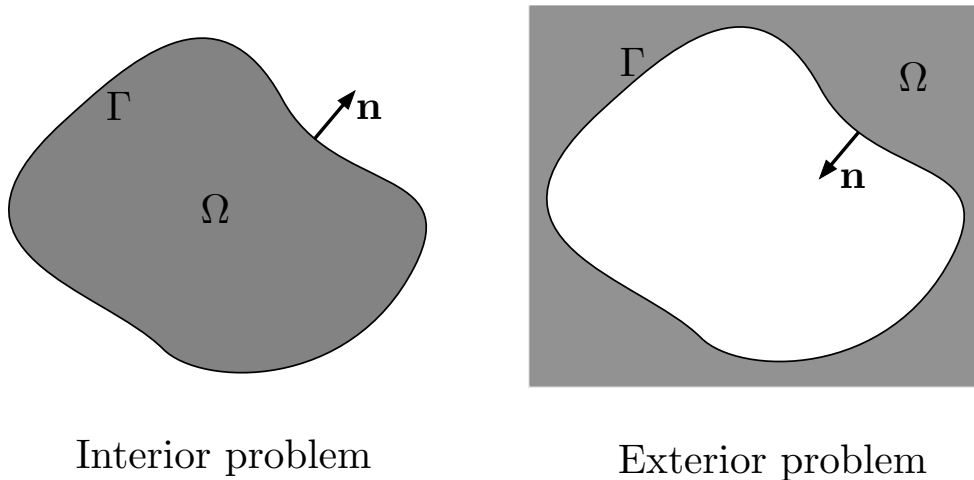


Figure 4.3: Definition of interior and exterior domains.

4.2.2 Acoustic boundary conditions

The Dirichlet boundary condition on the acoustic pressure on the surface is defined by

$$p = \bar{p} \quad \text{on} \quad \Gamma_D.$$

The Neumann boundary condition prescribes the normal derivative of the acoustic pressure on the surface as

$$\frac{\partial p}{\partial n} = \bar{q} \quad \text{on} \quad \Gamma_N,$$

where

$$\Gamma = \Gamma_N \cup \Gamma_D.$$

The pressure of incident wave is also applied as

$$p_{inc}(\mathbf{x}) = \bar{p}_{inc}(\mathbf{x}), \mathbf{x} \in \Gamma.$$

In this project, only Neumann boundary condition is applied to solve the plane wave scattering problem, where

$$\bar{q} = 0 \quad \text{on} \quad \Gamma,$$

and

$$\bar{p}_{inc}(\mathbf{x}) = e^{i\bar{\mathbf{k}} \cdot \mathbf{x}},$$

where $\bar{\mathbf{k}} = \bar{k}\mathbf{d}$ and \mathbf{d} is a vector with a unit length which indicates the direction of the plane wave.

4.2.3 Discretisation of the boundary integral equation

The BEM approximates the boundary integral equation through discretising the boundary into a number of elements as follows

$$\Gamma = \sum_{j=1}^{N_e} \Gamma_j, \quad (4.21)$$

where N_e is the total number of elements and j is the element index. In the conventional boundary element method, there is a geometry error e_g when the boundary is discretised into elements. In this work, the geometry is represented using subdivision surfaces which represent the exact geometry, so that there is no geometry error. The boundary surface of the model is naturally divided into a number of triangular elements by the Loop subdivision control mesh illustrated in Figure 4.4. Numerical integrations is computed within the reference element using Gauss quadrature and mapped into physical space as shown in Figure 4.5. A field point in the reference element has a local coordinates (ξ, η) , where $\xi \in [0, 1]$ and $\eta \in [0, 1]$ and the physical point can be interpolated using the basis functions defined with the local coordinates, so that the physical point is a function of local coordinates, denoted by $\mathbf{y}(\xi, \eta)$. The basis functions used here are the Loop subdivision surfaces basis functions (see Equation 3.12) which are derived from the box-spline functions. However, these functions are computed with barycentric coordinates (u, v, w) . A simple mapping method is used to get the barycentric coordinates:

$$\begin{aligned} u &= \xi, \\ v &= \eta, \\ w &= 1 - \xi - \eta. \end{aligned}$$

The Loop subdivision basis functions of the field point $\mathbf{y}(\xi, \eta)$ are defined in a larger control grid, which is termed the ‘element patch’, as shown in figure 4.4. Each of the basis functions is associated with one control point in the element patch and the field point \mathbf{y} is evaluated with Loop subdivision basis functions and the control point coefficients. The acoustic pressure and its normal derivative at field point \mathbf{y} are discretised by

$$p(\mathbf{y}(\xi, \eta)) = \sum_{k=1}^m N_k(\mathbf{y}(\xi, \eta)) p_k, \quad (4.22)$$

and

$$\frac{\partial p}{\partial n}(\mathbf{y}(\xi, \eta)) = \sum_{k=1}^m N_k(\mathbf{y}(\xi, \eta)) \frac{\partial p_k}{\partial n}, \quad (4.23)$$

where m is the number of basis functions and k is the local index within the element patch. N_k is the basis function corresponding to the k th control point in the element patch. Substituting equations (4.21), (4.22) and (4.23) into the boundary integral equation (4.20), the discretised boundary integral equation is expressed as:

$$\begin{aligned}
 b(\mathbf{x})p(\mathbf{x}) = & \sum_{j=1}^{N_e} \sum_{k=1}^m \frac{\partial p_k^j}{\partial n} \int_{\Gamma_j} N_k(\mathbf{y}(\xi, \eta)) G(\mathbf{x}, \mathbf{y}(\xi, \eta)) d\Gamma \\
 & - \sum_{j=1}^{N_e} \sum_{k=1}^m p_k^j \int_{\Gamma_j} N_k(\mathbf{y}(\xi, \eta)) \frac{\partial G}{\partial n}(\mathbf{x}, \mathbf{y}(\xi, \eta)) d\Gamma + p_{inc}(\mathbf{x}),
 \end{aligned} \tag{4.24}$$

where p_k^j and $\frac{\partial p_k^j}{\partial n}$ are the k th pair of coefficients in element j .

4.3 Boundary element method with subdivision surfaces

4.3.1 Collocation approach

The discretised boundary integral equation (4.24) interpolates the acoustic pressures and its normal derivatives using Loop subdivision surfaces basis functions with the corresponding nodal coefficients. The nodal coefficients are associated with the control points, so that the number of unknown variables in this equation is equal to the number of control points. The boundary element method must build the same number of boundary integral equations as the number of control points to formulate a system of equations to solve for the unknown nodal coefficients. One uses a collocation scheme to choose the locations of a number of source points to generate a system of equations. An alternative method is to apply a Galerkin approach but this involves double integration over the boundary, which is much more costly. The schemes for choosing the collocation points in isogeometric analysis can be found in [119]. Greville abscissae, Demko points and the maxima of B-splines have been considered in collocation methods which directly discretise the strong form of the governing equations. The maxima of the subdivision basis functions, which are associated with the control vertices, are used as the collocation points in this work. For a given element Γ_e , one defines the set of collocation points contained within the

element through its three nodal points with the parametric coordinates

$$C_e := \{\mathbf{x}^e(0, 0), \mathbf{x}^e(1, 0), \mathbf{x}^e(0, 1)\}$$

and construct the global set of collocation points as

$$C = \bigcup_{e=1}^{N_e} C_e. \quad (4.25)$$

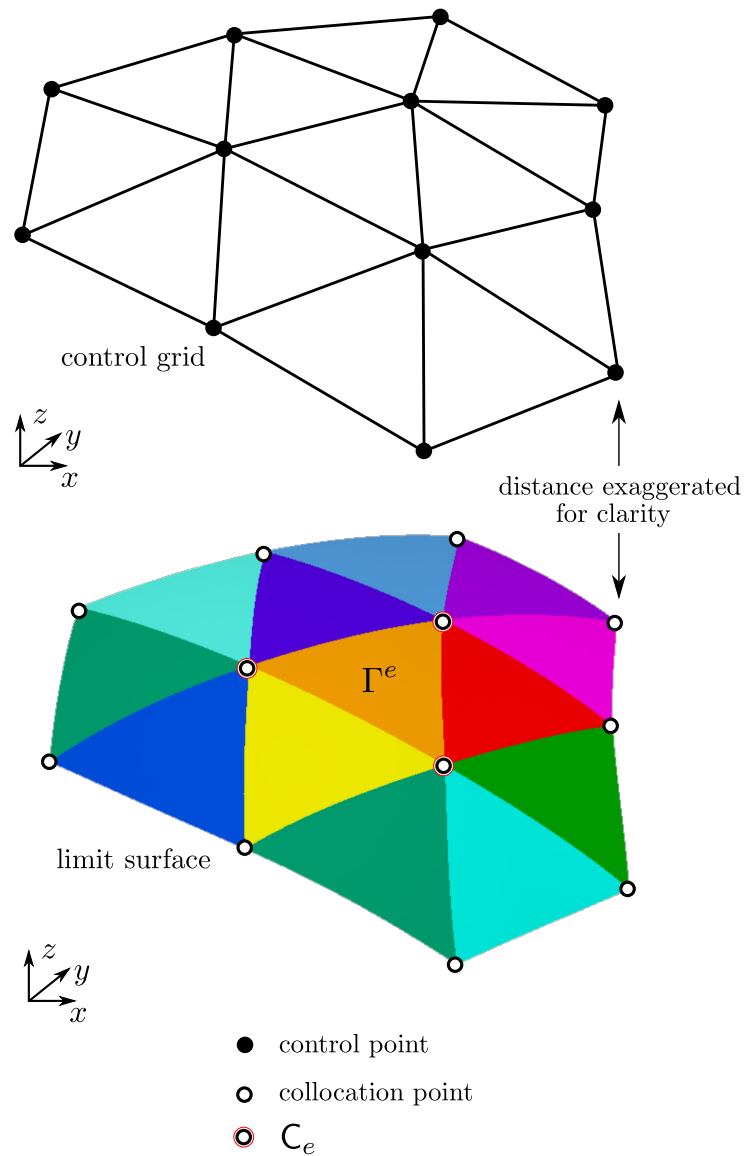


Figure 4.4: Illustration of a control mesh and associated limit surface for a regular patch using the Loop subdivision scheme. Control vertices are located in the control mesh at the intersection of edges and collocation points are defined as the corresponding points on the limit surface. The collocation points of the centre element specified by the set C_e are denoted by red circles. It is important to note that control vertices and collocation points do not coincide.

4.3.2 Derivation of system of equations

There is the same number of collocation points in the set C as the set of control points. One denotes both by the number N_c . For the i th collocation, the boundary integral equation is

$$\begin{aligned} b(\mathbf{x}_i)p(\mathbf{x}_i) &= \sum_{j=1}^{N_e} \sum_{k=1}^{N_c} \frac{\partial p_k^j}{\partial n} \int_{\Gamma_j} N_k(\mathbf{y}(\xi, \eta)) G(\mathbf{x}_i, \mathbf{y}(\xi, \eta)) d\Gamma_j \\ &\quad - \sum_{j=1}^{N_e} \sum_{k=1}^{N_c} p_k^j \int_{\Gamma_j} N_k(\mathbf{y}(\xi, \eta)) \frac{\partial G}{\partial n}(\mathbf{x}_i, \mathbf{y}(\xi, \eta)) d\Gamma_j + p_{inc}(\mathbf{x}_i), \end{aligned} \quad (4.26)$$

where \mathbf{x}_i is the i^{th} collocation point. The index k is now a global index of the basis function. The boundary element system of equations can be assembled as:

$$\mathbf{H}\mathbf{p} = \mathbf{G}\mathbf{q} + \mathbf{p}_{inc}, \quad (4.27)$$

where the entries (i^{th} row and k^{th} column) in matrices \mathbf{G} , \mathbf{H} are computed as

$$G_{ik} = \sum_{j=1}^{N_e} \int_{\Gamma_j} N_k(\mathbf{y}(\xi, \eta)) G(\mathbf{x}_i, \mathbf{y}(\xi, \eta)) d\Gamma_j, \quad (4.28)$$

$$H_{ik} = \sum_{j=1}^{N_e} \int_{\Gamma_j} N_k(\mathbf{y}(\xi, \eta)) \frac{\partial G}{\partial n}(\mathbf{x}_i, \mathbf{y}(\xi, \eta)) d\Gamma_j + N_k(\mathbf{x}_i) b(\mathbf{x}_i). \quad (4.29)$$

When the collocation point \mathbf{x}_i is not contained in element Γ_j , the $N_k(\mathbf{x}_i)$ will always be zero. \mathbf{p} denotes the global vector of the control point coefficients of the acoustic pressures and \mathbf{q} is the global vector of the acoustic pressure normal derivatives coefficients. \mathbf{p}_{inc} is the vector of the incident acoustic pressures at the set of collocation points.

4.3.3 Acceleration methods

Compared to the finite element method, the BEM matrices \mathbf{H} and \mathbf{G} are both fully populated (dense) matrices. Assembling these matrices is $O(N^2)$ complexity and a direct solver for BEM has $O(N^3)$ complexity. The conventional boundary element method requires a large amount of memory to store the entries of the matrices and a large runtime to solve the system of equations

when dealing with large-scale engineering problems. Therefore, matrix compression techniques are commonly used to reduce the overall complexity to $O(N \log N)$ or $O(N)$. The most popular techniques include the fast multipole method (FMM) [120–122] and hierarchical matrices (\mathcal{H} -matrices) [123, 124]. These two techniques are based on the same fundamental concept of approximating the far field values using an efficient hierarchical data structure that allow for fast matrix-vector computations within an iterative solver.

In terms of implementation, \mathcal{H} -matrix is preferred because it perform matrix compression in a purely algebraic manner, but the FMM requires extensive changes to boundary element formulations. An \mathcal{H} -matrix approach using the library HLibPro [125] is implemented in this work. The detailed theory of \mathcal{H} -matrix can be found in [35, 91]. The method computes a low-rank approximation of \mathbf{H} and \mathbf{G} through a specified tolerance by utilising a hierarchical ‘cluster tree’ which separates terms into far-field and near-field sets. The cluster tree is defined through a set of coordinates and bounding boxes related to the underlying basis of the boundary element discretisation. The low-rank compression method used in this work is Adaptive Cross Approximation (ACA) with $O(N \log N)$ complexity. The GMRES algorithm `citesaad1986gmres` is adopted with \mathcal{H} -matrix which reduce the complexity of the solver to $O(N)$.

4.3.4 Evaluation of element integrals

The entries of the BEM matrices, Equation 4.28 and 4.29, are computed as the sum of a number of discretised integrals which should be evaluated within subdivision surfaces elements. Assume the I_e in the following equation is one of the integrals that need to be evaluated in a subdivision surface element Γ_e , i.e.

$$I_e = \int_{\Gamma_e} N_k(\mathbf{y}(\xi, \eta)) G(\mathbf{x}, \mathbf{y}(\xi, \eta)) d\Gamma.$$

The element Γ_e in the Cartesian coordinate system can be considered as a surface in physical space mapped from a reference element with a local coordinate system (ξ, η) as shown in Figure 4.5. Any physical points in Γ_e can be evaluated with the local coordinates. Then the

differential of element area is given by

$$d\Gamma = |\mathbf{J}|d\xi d\eta,$$

where $|\mathbf{J}|$ is the Jacobian of the transformation from the reference element to the physical surfaces. That is

$$|\mathbf{J}| = \sqrt{J_1^2 + J_2^2 + J_3^2},$$

where

$$\begin{aligned} J_1 &= \frac{\partial x_2}{\partial \xi} \frac{\partial x_3}{\partial \eta} - \frac{\partial x_3}{\partial \eta} \frac{\partial x_2}{\partial \xi}, \\ J_2 &= \frac{\partial x_3}{\partial \xi} \frac{\partial x_1}{\partial \eta} - \frac{\partial x_1}{\partial \eta} \frac{\partial x_3}{\partial \xi}, \\ J_3 &= \frac{\partial x_1}{\partial \xi} \frac{\partial x_2}{\partial \eta} - \frac{\partial x_2}{\partial \eta} \frac{\partial x_1}{\partial \xi}. \end{aligned}$$

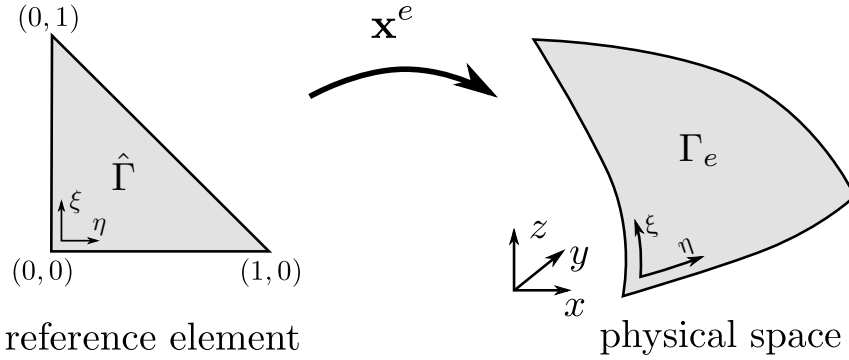


Figure 4.5: Mapping of the reference triangle to the triangle on the subdivision surface. \mathbf{x}^e denotes the mapping operation.

Now, the integral can be calculated within the reference element as

$$I_e = \int_{\eta=0}^1 \int_{\xi=0}^{1-\eta} N_k(\mathbf{y}(\xi, \eta)) G(\mathbf{x}, \mathbf{y}(\xi, \eta)) |\mathbf{J}| d\xi d\eta.$$

Using Gaussian quadrature for triangles, the integral can be approximated by the following expression

$$I_e = \frac{1}{2} \sum_{i=1}^{N_g} \sum_{j=1}^{N_g} N_k(\mathbf{y}(\xi_i, \eta_j)) G(\mathbf{x}, \mathbf{y}(\xi_i, \eta_j)) |\mathbf{J}(\xi_i, \eta_j)| w_{ij}.$$

The number of sampling points is N_g^2 and w_{ij} is the weight associated with the sampling point

$\mathbf{y}(\xi_i, \eta_j)$.

4.3.5 Non-uniqueness problem and the Burton-Miller method

For exterior acoustic problems, the boundary integral equations have non-unique solutions at certain frequencies. This problem was first identified by Copley in 1967 [126]. It is a mathematical limitation of the boundary integral formulation, which does not conform to the physical phenomena. A number of solutions have proposed to overcome this problem. Two notable methods are widely used in a number of boundary element formulations, namely the CHIEF method and the Burton-Miller method. The term CHIEF stands for the combined Helmholtz integral equation formulation. It increases the number of collocation points by adding interior points, which results in an overdetermined system of equations. This implementation is relatively simple but it is only suitable for simple acoustic models. It has difficulties to handle complex models because of the uncertainty in the number of collocation points and the difficulties to determine the positions of the extra interior collocation points. Burton and Miller [127] proposed another method which formulated a new boundary integral equation by taking the partial derivative of the conventional boundary integral equation (CBIE) with respect to the source point normal vector. Because the new boundary integral equation contains a hypersingular term, it is named hypersingular boundary integral equation (HBIE). The linear combination of CBIE and HBIE is formulated to obtain the unique solutions for the exterior acoustic problems:

$$\text{CBIE} + \alpha \text{HBIE} = 0, \quad (4.30)$$

where

$$\alpha = \begin{cases} i, & \text{if } \bar{k} \leq 1, \\ i/\bar{k}, & \text{if } \bar{k} > 1. \end{cases}$$

The hypersingular boundary integral equation is given by

$$b(\mathbf{x}) \frac{\partial p(\mathbf{x})}{\partial n_x} + \int_{\Gamma} \frac{\partial^2 G(\mathbf{x}, \mathbf{y})}{\partial n \partial n_x} p(\mathbf{y}) d\Gamma = \int_{\Gamma} \frac{G(\mathbf{x}, \mathbf{y})}{\partial n_x} \frac{\partial p(\mathbf{y})}{\partial n} d\Gamma + \frac{\partial p_{inc}(\mathbf{x})}{\partial n_x}, \quad (4.31)$$

where n_x denotes the normal vector at the source point \mathbf{x} . The hyper-singular boundary integral equation is derived from the conventional boundary integral equation by partial differentiation with respect to the normal vector at the source point \mathbf{x} . The derivatives of the two kernel functions (4.8) and (4.9) are given by

$$\frac{\partial G(\mathbf{x}, \mathbf{y})}{\partial n_x} = -\frac{e^{i\bar{k}r}}{4\pi r^2} [i\bar{k}r - 1] \frac{\partial r}{\partial n_x}, \quad (4.32)$$

$$\frac{\partial^2 G(\mathbf{x}, \mathbf{y})}{\partial n \partial n_x} = \frac{e^{i\bar{k}r}}{4\pi r^3} \left[[1 - i\bar{k}r] \mathbf{n} \cdot \mathbf{n}_x + [\bar{k}^2 r^2 - 3 [1 - i\bar{k}r]] \frac{\partial r}{\partial n_x} \frac{\partial r}{\partial n} \right]. \quad (4.33)$$

Combining the two boundary integral equations, Equation 4.30 can be written as:

$$\begin{aligned} b(\mathbf{x})p(\mathbf{x}) + \int_{\Gamma} \frac{\partial G(\mathbf{x}, \mathbf{y})}{\partial n} p(\mathbf{y}) d\Gamma + \alpha \left[b(\mathbf{x}) \frac{\partial p(\mathbf{x})}{\partial n_x} + \int_{\Gamma} \frac{\partial^2 G(\mathbf{x}, \mathbf{y})}{\partial n \partial n_x} p(\mathbf{y}) d\Gamma \right] \\ = \int_{\Gamma} G(\mathbf{x}, \mathbf{y}) \frac{\partial p(\mathbf{y})}{\partial n} d\Gamma + p_{inc}(\mathbf{x}) + \alpha \left[\int_{\Gamma} \frac{G(\mathbf{x}, \mathbf{y})}{\partial n_x} \frac{\partial p(\mathbf{y})}{\partial n} d\Gamma + \frac{\partial p_{inc}(\mathbf{x})}{\partial n_x} \right]. \end{aligned}$$

Equation 4.33 contains a hyper-singular ($1/r^3$) after the second derivation of the Green's function. The hyper-singular problem dramatically increases the difficulty of the implementation of the Burton-Miller method. One implements a regularisation method to evaluate the hyper-singular term in the Burton-Miller formulations. The method is illustrated in Section 4.4.3.

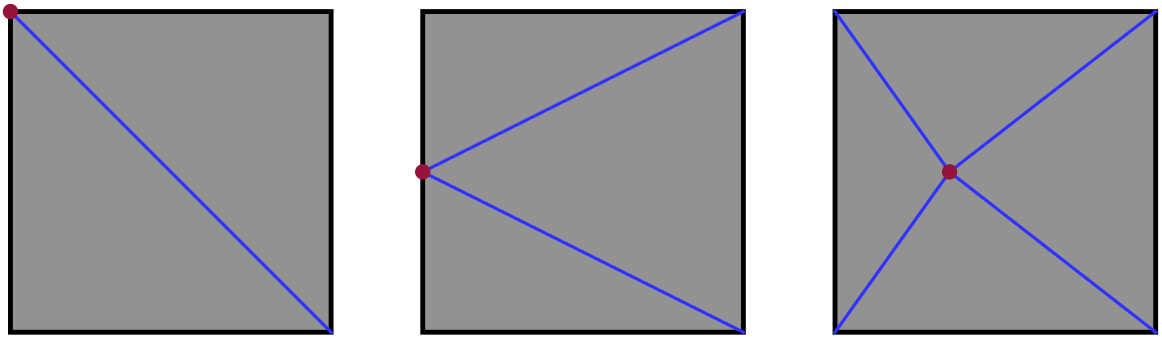
4.4 Singular integration

The Green's function $G = \frac{e^{i\bar{k}r}}{4\pi r}$ has the term ($1/r$) which leads to a weakly singular problem for the integration. The normal derivative of the Green's function $\frac{\partial G}{\partial n} = \frac{e^{i\bar{k}r}}{4\pi r^2} [i\bar{k}r - 1] \frac{\partial r}{\partial n}$ is more difficult to integrate because it contains the term ($1/r^2$) which is considered as strongly singular. The second derivative of the Green's function in the Burton-Miller method is hyper-singular with the term ($1/r^3$).

4.4.1 Weakly-singular integrals: polar coordinate transformation

The integrals in the BEM matrix \mathbf{G} contain the Green's function term $G = \frac{e^{i\bar{k}r}}{4\pi r}$. When the collocation point is located in the target integration element, the distant r between the collocation

point and the Gauss point is relatively small. In this case, the integral is weakly singular can not be computed accurately with conventional Gauss quadrature. An efficient method for dealing with weakly singular integrals in three dimensional surface elements is the polar coordinate transformation. The method divides the integration element into several sub-elements using a scheme dependent on the position of singular point as shown in Figure 4.6. The elements in Loop subdivision surfaces are all triangular elements and the collocation points (singular points) are always located at one of the corner points, so the triangular element do not need to be subdivided.



• Singular point

Figure 4.6: Subdivision for Polar coordinate transformation (If the singular point is located at one of the corners, divide the element through the diagonal line (left). If the singular point lies on one of the edges, divide the element into three triangle elements (middle). If the singular point lies in the element, the element will be divided into four triangular elements (right)).

Illustrate the polar coordinate transformation method by assuming the integral will be computed in element Γ_e and the field point in this element \mathbf{y} has a local coordinates (ξ, η) . The integral is expressed as

$$I = \int_{\Gamma_e} G(\mathbf{x}, \mathbf{y}(\xi, \eta)) N(\mathbf{y}(\xi, \eta)) |\mathbf{J}(\mathbf{y}(\xi, \eta))| d\xi d\eta.$$

The polar coordinates system is built at the singular point \mathbf{x} as the origin, which has an local coordinates (ξ^s, η^s) . Then, the local coordinates of the field point \mathbf{y} can be expressed using polar

coordinates by

$$\begin{aligned}\xi &= \xi^s + \bar{\rho} \cos \theta, \\ \eta &= \eta^s + \bar{\rho} \sin \theta.\end{aligned}$$

Then the derivatives of the coordinates can be expressed as

$$\begin{aligned}d\xi &= d\bar{\rho} \cos \theta - \bar{\rho} \sin \theta d\theta, \\ d\eta &= d\bar{\rho} \sin \theta + \bar{\rho} \cos \theta d\theta.\end{aligned}$$

and their product $d\xi d\eta$ is calculated as:

$$\begin{aligned}d\xi d\eta &= [d\bar{\rho} \cos \theta - \bar{\rho} \sin \theta d\theta] [d\bar{\rho} \sin \theta + \bar{\rho} \cos \theta d\theta] \\ &= \sin \theta \cos \theta d\bar{\rho} d\bar{\rho} - \bar{\rho} \sin^2 \theta d\theta d\bar{\rho} \\ &\quad + \bar{\rho} \cos^2 \theta d\bar{\rho} d\theta - \bar{\rho}^2 \sin \theta \cos \theta d\theta d\theta.\end{aligned}$$

The terms $d\bar{\rho} d\bar{\rho}$ and $d\theta d\theta$ vanish and $d\theta d\bar{\rho} = -d\bar{\rho} d\theta$, so that $d\xi d\eta = \bar{\rho} d\bar{\rho} d\theta$. After the subdivision scheme is applied to each sub-element, a quadrilateral element will be divided into a number of triangular sub-elements. The original integral is also subdivided into a number of sub-integrals as

$$I = \sum_{j=1}^{n_e} \int_{\theta_{j-1}}^{\theta_j} \int_0^{\hat{r}(\theta)} G(\bar{\rho}, \theta) N(\bar{\rho}, \theta) |\mathbf{J}(\bar{\rho}, \theta)| \bar{\rho} d\bar{\rho} d\theta, \quad (4.34)$$

where n_e is the number of sub-elements. (θ_{j-1}, θ_j) is the angular boundary of the sub-element j in polar coordinates system. $\hat{r}(\theta)$ gives a parametrisation of the boundary of the sub-element according to the angle θ in polar coordinates system. It can be calculated from the following equation

$$\hat{r}(\theta) = \frac{h_j}{\cos \theta},$$

where $\bar{\theta}$, \hat{r} and h_j are defined in Figure 4.7. After the Polar transformation, the integrals in Equation 4.34 are no longer singular.

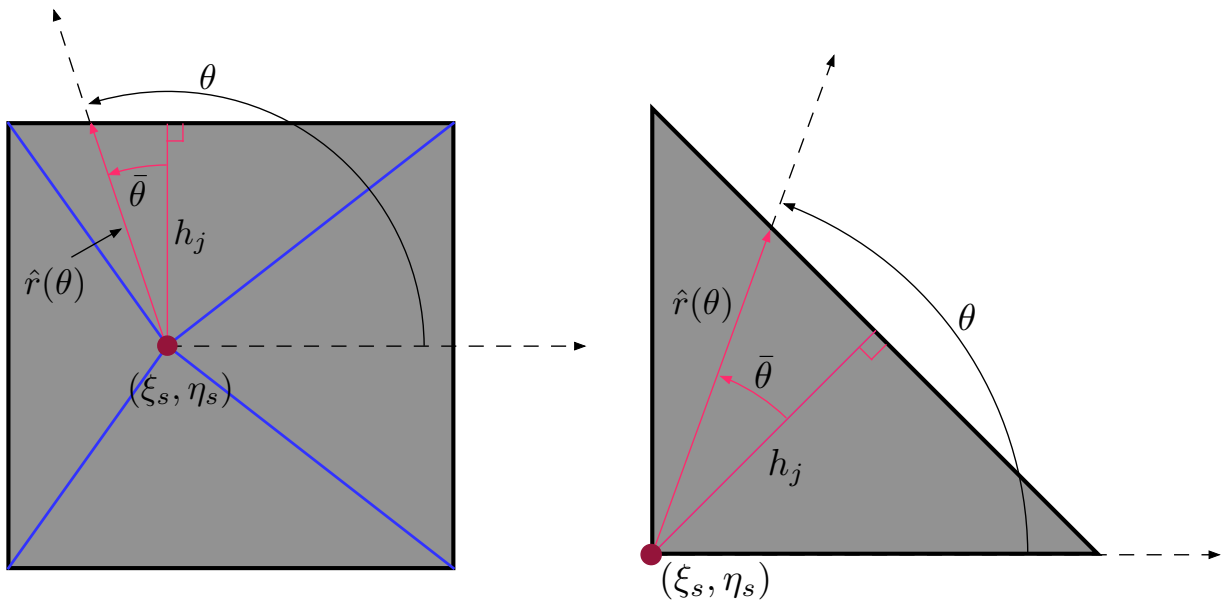


Figure 4.7: The definitions of the variables in polar coordinates transformation for a standard quadrilateral element (left) and a triangular element in the Loop subdivision surfaces (right).

Convergence study

A convergence study is conducted to determine the number of quadrature points that should be used in the numerical simulations. One chooses an arbitrary element from a subdivision discretisation and performs a polar transformation. After that, the integration scheme stated above is applied. The kernel function is the Green's function of Helmholtz equation given in Equation 4.8. The integration of this kernel function with 3600 (60×60) quadrature points is used as a reference results to compute quadrature errors. The singular point has a parametric coordinate $(0, 0)$. For subdivision surface discretisations, this is the worst scenario for polar coordinates transformation as the singular point corresponds to an extraordinary vertex of the control mesh. The integration error of an element with an extraordinary vertex is compared with the regular case. Table 4.1 shows the quadrature errors decrease while increasing number of quadrature points. e_{L_2} denotes the L_2 normalised error. To consider the computational efficiency, a 4×4 quadrature scheme is chosen for numerical examples in the following sections.

Table 4.1: Integral errors after polar coordinates transformation

Number of quadrature points	e_{L_2} (regular element)	e_{L_2} (element with extraordinary vertex)
4	1.64e-3	1.727e-2
16	3.342e-5	4.548e-3
64	5.941e-6	1.756e-3
100	8.539e-6	6.489e-4
144	2.705e-6	7.212e-4
196	2.382e-7	2.451e-4

4.4.2 Strongly-singular integrals

Similar to the \mathbf{G} matrix, the integral in the \mathbf{H} matrix also has problems with singular terms because it contains the derivative of the Green's function $\frac{\partial G}{\partial n} = \frac{e^{i\bar{k}r}}{4\pi r^2} (i\bar{k}r - 1) \frac{\partial r}{\partial n}$. But this term has $\frac{1}{r^2}$ which is considered as a strongly singular problem and more difficult to evaluate. Evaluation of strong singular integrals is a common but challenging problem in the development of boundary element method. A number of researchers have studied this problem and provided reliable solutions [128–131]. This work uses the regularisation process to deal with the problem. The regularisation method manipulates the singular kernel in boundary integral equation and builds a new boundary integral equation to avoid integrating singular terms. We first consider the strongly singular term in Equation 4.20. Subtract a static normal derivative of Green's function $\frac{\partial \bar{G}}{\partial n} = \frac{1}{4\pi r^2}$ from the normal derivative of acoustic Green's function and add it back as

$$\int_{\Gamma} \frac{\partial G(\mathbf{x}, \mathbf{y})}{\partial n} p(\mathbf{y}) \, d\Gamma = \int_{\Gamma} \left[\frac{\partial G(\mathbf{x}, \mathbf{y})}{\partial n} - \frac{\partial \bar{G}(\mathbf{x}, \mathbf{y})}{\partial n} \right] p(\mathbf{y}) \, d\Gamma + \int_{\Gamma} \frac{\partial \bar{G}(\mathbf{x}, \mathbf{y})}{\partial n} p(\mathbf{y}) \, d\Gamma. \quad (4.35)$$

The first integral on the right-hand side is now regularised and no longer singular but the second integral still has a singularity. After this step, the singularity problem of the Helmholtz Green's function is shifted to a static Laplace Green's function. The singular part at the source point \mathbf{x} can be subtracted from the integral and the integral is expanded as

$$\int_{\Gamma} \frac{\partial \bar{G}(\mathbf{x}, \mathbf{y})}{\partial n} p(\mathbf{y}) \, d\Gamma = \int_{\Gamma} \frac{\partial \bar{G}(\mathbf{x}, \mathbf{y})}{\partial n} [p(\mathbf{y}) - p(\mathbf{x})] \, d\Gamma + \int_{\Gamma} \frac{\partial \bar{G}(\mathbf{x}, \mathbf{y})}{\partial n} \, d\Gamma p(\mathbf{x}), \quad (4.36)$$

where the static Green's function derivative $\int_{\Gamma} \frac{\partial \bar{G}(\mathbf{x}, \mathbf{y})}{\partial n} d\Gamma = -\frac{1}{2}$. When the source point is on a smooth surface, $b(\mathbf{x})$ in the boundary integral equation (4.20) is equal to $\frac{1}{2}$. Then, the $\int_{\Gamma} \frac{\partial \bar{G}(\mathbf{x}, \mathbf{y})}{\partial n} d\Gamma p(\mathbf{x})$ cancels with $b(\mathbf{x})p(\mathbf{x})$. The left-hand side of Equation 4.20 is transformed as

$$b(\mathbf{x})p(\mathbf{x}) + \int_{\Gamma} \frac{\partial G(\mathbf{x}, \mathbf{y})}{\partial n} p(\mathbf{y}) d\Gamma = \int_{\Gamma} \left[\frac{\partial G(\mathbf{x}, \mathbf{y})}{\partial n} p(\mathbf{y}) - \frac{\partial \bar{G}(\mathbf{x}, \mathbf{y})}{\partial n} p(\mathbf{x}) \right] d\Gamma.$$

The boundary integral equation (4.20) is now regularised as

$$\int_{\Gamma} \left[\frac{\partial G(\mathbf{x}, \mathbf{y})}{\partial n} p(\mathbf{y}) - \frac{\partial \bar{G}(\mathbf{x}, \mathbf{y})}{\partial n} p(\mathbf{x}) \right] d\Gamma = \int_{\Gamma} G(\mathbf{x}, \mathbf{y}) \frac{\partial p(\mathbf{y})}{\partial n} d\Gamma + p_{inc}(\mathbf{x}).$$

This new boundary integral equation does not have singularities.

4.4.3 Hyper-singular integrals

The regularisation of HBIE is more difficult because of the hyper-singular term $\frac{1}{r^3}$. Similar to the treatment of strongly singular term, first subtract the hyper-singularity with the corresponding static Green's function derivative:

$$\int_{\Gamma} \frac{\partial^2 G(\mathbf{x}, \mathbf{y})}{\partial n \partial n_x} p(\mathbf{y}) d\Gamma = \int_{\Gamma} \left[\frac{\partial^2 G(\mathbf{x}, \mathbf{y})}{\partial n \partial n_x} - \int_{\Gamma} \frac{\partial^2 \bar{G}(\mathbf{x}, \mathbf{y})}{\partial n \partial n_x} \right] p(\mathbf{y}) d\Gamma + \int_{\Gamma} \frac{\partial^2 \bar{G}(\mathbf{x}, \mathbf{y})}{\partial n \partial n_x} p(\mathbf{y}) d\Gamma. \quad (4.37)$$

The first term is non-singular and the second term can be further transformed by subtracting the first two terms of the Taylor expansion and adding these terms back gives

$$\begin{aligned} \int_{\Gamma} \frac{\partial^2 \bar{G}(\mathbf{x}, \mathbf{y})}{\partial n \partial n_x} p(\mathbf{y}) d\Gamma &= \int_{\Gamma} \frac{\partial^2 \bar{G}(\mathbf{x}, \mathbf{y})}{\partial n \partial n_x} [p(\mathbf{y}) - p(\mathbf{x}) - \nabla p(\mathbf{y})(\mathbf{y} - \mathbf{x})] d\Gamma \\ &+ p(\mathbf{y}) \int_{\Gamma} \frac{\partial^2 \bar{G}(\mathbf{x}, \mathbf{y})}{\partial n \partial n_x} d\Gamma + \int_{\Gamma} \frac{\partial^2 \bar{G}(\mathbf{x}, \mathbf{y})}{\partial n \partial n_x} [\nabla p(\mathbf{y})(\mathbf{y} - \mathbf{x})] d\Gamma. \end{aligned} \quad (4.38)$$

The term containing the gradient of the acoustic pressure can be computed as

$$\nabla p(\mathbf{y})(\mathbf{y} - \mathbf{x}) = \sum_{k=1}^2 \frac{\partial p(\mathbf{x})}{\partial \mathbf{v}_k} \mathbf{v}_k \cdot (\mathbf{y} - \mathbf{x}),$$

where $\mathbf{v}_1, \mathbf{v}_2$ refer to the two tangent vectors at the surface point. The following Laplace integral identities are used to regularise the expanded singular term:

$$\int_{\Gamma} \frac{\partial^2 \bar{G}(\mathbf{x}, \mathbf{y})}{\partial n \partial n_x} d\Gamma = 0 \quad (4.39)$$

$$\int_{\Gamma} \frac{\partial^2 \bar{G}(\mathbf{x}, \mathbf{y})}{\partial n \partial n_x} (\mathbf{y} - \mathbf{x}) d\Gamma = \int_{\Gamma} \frac{\partial \bar{G}(\mathbf{x}, \mathbf{y})}{\partial n_x} \mathbf{n}(\mathbf{y}) d\Gamma - \frac{1}{2} \mathbf{n}(\mathbf{x}). \quad (4.40)$$

Substituting the identity (4.39) into the expanded equation (4.38), the second term on the right-hand side can be eliminated. Using identity (4.40) to modify the last term on the right-hand side, the new expansion form is reduced to weakly and strongly singular integrals:

$$\begin{aligned} \int_{\Gamma} \frac{\partial^2 \bar{G}(\mathbf{x}, \mathbf{y})}{\partial n \partial n_x} p(\mathbf{y}) d\Gamma &= \int_{\Gamma} \frac{\partial^2 \bar{G}(\mathbf{x}, \mathbf{y})}{\partial n \partial n_x} \left[p(\mathbf{y}) - p(\mathbf{x}) - \sum_{k=1}^2 \frac{\partial p(\mathbf{x})}{\partial \mathbf{v}_k} \mathbf{v}_k \cdot (\mathbf{y} - \mathbf{x}) \right] d\Gamma \\ &+ \sum_{k=1}^2 \frac{\partial p(\mathbf{x})}{\partial \mathbf{v}_k} \int_{\Gamma} \left[\frac{\partial \bar{G}(\mathbf{x}, \mathbf{y})}{\partial n_x} \mathbf{v}_k \cdot \mathbf{n}(\mathbf{y}) + \frac{\partial \bar{G}(\mathbf{x}, \mathbf{y})}{\partial n} \mathbf{v}_k \cdot \mathbf{n}(\mathbf{x}) \right] d\Gamma. \end{aligned}$$

This equation can be expressed as

$$\begin{aligned} \int_{\Gamma} \frac{\partial^2 \bar{G}(\mathbf{x}, \mathbf{y})}{\partial n \partial n_x} p(\mathbf{y}) d\Gamma &= \int_{\Gamma} \frac{\partial^2 \bar{G}(\mathbf{x}, \mathbf{y})}{\partial n \partial n_x} \left[p(\mathbf{y}) - p(\mathbf{x}) - \sum_{k=1}^2 \frac{\partial p(\mathbf{x})}{\partial \mathbf{v}_k} \mathbf{v}_k \cdot (\mathbf{y} - \mathbf{x}) \right] d\Gamma \\ &+ \sum_{k=1}^2 \frac{\partial p(\mathbf{x})}{\partial \mathbf{v}_k} \int_{\Gamma} \frac{\partial \bar{G}(\mathbf{x}, \mathbf{y})}{\partial n_x} \mathbf{v}_k \cdot \mathbf{n}(\mathbf{y}) d\Gamma - \frac{1}{2} \sum_{k=1}^2 \frac{\partial p(\mathbf{x})}{\partial \mathbf{v}_k} \mathbf{v}_k \cdot \mathbf{n}(\mathbf{x}). \end{aligned} \quad (4.41)$$

The weak singularity can be easily eliminated through polar integration. Substitute Equation 4.41 into the Equation 4.37, the whole hyper-singular integral can be written as

$$\begin{aligned} \int_{\Gamma} \frac{\partial^2 G(\mathbf{x}, \mathbf{y})}{\partial n \partial n_x} p(\mathbf{y}) d\Gamma &= \int_{\Gamma} \left[\frac{\partial^2 G(\mathbf{x}, \mathbf{y})}{\partial n \partial n_x} - \frac{\partial^2 \bar{G}(\mathbf{x}, \mathbf{y})}{\partial n \partial n_x} p(\mathbf{y}) \right] d\Gamma \\ &+ \int_{\Gamma} \frac{\partial^2 \bar{G}(\mathbf{x}, \mathbf{y})}{\partial n \partial n_x} \left[p(\mathbf{y}) - p(\mathbf{x}) - \sum_{k=1}^2 \frac{\partial p(\mathbf{x})}{\partial \mathbf{v}_k} \mathbf{v}_k \cdot (\mathbf{y} - \mathbf{x}) \right] d\Gamma \\ &+ \sum_{k=1}^2 \frac{\partial p(\mathbf{y})}{\partial \mathbf{v}_k} \int_{\Gamma} \frac{\partial \bar{G}(\mathbf{x}, \mathbf{y})}{\partial n_x} \mathbf{v}_k \cdot \mathbf{n}(\mathbf{y}) d\Gamma - \frac{1}{2} \sum_{k=1}^2 \frac{\partial p(\mathbf{x})}{\partial \mathbf{v}_k} \mathbf{v}_k \cdot \mathbf{n}(\mathbf{x}). \end{aligned}$$

For the right-hand side of HBIE (4.31), the strongly singular integral also can be regularised with a identity using the same method with CBIE. The final expression of the boundary integral equation is given as

$$\begin{aligned} &\int_{\Gamma} \left[\frac{\partial^2 G(\mathbf{x}, \mathbf{y})}{\partial n \partial n_x} - \frac{\partial^2 \bar{G}(\mathbf{x}, \mathbf{y})}{\partial n \partial n_x} \right] p(\mathbf{y}) d\Gamma + \int_{\Gamma} \frac{\partial^2 \bar{G}(\mathbf{x}, \mathbf{y})}{\partial n \partial n_x} \left[p(\mathbf{y}) - p(\mathbf{x}) - \sum_{k=1}^2 \frac{\partial p(\mathbf{x})}{\partial \mathbf{v}_k} \mathbf{v}_k \cdot [\mathbf{y} - \mathbf{x}] \right] d\Gamma \\ &+ \sum_{k=1}^2 \frac{\partial p(\mathbf{y})}{\partial \mathbf{v}_k} \int_{\Gamma} \frac{\partial \bar{G}(\mathbf{x}, \mathbf{y})}{\partial n_x} \mathbf{v}_k \cdot \mathbf{n}(\mathbf{y}) d\Gamma - \frac{1}{2} \sum_{k=1}^2 \frac{\partial p(\mathbf{x})}{\partial \mathbf{v}_k} \mathbf{v}_k \cdot \mathbf{n}(\mathbf{x}) \\ &= \int_{\Gamma} \left[\frac{\partial G(\mathbf{x}, \mathbf{y})}{\partial n_x} + \frac{\partial \bar{G}(\mathbf{x}, \mathbf{y})}{\partial n_x} \right] \frac{\partial p(\mathbf{y})}{\partial n} d\Gamma - \int_{\Gamma} \frac{\partial \bar{G}(\mathbf{x}, \mathbf{y})}{\partial n} \left[\frac{\partial p(\mathbf{y})}{\partial n} - \frac{\partial p(\mathbf{x})}{\partial n_x} \right] d\Gamma + \frac{\partial p_{inc}(\mathbf{x})}{\partial n_x}. \end{aligned}$$

The remaining weakly singularity can be cancelled using a Polar transformation.

4.5 Numerical verification

4.5.1 Plane wave scattered by a rigid sphere

Problem setup

The superior accuracy of isogeometric acoustic boundary element method based on T-splines has been illustrated in [87]. A similar advantage is expected when using subdivision surfaces discretisation performing the same acoustic analysis. This section replicates the problem of a plane wave impinging on a sphere simulation as performed in [87] with Loop subdivision surfaces. The problem is defined in Figure 4.8. An incident plane wave propagating in the positive x - direction and a hard sphere with a radius r_s scatters the wave. The incident plane wave is expressed as:

$$p_{inc} = M e^{i\bar{k}\mathbf{d}\cdot\mathbf{x}},$$

where M denotes the amplitude of the acoustic plane wave and \mathbf{d} is a unit vector which indicates the propagating direction of the wave. In this test, a unit amplitude ($M = 1$) and a positive x direction ($\mathbf{d} = (1, 0, 0)$) are chosen, so the incident pressure is defined as $p_{inc} = e^{i\bar{k}x_1}$ and applied as a boundary condition. Assume the derivative of acoustic pressure on the surface $\frac{\partial p}{\partial n} = 0$, then the acoustic pressure can be solved using the system of equations (4.27).

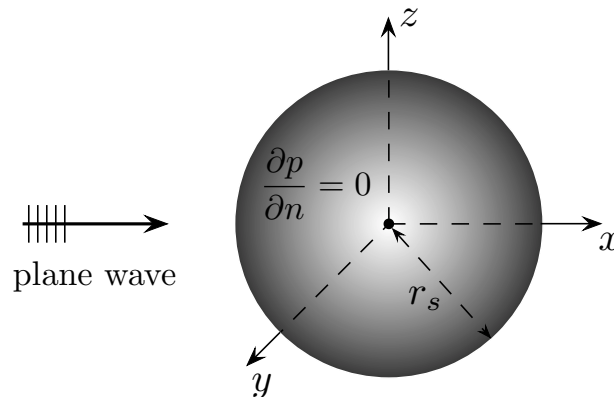


Figure 4.8: Definition of plane wave impinging on a sphere.

Analytical solution

This is a benchmark problem for computational acoustics and the analytical solution is given in [132–134]. The acoustic pressure at the sample point is expressed as

$$p(r, \theta) = p_0 \sum_{n=1}^{\infty} -\frac{i^n (2n+1) j'_n(\bar{k}r_s)}{h'_n(\bar{k}r_s)} L_n(\cos \theta) h_n(\bar{k}r), \quad (4.42)$$

where p_0 is the magnitude of the incident wave, L_n is the n th Legendre function, h_n and h'_n are the n th Hankel function and its derivative respectively. j'_n is the derivative of the n th spherical Bessel function and r_s is the radius of the sphere.

Mesh refinement study

Figure 4.9a illustrates an initial control polygon mesh and Figure 4.9b shows the Loop subdivision limit surface of this control mesh. In order to study the convergence of the coupled method, two different mesh refinement strategies are used to generate successively finer meshes for the same sphere geometry. The two strategies are subdivision refinement and Least squares fitting (L_2 projection). We applied the Loop subdivision refinement algorithm stated in Section 3.2.3 twice to the initial mesh. Two successively refined meshes (a) and (b) were generated and the two control meshes used to evaluate the same limit surface as the initial control mesh. In general, it is an advantage when the limit surfaces are the design geometries as there will be no geometry error throughout the entire analysis process. But in this benchmark problem for numerical verification, the two refined meshes and the initial mesh all exhibit non-negligible geometry errors because their common limit surface has a deviation from the sphere geometry. A second refinement scheme performed using a least squares fitting of the subdivision surface to an analytical sphere surface with diameter $a = 1$. This generated two successively refined meshes (c) and (d). The geometry error will be successively reduced because mesh (d) better represents the geometry of the sphere than mesh (c). Figure 4.10 shows the control mesh (d) and its limiting surface.

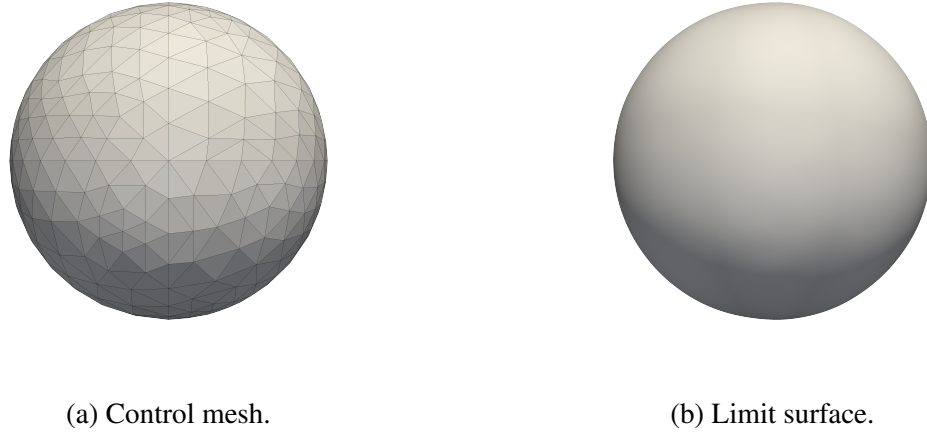


Figure 4.9: The initial coarse Loop subdivision discretisation with 438 vertices used to generate control meshes (a) through to (d) in Table 4.2 and Table 4.3. The control vertices are placed such that they lie on a sphere with diameter $a = 1$.

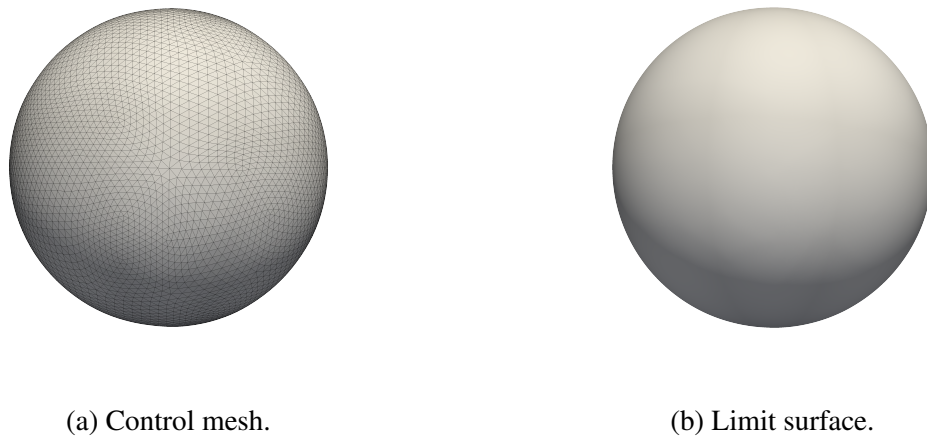


Figure 4.10: The Loop subdivision discretisation of a sphere geometry with 6978 vertices corresponding to control mesh (d) in Table 4.3. The control vertex positions are determined such that the limit surface approximates a sphere with diameter $a = 1$.

For each control mesh the relative geometry error ε_g of the limit surface is calculated as

$$\varepsilon_g = \frac{\|\mathbf{x}^h - \mathbf{x}\|_0}{\|\mathbf{x}\|_0},$$

where \mathbf{x}^h and \mathbf{x} are physical coordinates on the Loop subdivision surface and analytical surface

respectively with

$$\|\cdot\|_0 := \left[\int_{\Gamma} (\cdot)^2 d\Gamma \right]^{1/2}.$$

Table 4.2 and 4.3 details each of the control meshes for both refinement schemes. Table 4.2 shows that the subdivision refinement produces a constant geometry error ($\varepsilon_g = 0.93\%$) which means the limiting surfaces are one and the same. Table 4.3 shows the geometry errors will converge to zero when the new control vertices are L_2 projected onto the analytical sphere surface.

Table 4.2: Mesh properties for subdivision refinement

control mesh	initial	(a)	(b)
number of vertices	438	1746	6978
n_e	872	3488	13952
ε_g	0.93%	0.93%	0.93%

Table 4.3: Mesh properties for subdivision refinement and subsequent L_2 projection

control mesh	initial	(c)	(d)
number of vertices	438	1746	6978
n_e	872	3488	13952
ε_g	0.93%	0.24%	0.06%

Convergence study

A relatively low frequency problem with normalised wavenumber of $\bar{k}a = 10$ is used to to conduct the convergence study. The magnitude of the total acoustic pressure at sample points located on the x - y plane of the sphere surface is calculated as

$$|p_t| = \sqrt{\text{Re}(p_t)^2 + \text{Im}(p_t)^2}.$$

Results for control meshes (a) and (b) are shown in Figure 4.11. These illustrate convergence to a solution that is distinct from the analytical solution due to a geometry difference between the limiting surface and the analytical surface. However, the results for control meshes (c) and (d) (Figure 4.12) illustrate convergence to the analytical solution. It demonstrates the importance

of controlling geometry error when verifying the coupled method. Therefore, care must be taken to ensure that the limit surface provides an accurate representation of required model geometry because further application of the Loop subdivision refinement algorithm will not overcome the inherent error induced by the incorrect geometry representation. In the case that the limit surface is an accurate representation of the sphere our method converges to the analytical coupled solution and thus verifies the implementation.

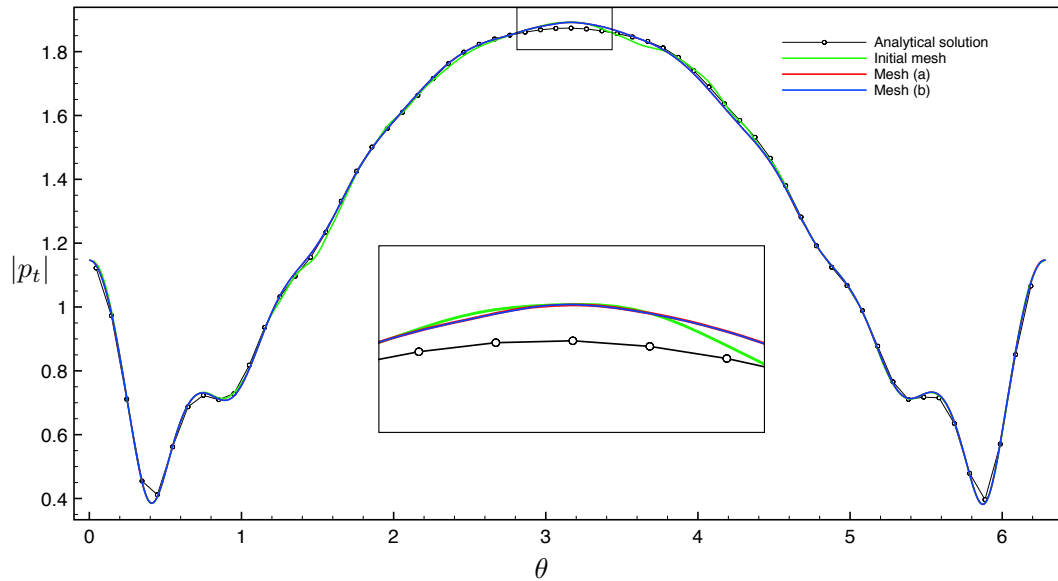


Figure 4.11: Rigid sphere scattering a plane wave with $\bar{k}a = 10$: surface acoustic potential magnitude along x - y plane using control meshes (a) and (b). The inset image illustrates convergence to a solution which does not correspond to the analytical solution due to the non-negligible geometrical error of the limit surface.

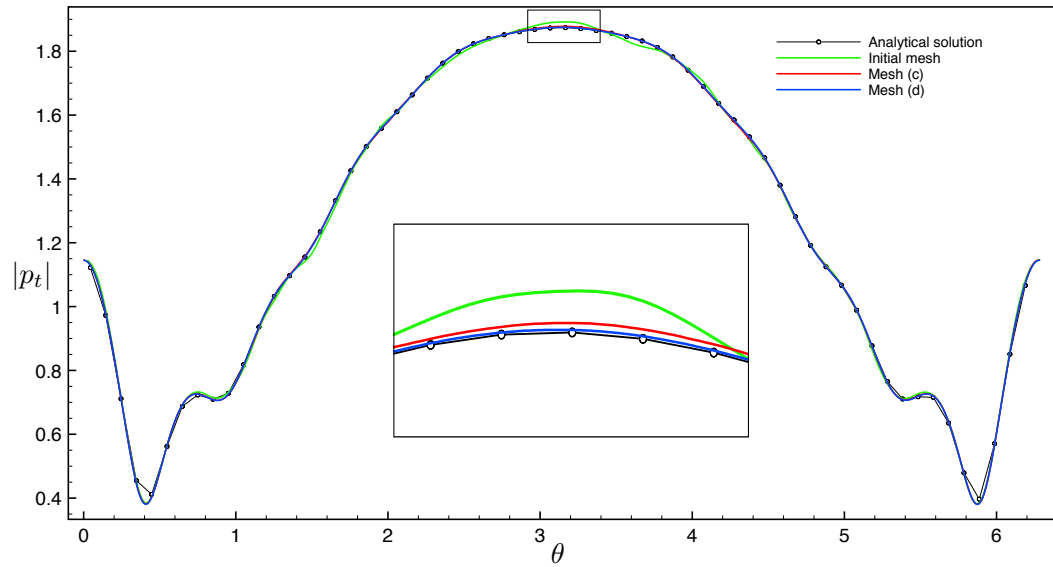


Figure 4.12: Rigid sphere scattering a plane wave with $\bar{k}a = 10$: surface acoustic potential magnitude along x - y plane using control meshes (c) and (d). L_2 projection of control vertices onto the analytical sphere surface leads to a reduced geometrical error in the limit surface and convergence to the analytical solution.

Comparison with Lagrangian discretisation

A mesh with quartic (4th order) Lagrangian elements is used for comparison between subdivision surfaces and a Lagrangian discretisation. The mesh properties are shown in Table 4.4. The problem used in the comparison is defined in Figure 4.13. An acoustically hard sphere is impinged by a plane-wave with $ka = 8$. Different from the previous problem, the sample points are in the far field, where $r = 5m$. The magnitude of acoustic pressure at the sample points are computed using the quartic Lagrangian discretisation and two subdivision discretisations constructed with the initial mesh and mesh (c). 8×8 Gauss points per element are used for all cases.

Table 4.4: Mesh properties for Lagrangian discretisation

control mesh	4 th order Lagrangian
number of vertices	1092
n_e	281
ε_g	0.48%

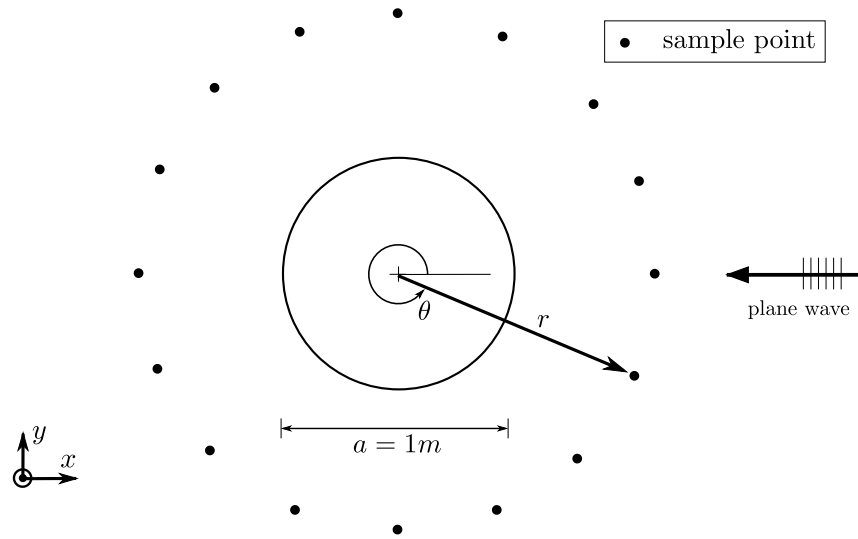


Figure 4.13: Sample points in acoustic domain.

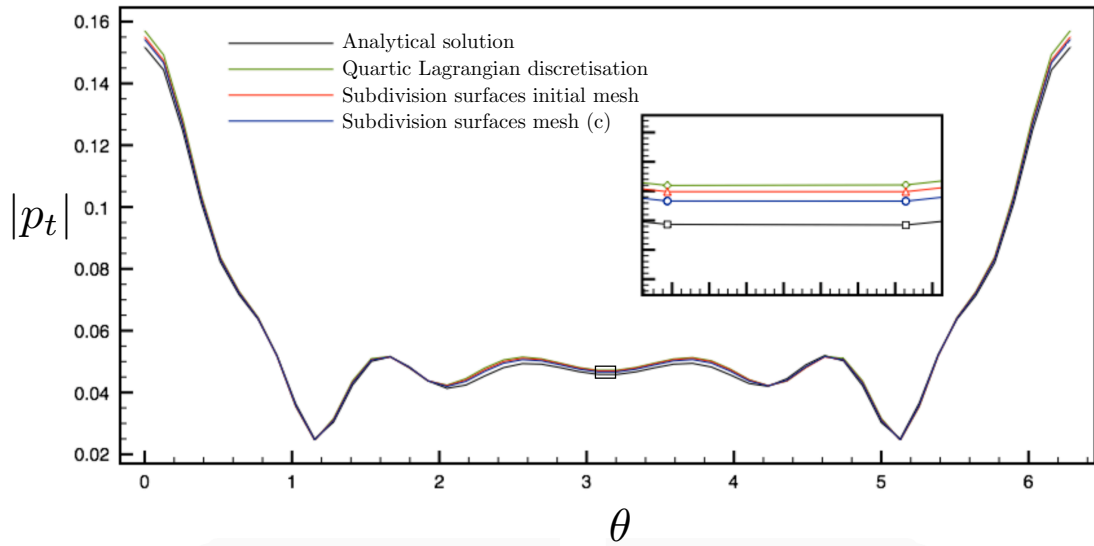


Figure 4.14: A comparison between Lagrangian discretisations and subdivision surfaces ($k = 8$).

The results for the three meshes at each of the sampling points are shown in Figure 4.14 along with the analytical solution. A closeup view of this plot illustrates that both subdivision discretisations deliver higher accuracies compared to the Lagrangian discretisation even if it has a lower geometry error and more collocation points. By adopting the high order basis functions of subdivision surfaces, a higher accuracy per degree of freedom is obtained over equivalent Lagrangian discretisations.

4.5.2 Acoustic wave scattered by a mannequin model

This numerical example will consider the ability of the present method to provide high-order discretisations of arbitrarily complex geometries. The model we consider is that of a mannequin which is often used to determine important acoustic parameters such as the Head Related Transfer Function known to be important for the human perception of sound [135]. An initial triangulation of the mannequin surface is constructed as shown in Figure 4.15 with 2,834 vertices and then apply one level of subdivision refinement to generate the control grid shown in Figure 4.16 with 11,330 vertices. Both control grids exhibit a common limit surface as shown in Figure 4.17.

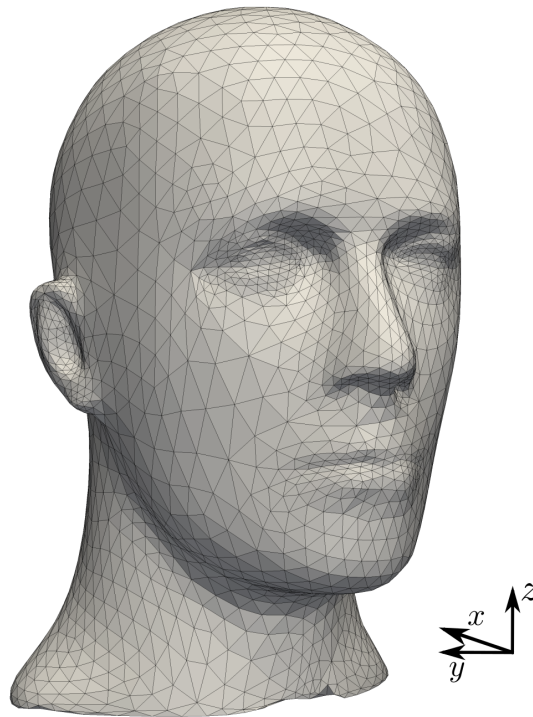


Figure 4.15: Mannequin problem: control grid with 2,834 vertices. The minimum bounding box for this model and the refined model in Figure 4.16 is defined by $[x_i^{min}, x_i^{max}]^3 = [-179.0, 51.0] \times [-81.6, 92.4] \times [10.3, 294.0]$.

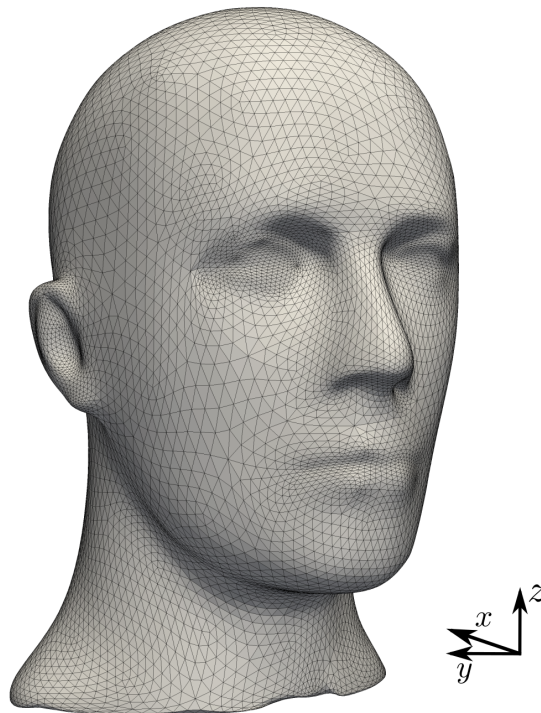


Figure 4.16: Mannequin problem: control grid with 11,330 vertices.

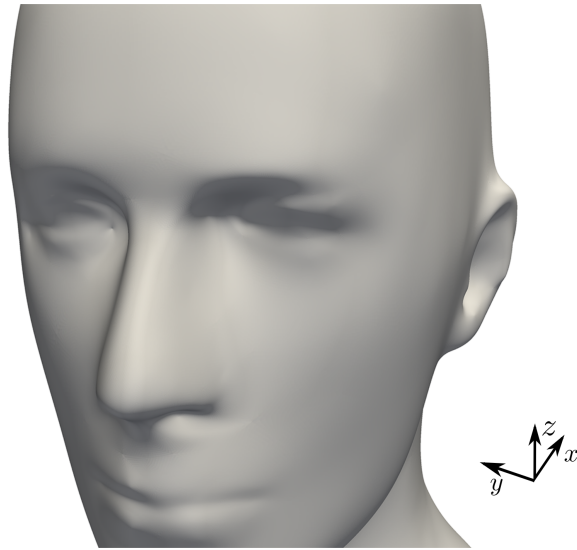
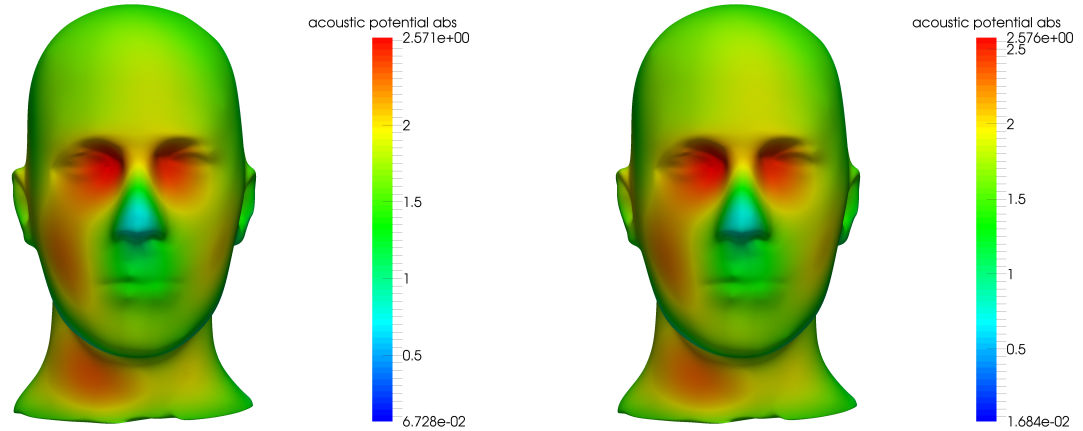


Figure 4.17: The smooth limit surface of the mannequin model generated through Loop subdivision. This limits surface is common to the control grids shown in Figures 4.15 and 4.16.

A forcing function is constructed through an incident plane wave with unit magnitude travelling in the positive x - direction with a normalised wavenumber of $\bar{k}a = 11.5$. Close inspection of the geometry reveals that the model is unsymmetric about the $x - z$ plane and hence any solution will be unsymmetric about the same plane. Profiles of acoustic pressure magnitude are illustrated in Figures 4.18a and 4.18b for the control grids with 2,834 and 11,330 vertices respectively, and a good agreement is observed. The ability to solve the present problem involving dense matrices with 11,330 vertices is only possible through the use of an \mathcal{H} -matrix approximation. Table 4.5 shows the runtimes and memory usage for assembling and storing \mathbf{H} with hierarchical matrices in both tests. The set of bounding boxes and low-rank matrix approximation used to construct our \mathcal{H} -matrix approximation for the 11,330 model are shown in Figures 4.19 and 4.20 respectively.



(a) Acoustic pressure magnitude: 2,834 vertices. (b) Acoustic pressure magnitude: 11,330 vertices.

Figure 4.18: Mannequin problem: acoustic pressure profiles for the two considered Loop subdivision discretisations.

Table 4.5: Runtime and memory usage for assembling and storing matrix \mathbf{H} using hierarchical matrices in two mannequin model tests

number of vertices	2834	11330
runtime for assembly	32min 36sec	5hr 1min 40sec
memory usage for storage	1.17GB	2.65GB

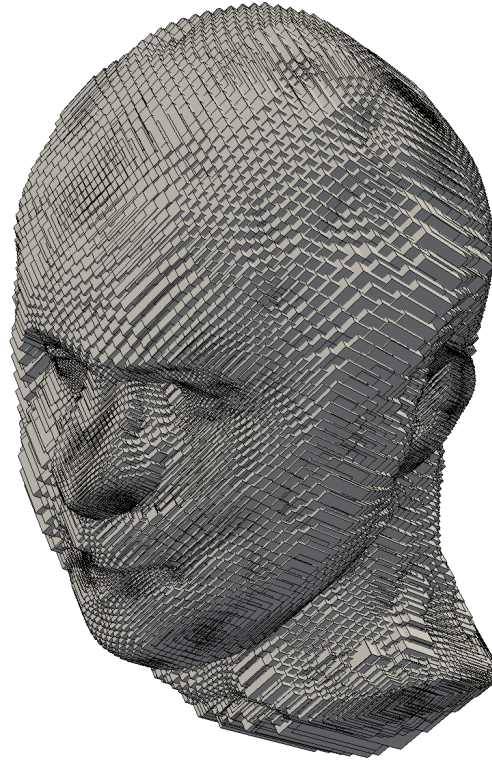


Figure 4.19: The set of bounding boxes used to define the block cluster tree for \mathcal{H} -matrix construction of the dense matrices (11,330 vertices).

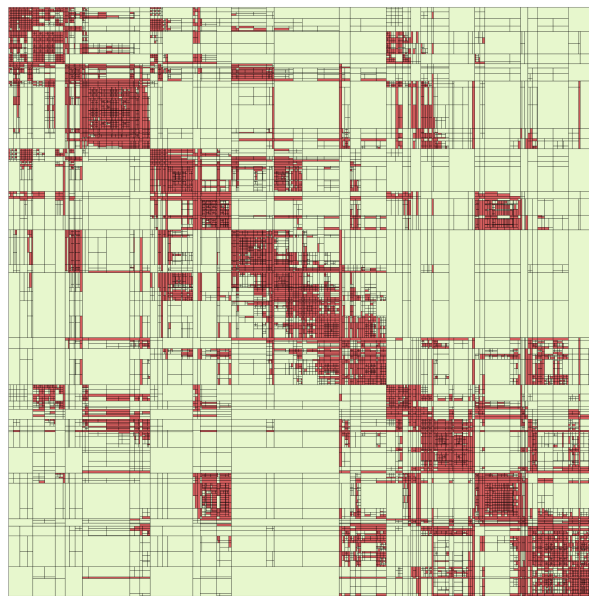


Figure 4.20: The low-rank approximation of the dense matrix \mathbf{H} for the control grid with 11,330 vertices. Dense and sparse entries are denoted by red and green respectively.

Chapter 5

A coupled isogeometric boundary element and finite element method for two-way structural-acoustic coupling analysis using subdivision surfaces

This chapter presented a novel method which coupled a collocation boundary element formulation and a Galerkin Kirchhoff-Love shell finite element formulation using the same Loop subdivision discretisation for structural-acoustic analysis. The work was presented in [136]. The Kirchhoff-Love shell formulation with Loop subdivision surfaces is presented in [5] and will be reviewed in Section 5.1. Section 5.2 presented the coupled structural-acoustic formulation. The implementation is verified by the examples that plane wave scattered by elastic spherical shells. Complex geometries are then presented to demonstrate the abilities of this method to solving practical problems.

5.1 Shell structural dynamic analysis using Kirchhoff-Love theory

In a number of applications of acoustic studies, the mechanical models of the underwater objects can be considered as shell structures. The Kirchhoff-Love shell theory simplifies a three-dimensional structure into a two dimensional surface with an uniform thickness. Using simplified model, one can determine the dynamic response of the shell subject to an acoustic wave. There are two widely-used shell theories, which are classified according to the ratio between thickness and the radius of curvature of the shell. The Kirchhoff-Love shell theory describes thin shells. The Reissner-Mindlin shell theory extends the Kirchhoff-Love theory with shear deformations and can be applied to both thin and thick shells. The Kirchhoff-Love theory requires C^1 continuity of the geometry discretisation where the Reissner-Mindlin theory only requires C^0 continuity. The conventional FEM was introduced with Lagrange elements [137], defined using Lagrange interpolation polynomials, to discretise the geometry. The discretisation only provides C^0 continuity between elements, so that the conventional finite element implementations prefer the Reissner-Mindlin shell formulation. However, the Reissner-Mindlin shell have three additional rotation degrees of freedom, which significantly increase the computational efforts to formulate the system of equations. Subdivision discretisation can provide at C^1 continuity all over the surfaces. Thus it provides the possibility to model the mechanical response of shells using Kirchhoff-Love theory. The detailed theory can be found in Simo and Fox [138] and [139–141].

Figure 5.1 illustrates the kinematic definition of a thin shell. The Kirchhoff-Love theory implemented in this work is confined to linear theory of shells under time-harmonic loads. The weak form of the equilibrium equations of thin-shells is used to formulate the finite element method. Assume a elastic shell with a mid-surface Γ and uniform thickness h . The virtual work expression for the shell with displacements \mathbf{u} expresses as:

$$W_{\text{mas}}(\mathbf{u}, \bar{\mathbf{u}}) + W_{\text{int}}(\mathbf{u}, \bar{\mathbf{u}}) + W_{\text{ext}}(\bar{\mathbf{u}}) = 0, \quad (5.1)$$

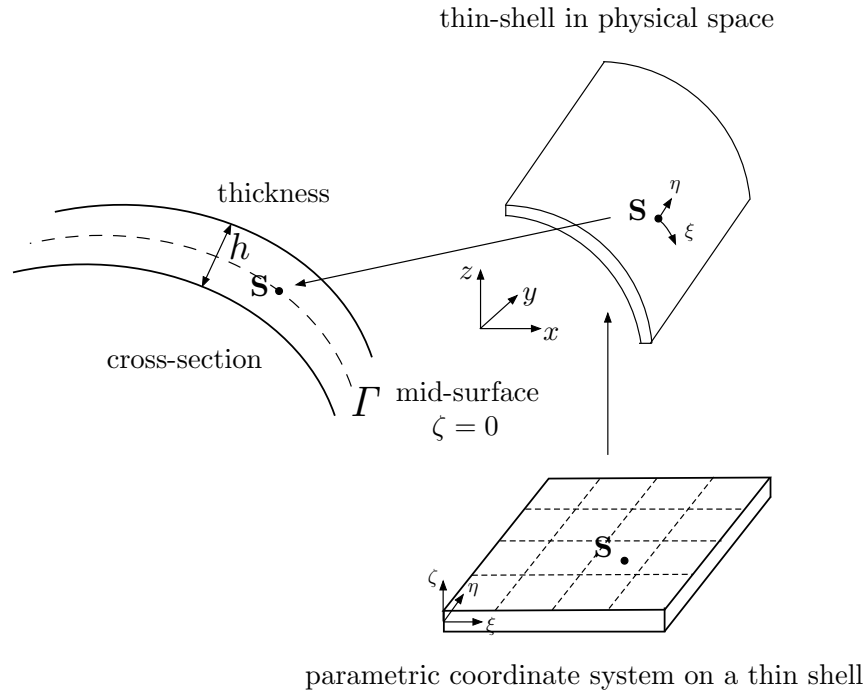


Figure 5.1: An example thin shell illustrates the definitions of thickness, mid-surface and the parametric coordinate system.

where $\bar{\mathbf{u}}$ is the virtual displacement. The three terms $W_{\text{mas}}(\mathbf{u}, \bar{\mathbf{u}})$, $W_{\text{int}}(\mathbf{u}, \bar{\mathbf{u}})$ and $W_{\text{ext}}(\bar{\mathbf{u}})$ denote the virtual work contributions of the inertia, internal and external forces, respectively. The detailed presentation of the equilibrium equations of elastic shells can be found in [5, 32, 142]. For a thin-shell with a density ρ_s the inertia contribution is given by

$$W_{\text{mas}}(\mathbf{u}, \bar{\mathbf{u}}) = \int_{\Gamma} \rho_s \frac{\partial^2 \mathbf{u}}{\partial t^2} \cdot \bar{\mathbf{u}} \mu \, d\Gamma$$

where μ is a Jacobian term taking care of integration across the thickness of the shell. A Kirchhoff-Love shell theory only considers the acceleration of the mid-surface. The contribution of the angular acceleration associated with the shell's mid-surface normal has been neglected. The mid-surface displacements \mathbf{u} are assumed to be time harmonic so that applying a Fourier transformation to the weak form (5.1) leads to its time-harmonic form, given by

$$W_{\text{mas}}(\mathbf{u}, \bar{\mathbf{u}}) = -\omega^2 \int_{\Gamma} \rho_s \mathbf{u} \cdot \bar{\mathbf{u}} \mu \, d\Gamma,$$

where ω denotes the angular frequency. The internal work $W_{int}(\mathbf{u}, \bar{\mathbf{u}})$ consists of two parts:

$$W_{int}(\mathbf{u}, \bar{\mathbf{u}}) = \int_{\Gamma} \boldsymbol{\alpha}(\mathbf{u}) : \mathbf{E} : \boldsymbol{\alpha}(\bar{\mathbf{u}}) \mu \, d\Gamma + \frac{h^2}{12} \int_{\Gamma} \boldsymbol{\beta}(\mathbf{u}) : \mathbf{E} : \boldsymbol{\beta}(\bar{\mathbf{u}}) \mu \, d\Gamma.$$

The first integral is the membrane part. The membrane integral depends on the fourth order constitutive tensor \mathbf{E} and the change of the metric tensor $\boldsymbol{\alpha}(\mathbf{u})$ of the mid-surface between the reference and deformed configurations of the shell shown in Figure 5.2. The components in \mathbf{E} are defined as

$$\mathbf{E}^{ijkl} = \frac{1}{2} \frac{Eh}{1 - \nu^2} \left(\nu \bar{a}^{ij} \bar{a}^{kl} + \frac{1}{2} (1 - \nu) (\bar{a}^{ik} \bar{a}^{jl} + \bar{a}^{il} \bar{a}^{jk}) \right),$$

where E is Young's modulus, ν is Poisson's ratio, and \bar{a}^{ij} is the contravariant components of the undeformed surface metric tensors. The components in $\boldsymbol{\alpha}$ are defined as

$$\alpha_{ij} = \frac{1}{2} (\bar{\mathbf{a}}_i \cdot \mathbf{u}_{,j} + \bar{\mathbf{u}}_{,i} \cdot \bar{\mathbf{a}}_j).$$

The second integral representing the bending part is multiplied with the square of the shell thickness h and depends on change of curvature tensor $\boldsymbol{\beta}(\mathbf{u})$ between the reference and deformed configurations. The components in $\boldsymbol{\beta}$ are defined as

$$\begin{aligned} \beta_{ij} = & -\mathbf{u}_{,ij} \cdot \bar{\mathbf{a}}_3 + \frac{1}{\sqrt{\bar{a}}} (\mathbf{u}_{,1} \cdot (\bar{\mathbf{a}}_{i,j} \times \bar{\mathbf{a}}_2) + \mathbf{u}_{,2} \cdot (\bar{\mathbf{a}}_1 \times \bar{\mathbf{a}}_{i,j})) \\ & + \frac{\bar{\mathbf{a}}_3 \cdot \bar{\mathbf{a}}_{i,j}}{\sqrt{\bar{a}}} (\mathbf{u}_{,1} \cdot (\bar{\mathbf{a}}_2 \times \bar{\mathbf{a}}_3) + \mathbf{u}_{,2} \cdot (\bar{\mathbf{a}}_3 \times \bar{\mathbf{a}}_1)), \end{aligned}$$

where $\sqrt{\bar{a}}$ is the Jacobian of the surface coordinates. The detailed definitions can also be found in [5]. The external virtual work for a pressure p on the mid-surface is given by

$$W_{ext}(\bar{\mathbf{u}}) = - \int_{\Gamma} p \mathbf{n}_S \cdot \bar{\mathbf{u}} \, d\Gamma$$

where \mathbf{n}_S denotes the normal vector at the mid-surface point.

Similar with boundary element method, the Loop subdivision basis functions $\mathbf{N}(\xi, \eta)$ are

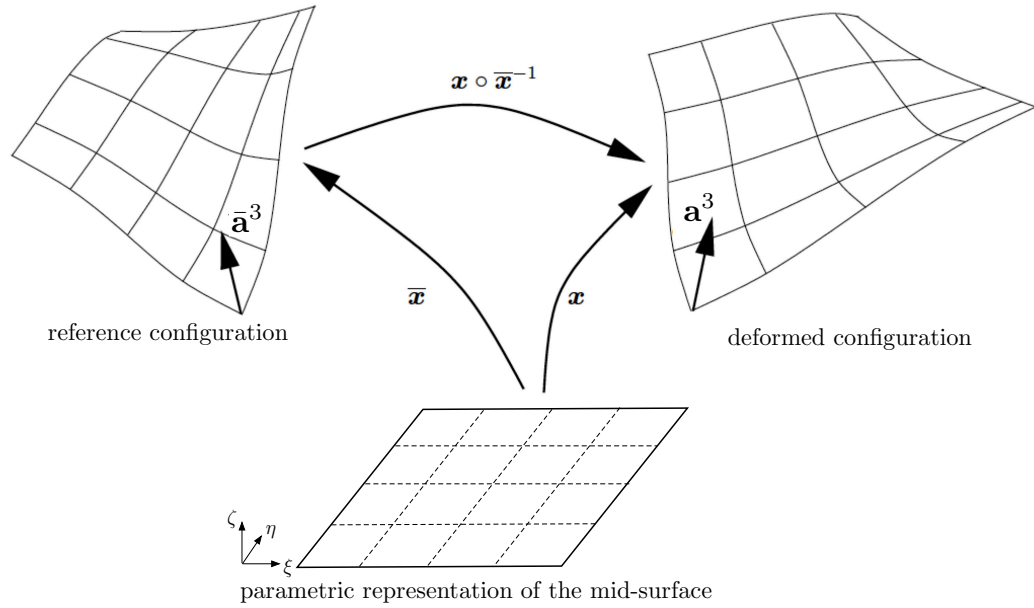


Figure 5.2: Reference and deformed configuration of the shell. $\bar{\mathbf{x}}$ and \mathbf{x} are two mapping operators map the parametric representation of the mid-surface to its reference and deformed configurations. Figure reproduced from [5].

used to discretise the displacements \mathbf{u} and the test functions (virtual displacements) \mathbf{v} in each element:

$$\mathbf{u}^e(\xi, \eta) = \sum_{k=1}^m N_k(\xi, \eta) \mathbf{u}_k^e \quad \text{and} \quad \bar{\mathbf{u}}^e(\xi, \eta) = \sum_{k=1}^m N_k(\xi, \eta) \bar{\mathbf{u}}_k^e,$$

where the \mathbf{u}_k^e and $\bar{\mathbf{u}}_k^e$ are nodal values. The integrals are evaluated with Gauss quadrature. After linearisation, the system of equations that governs the time-harmonic behaviour of the displacements is expressed as

$$\underbrace{(-\omega^2 \mathbf{M} + \mathbf{K})}_{\mathbf{A}} \mathbf{u} = \mathbf{f}, \quad (5.2)$$

where \mathbf{K} is the stiffness matrix, \mathbf{M} denotes the mass matrix and \mathbf{f} is the global force vector. The explicit expressions of the stiffness matrix and the implementation details can be found in [5]. The FE system matrix is denoted as \mathbf{A} .

5.2 Coupled structural-acoustic formulation

An isogeometric boundary element method was introduced in Chapter 4 to analyse acoustic scattering problems in the exterior fluid domain. There, the objects were considered as acoustically hard obstacles, which means they are perfectly rigid and reflect all acoustic waves. The derivatives of acoustic pressures with respect to normal vector (acoustic pressure normal derivatives) retain zero on the surfaces. However, if an incident acoustic wave impinges a thin-shell structure, it will introduce a surface force to the shell structure and the shell will vibrate with the associated the structural nodal velocities on the shell surfaces. The phenomena also can be understood as the shell absorbs a part of the incident wave, which introduces acoustic pressure normal derivatives on the surfaces. A formulation is introduced in this section to analyse the coupled structural-acoustic problem using the finite element method to analyse the structural dynamic behaviours and boundary element method to solve the acoustic scattering problem. It considers the acoustic pressures as a structural forces on the surface and also links the structural nodal velocities with the acoustic pressure normal derivatives on the surfaces. The structural domain and acoustic domain are defined in Figure 5.3.

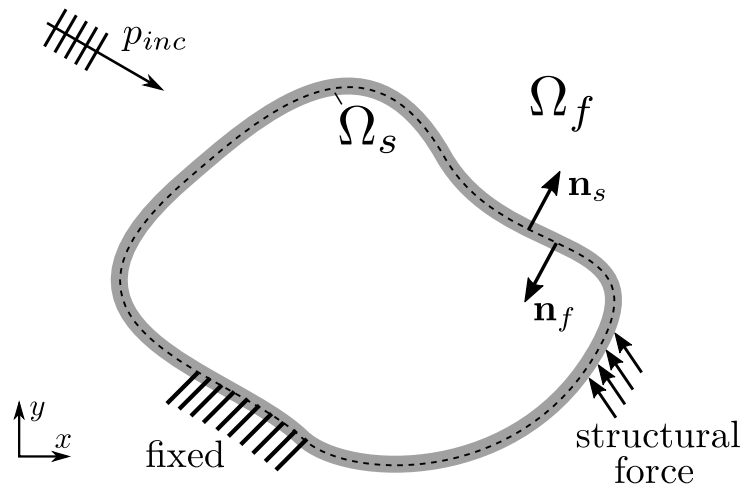


Figure 5.3: Definition of the structural thin shell and fluid domains for the coupled structural-acoustic problem impinged by an incident plane wave p_{inc} . The mid-surface of the shell is denoted by a dashed line. The structural domain normal vectors \mathbf{n}_s and the fluid domain normal vector \mathbf{n}_f are pointing opposite directions.

The acoustic pressure in the fluid domain can be treated as a force on the shell surface, which

is directed along the surface normal \mathbf{n}_f . The shell nodal forces vector \mathbf{f} in Equation 5.2 consist of structural force \mathbf{f}_s and fluid force \mathbf{f}_f :

$$\mathbf{f} = \mathbf{f}_s + \mathbf{f}_f. \quad (5.3)$$

The fluid force due to an acoustic pressure field is given by:

$$\mathbf{f}_f = \underbrace{\tilde{\mathbf{n}}_f \int_{\Gamma} \mathbf{N}^T \mathbf{N} d\Gamma}_{\mathbf{C}_{sf}} \mathbf{p}, \quad (5.4)$$

where \mathbf{N} is the global vector of subdivision basis functions and \mathbf{p} denotes the global vector of nodal acoustic pressure coefficients. The matrix of vertex normals $\tilde{\mathbf{n}}_f$ is defined as:

$$\tilde{\mathbf{n}}_f = \begin{bmatrix} \mathbf{n}_{1f} \cdot \mathbf{e}_1 & 0 & \dots \\ \mathbf{n}_{1f} \cdot \mathbf{e}_2 & 0 & \dots \\ \mathbf{n}_{1f} \cdot \mathbf{e}_3 & 0 & \dots \\ 0 & \mathbf{n}_{2f} \cdot \mathbf{e}_1 & \dots \\ 0 & \mathbf{n}_{2f} \cdot \mathbf{e}_2 & \dots \\ 0 & \mathbf{n}_{2f} \cdot \mathbf{e}_3 & \dots \\ \dots & \dots & \dots \end{bmatrix}$$

where $\mathbf{e}_1, \mathbf{e}_2, \mathbf{e}_3$ are the three orthogonal normal Cartesian base vectors so that each column of $\tilde{\mathbf{n}}_f$ contains the normal at one of the n_c control vertices in the mesh. The so defined transfer matrix \mathbf{C}_{sf} of dimension $3n_c \times n_c$ transfers forces from the fluid to the shell. Then, The global force vector is expressed as:

$$\mathbf{f} = \mathbf{C}_{sf} \mathbf{p} + \mathbf{f}_s. \quad (5.5)$$

Now, we consider the relationship between acoustic pressure and shell mid-surface velocities. The normal components of the fluid and structural velocities are denoted as v_f^n and v_s^n respectively. If there is no energy loss between the structural domain and fluid domain, the

two normal velocities can be related through:

$$v_f^n - v_s^n = 0. \quad (5.6)$$

The acoustic pressure normal derivatives at a surface point is related to the fluid normal velocity v_f^n as

$$\frac{\partial p}{\partial n} = -i\omega\rho_f v_f^n, \quad (5.7)$$

where ρ_f is the density of fluid. The structural normal velocity v_s^n is related to the nodal displacements \mathbf{u} through:

$$v_s^n = i\omega\mathbf{n}_f \cdot \mathbf{u}. \quad (5.8)$$

Substituting Equations 5.7 and 5.8 into 5.6 for v_f^n and v_s^n respectively, the relationship between acoustic pressure normal derivative and structural displacement at a surface point is expressed as:

$$\frac{\partial p}{\partial n} = \omega^2\rho_f\mathbf{n}_f \cdot \mathbf{u}.$$

With this relationship, the global vectors can be related as

$$\mathbf{q} = \omega^2\rho_f\mathbf{C}_{fs}\mathbf{u}, \quad (5.9)$$

where $\mathbf{C}_{fs} = \tilde{\mathbf{n}}_f^T$ and \mathbf{u} is the global vector of nodal displacements. Using Equation 5.9 to substitute for \mathbf{q} in the boundary element system of equations (4.27), a coupled system for the acoustic problem is given by

$$\mathbf{H}\mathbf{p} = \mathbf{G}\omega^2\rho_f\mathbf{C}_{fs}\mathbf{u} + \mathbf{p}_{inc}. \quad (5.10)$$

Substitute Equation 5.5 into Equation 5.2, a coupled system of equations for the structural dynamics problem is expressed as

$$\mathbf{A}\mathbf{u} = \mathbf{C}_{sf}\mathbf{p} + \mathbf{f}_s. \quad (5.11)$$

Finally, by combining Equation 5.10 and Equation 5.11, the global coupled system of equations

is expressed as

$$\begin{bmatrix} \mathbf{A} & -\mathbf{C}_{sf} \\ -\omega^2 \rho \mathbf{G} \mathbf{C}_{fs} & \mathbf{H} \end{bmatrix} \begin{bmatrix} \mathbf{u} \\ \mathbf{p} \end{bmatrix} = \begin{bmatrix} \mathbf{f}_s \\ \mathbf{p}_{inc} \end{bmatrix}. \quad (5.12)$$

Given the structural nodal shell forces and the incident acoustic pressures on the right-hand side of the system of equations as Neumann boundary conditions, the two global vectors of the nodal displacements and acoustic pressure coefficients can be solved. However, in the large matrix, the finite element method matrix \mathbf{A} is a sparse matrix but the entries in boundary element method matrices \mathbf{H} and \mathbf{G} are fully populated. The matrix is also non-symmetric. Solving this system of equation using a direct solver will lead to long runtimes and the computations will consume significant memory. In order to solve the problem efficiently, first solve the inverse of matrix \mathbf{A} and use it to express displacements \mathbf{u} :

$$\mathbf{u} = \mathbf{A}^{-1}(\mathbf{f}_s + \mathbf{C}_{sf}\mathbf{p}). \quad (5.13)$$

Then substitute Equation 5.13 into system of equation 5.10. The new coupled system of equations for acoustic analysis is expressed as

$$\mathbf{H}\mathbf{p} = \omega^2 \rho \mathbf{G} \mathbf{C}_{fs} \mathbf{A}^{-1} (\mathbf{f}_s + \mathbf{C}_{sf}\mathbf{p}) + \mathbf{p}_{inc}. \quad (5.14)$$

Defining the vector \mathbf{q}_s which accounts for the contribution of acoustic velocities from the structural domain as

$$\mathbf{q}_s = \omega^2 \rho \mathbf{C}_{fs} \mathbf{A}^{-1} \mathbf{f}_s,$$

and a global admittance matrix \mathbf{Y}_C that represents the admittance effect caused by the structure as

$$\mathbf{Y}_C = \omega^2 \rho \mathbf{C}_{fs} \mathbf{A}^{-1} \mathbf{C}_{sf}.$$

The system of equations of Equation 5.14 is then written as

$$[\mathbf{H} - \mathbf{G}\mathbf{Y}_C]\mathbf{p} = \mathbf{G}\mathbf{q}_s + \mathbf{p}_{inc}. \quad (5.15)$$

Low-rank approximations using the theory of \mathcal{H} -matrices are computed for \mathbf{H} and \mathbf{G} . The matrix \mathbf{Y}_C is computed with an approximation of the inverse operator for \mathbf{A} through a triangular factorisation. Apply the Neumann boundary conditions at the right-hand side of this system of equations, \mathbf{p} can be solved using a GMRES iterative solver. Substitute it into Equation 5.13 and the nodal displacements are obtained.

5.3 Numerical examples

5.3.1 Plane wave scattered by an elastic spherical shell

Assume an elastic spherical shell is immersed in water. An acoustic wave is propagating from a far field point source. When the acoustic wave impinges on the elastic spherical shell, it can be seen as an incident plane wave scattered by the spherical shell. This relatively simple problem with an analytical solution is used to verify the coupled formulation and the implementation. The definition of the problem is illustrated in Figure 5.4. Figure 5.5 shows the Cartesian coordinate system and the local polar coordinate system defined in the $x - y$ plane. Table 5.1 specifies all geometry and material properties. The definition of the incident wave is same as the test in Section 4.5.1 which is expressed as:

$$p_{inc} = e^{i\bar{k}x_1}.$$

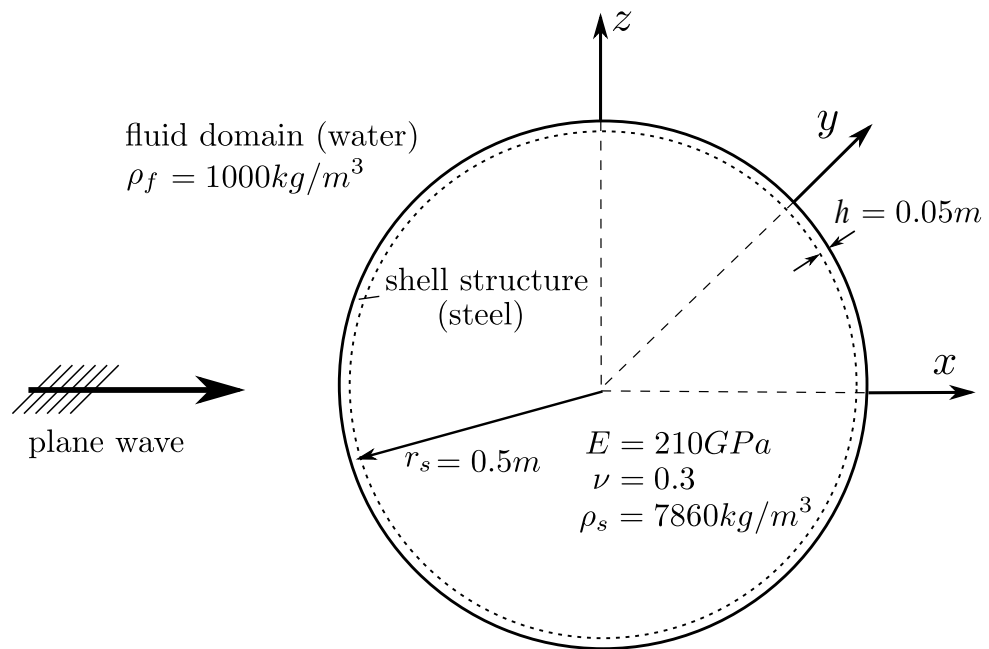


Figure 5.4: Coupled structural-acoustic problem of a plane wave impinged on a spherical shell immersed in an infinite fluid domain.

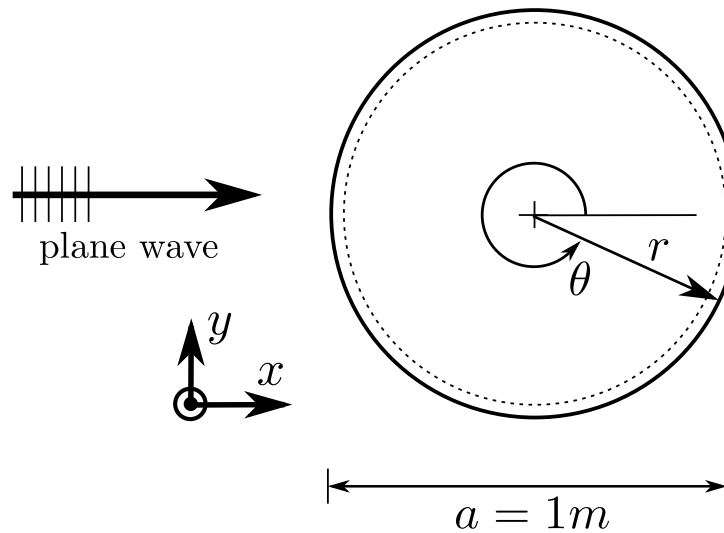


Figure 5.5: Spherical shell scattering study: incident wave direction and polar coordinate system defined in the x - y plane

Table 5.1: Default material and geometry parameters settings in the structural-acoustics problem.

Parameter name	Symbol	Value	Unit
density (water)	ρ_f	1000	kg/m^3
speed of sound(water)	c_w	1482	m/s
density (steel)	ρ_s	7860	kg/m^3
Young's modulus	E	210	GPa
Poisson's ratio	ν	0.3	-
sphere radius	r_s	0.5	m
shell thickness	h	0.05	m
plane wave magnitude	M	1	Pa

Analytical solution

The solution to this problem can be calculated analytically [12]. The total acoustic pressure $p_t \equiv p$ is consisted of the scattered and radiated acoustic components:

$$p_t = p_{scat} + p_{ela}, \quad (5.16)$$

where p_{scat} is the acoustic pressure that would result from scattering over a rigid sphere which is expressed as

$$p_{scat}(r, \theta) = p_0 \sum_{n=1}^{\infty} -\frac{i^n(2n+1)j'_n(\bar{k}r_s)}{h'_n(\bar{k}r_s)} L_n(\cos \theta) h_n(\bar{k}r), \quad (5.17)$$

and p_{ela} is the radiated acoustic pressure resulting from elastic shell vibrations. It can be expressed as

$$p_{ela}(r, \theta) = p_0 \sum_{n=1}^{\infty} \frac{i^n(2n+1)\rho_f c_w}{(Z_n + z_n)[\bar{k}r_s h'_n(\bar{k}r_s)]^2} L_n(\cos \theta) h_n(\bar{k}r), \quad (5.18)$$

where $p_0 \equiv M$ is the magnitude of the incident wave. L_n is the n th Legendre function. h_n and h'_n are the n th Hankel function and its derivative respectively. j'_n is the derivative of the n th spherical Bessel function. Z_n denotes the *invacuo* modal impedance of the spherical shell

calculated as:

$$Z_n = -\frac{i\rho_s c_p}{\Omega} \frac{h}{r_s} \frac{[\Omega^2 - (\Omega_n^{(1)})^2][\Omega^2 - (\Omega_n^{(2)})^2]}{[\Omega^2 - (1 + \beta^2)(\nu + \lambda_n - 1)]},$$

where $\lambda_n = n(n + 1)$, $\Omega = \omega \frac{r_s}{c_p}$ is a dimensionless driving frequency, $\beta^2 = \frac{h^2}{12r_s^2}$, c_p is the velocity of compressional waves in the structure given by

$$c_p = \sqrt{\frac{E}{(1 - \nu^2)\rho_s}}$$

and $\Omega_n^{(1)}$ and $\Omega_n^{(2)}$ are dimensionless natural frequencies of the spherical shell determined from the two positive roots of the polynomial equation:

$$\begin{aligned} \Omega_n^4 - [1 + 3\nu + \lambda_n - \beta^2(1 - \nu - \lambda_n^2 - \nu\lambda_n)]\Omega_n^2 + (\lambda_n - 2)(1 - \nu^2) + \\ \beta^2[\lambda_n^3 - 4\lambda_n^2 + \lambda_n(5 - \nu^2) - 2(1 - \nu^2)] = 0. \end{aligned}$$

Finally, z_n is the modal specific acoustic impedance expressed as:

$$z_n = i\rho_f c_w \frac{h_n(\bar{k}r_s)}{h'_n(\bar{k}r_s)}.$$

Convergence study

The first numerical study examining the convergence characteristics of the coupled boundary element and finite element method using the analytical solution given by Equations 5.16 to 5.18. The system of equations given by Equation 5.15 is constructed using the Loop subdivision discretisation procedure. We adopted the similar idea in Section 4.5.1 and chose the consistent normalised wavenumber $\bar{k}a = 10$. Results for control meshes (a) and (b) are shown in Figure 5.6 and results for control mesh (c) and (d) are illustrated in Figure 5.7. The profiles of the results for control meshes (a) and (b) converge to a different solution because of the non-negligible geometry error illustrated in Table 4.2. Results for control mesh (c) and (d) converged to the analytical solution which verifies the implementation of the coupled method for structural-acoustic analysis.

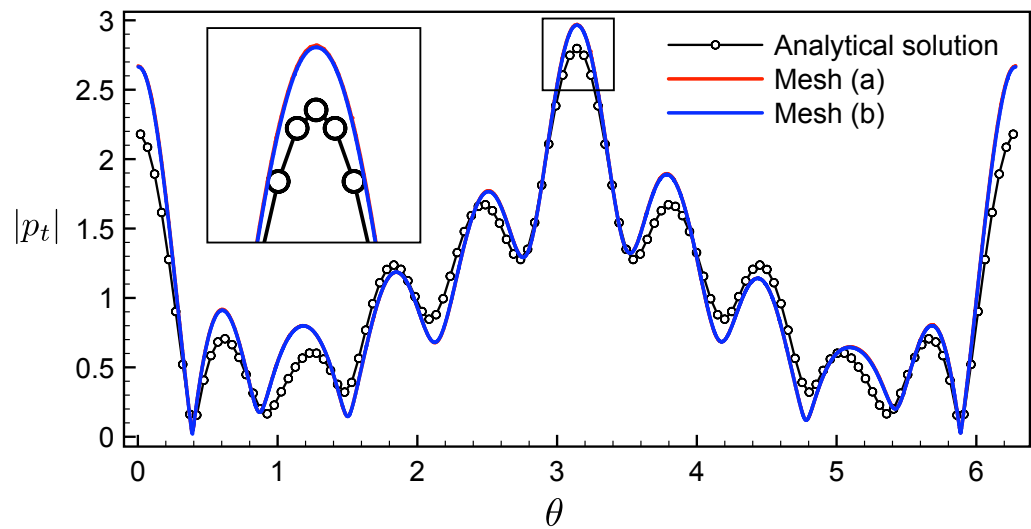


Figure 5.6: Coupled spherical shell problem, $\bar{k}a = 10$: surface acoustic potential magnitude along x - y plane using control meshes (a) and (b). The inset illustrates convergence to a solution which does not correspond to the analytical solution due to the non-negligible geometrical error of the limit surface.

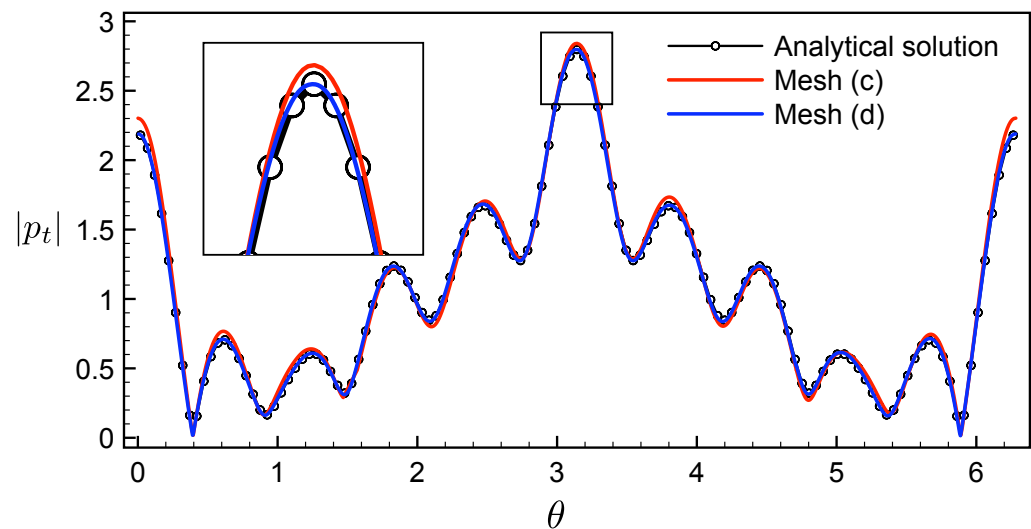


Figure 5.7: Coupled spherical shell problem, $\bar{k}a = 10$: surface acoustic potential magnitude along x - y plane using control meshes (c) and (d). L_2 projection of control vertices onto the analytical sphere surface leads to a reduced geometrical error in the limit surface and convergence to the analytical solution.

Coupling effect study

After the verification of the coupled formulation, this section will demonstrate the coupling effect caused by the dynamic response of the shell structure. We conduct three tests using the same Loop subdivision surface discretisation generated by the initial mesh shown in Figure 4.9. The first analysis is an acoustically hard sphere scattered an acoustic plane wave using the method specified in Section 4.5.1. The result is used as reference to compare with the other two tests of elastic spherical shells with thickness $h = 0.1m$ and $h = 0.05m$ respectively scatter the same acoustic plane wave. A wavenumber of $\bar{k}a = 6$ was chosen in these tests in order to keep consistent with the acoustic scattering study in [87]. The initial control mesh is sufficient for this frequency with approximately thirteen elements per wavelength. Figures 5.8, 5.9 and 5.10 illustrate the results for these three tests, where Figures 5.8c, 5.9e and 5.10e compared the far-field acoustic potential magnitude for the hard sphere against the elastic spherical shells. The effect of the additional radiated acoustic pressure caused by shell vibrations is clearly shown. Figures 5.9c, 5.9d, 5.10c and 5.10d showed that the thinner shell subjected to the same acoustic wave has larger displacements and creates larger additional radiated acoustic pressure which dramatically change the profile of the total acoustic pressure magnitude. Figure 5.10e also shows that decrease in the shell thickness creates a region of low pressure after the elastic spherical obstacle. In addition, an inspection of Figures 5.9a, 5.9b, 5.10a and 5.10b reveals that the maximum value of $Re(p)$ shifts from the illuminating region to the shadow region when the shell thickness is reduced.

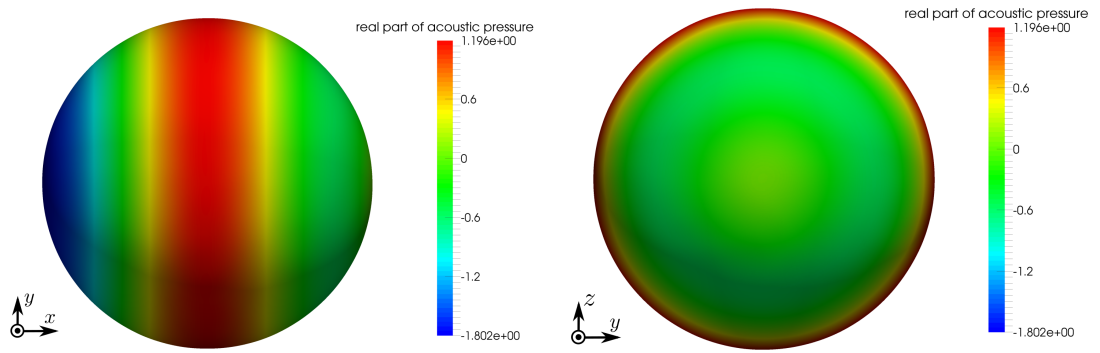
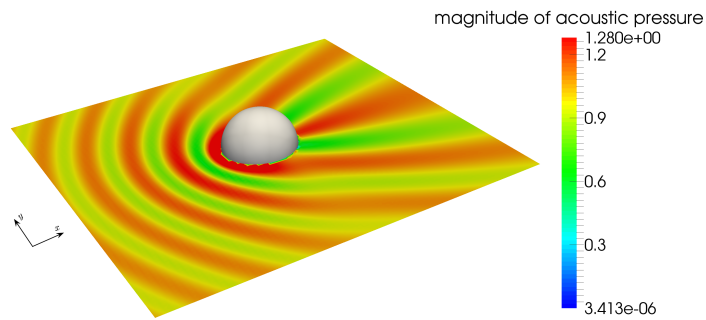
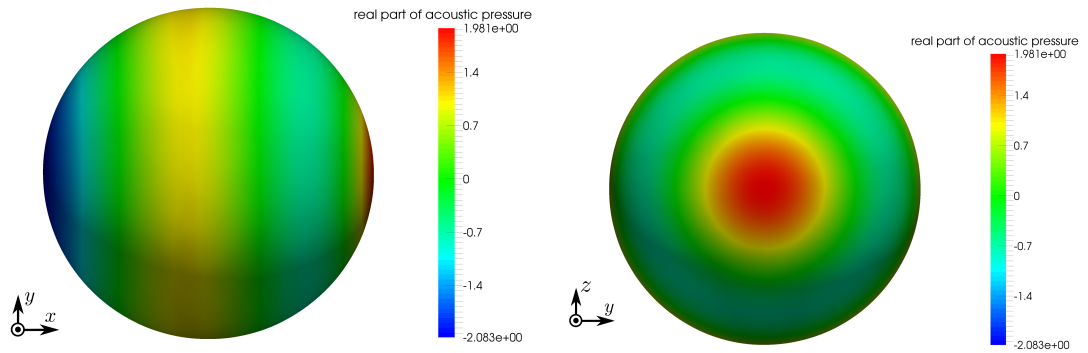
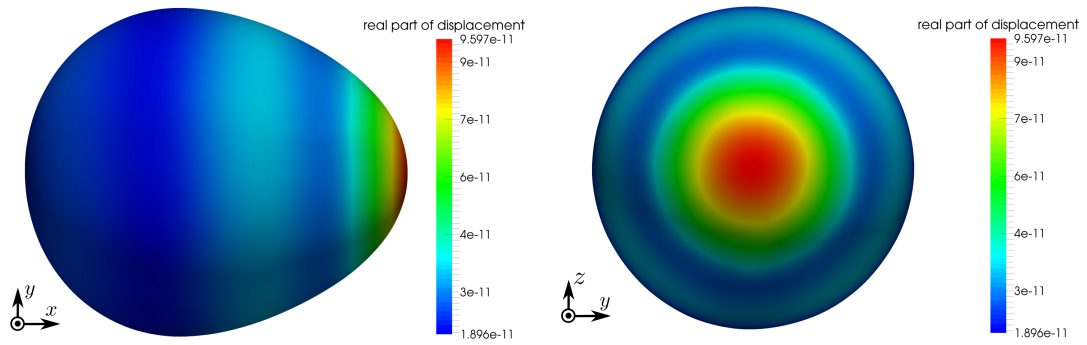
(a) $\text{Re}(p)$, x - y plane.(b) $\text{Re}(p)$, y - z plane.(c) $|p|$ on the x - y plane.

Figure 5.8: Acoustic pressure plots for the coupled sphere scattering problem with acoustically hard surface, $\bar{k}a = 6$. Shell displacements are equal to zero in this case.



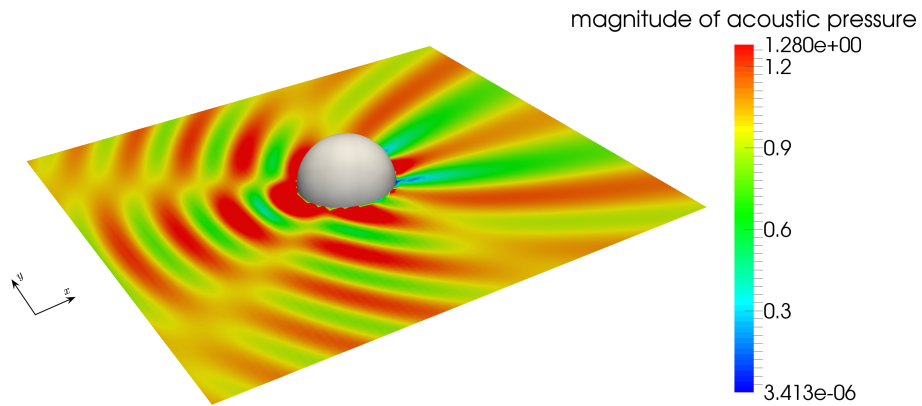
(a) $\text{Re}(p)$, x - y plane.

(b) $\text{Re}(p)$, y - z plane.



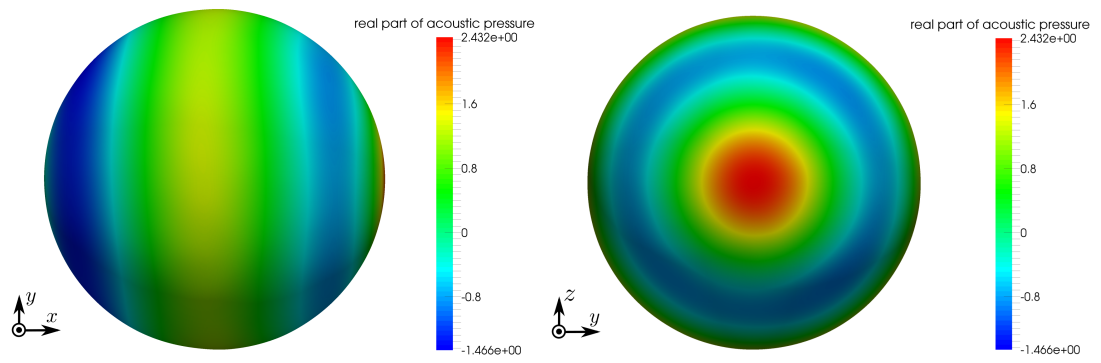
(c) $\text{Re}(\mathbf{u})$, x - y plane.

(d) $\text{Re}(\mathbf{u})$, y - z plane.



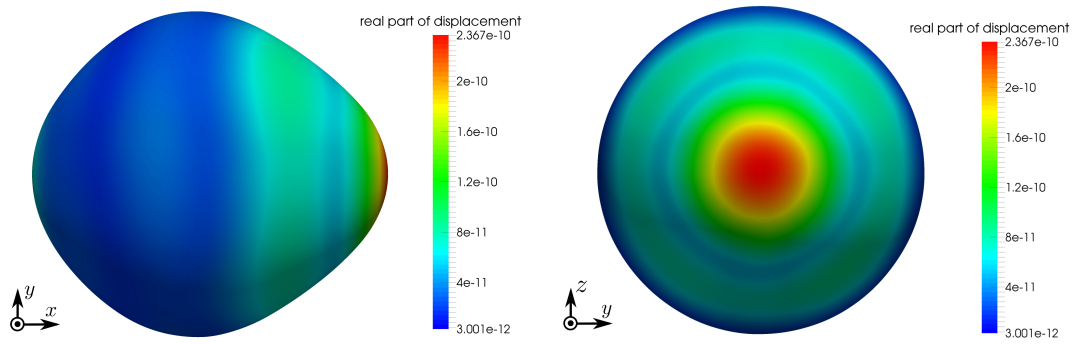
(e) $|p|$ sampled on the x - y plane.

Figure 5.9: Acoustic pressure and displacement plots for the coupled sphere scattering problem with $h = 0.1m$, $\bar{k}a = 6$. The displacements are enlarged in the figure (c) and (d).



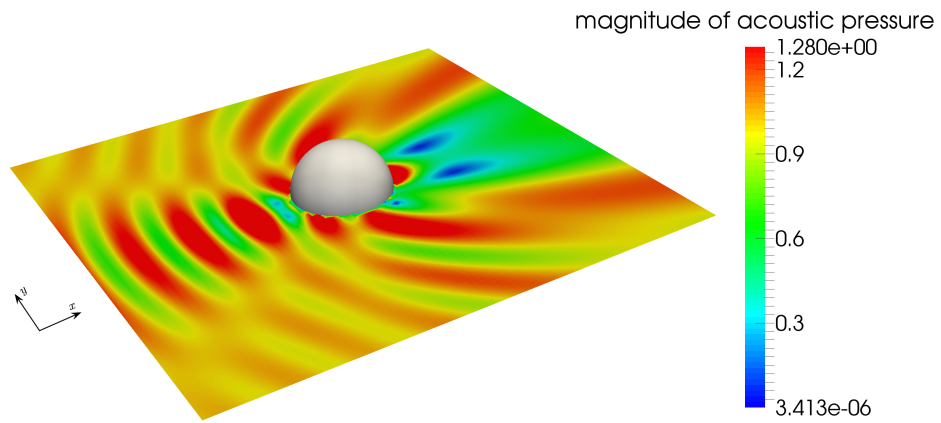
(a) $\text{Re}(p)$, x - y plane.

(b) $\text{Re}(p)$, y - z plane.



(c) $\text{Re}(\mathbf{u})$, x - y plane.

(d) $\text{Re}(\mathbf{u})$, y - z plane.



(e) $|p|$ sampled on the x - y plane.

Figure 5.10: Acoustic pressure and displacement plots for the coupled sphere scattering problem with $h = 0.05m$, $\bar{k}a = 6$. The displacements are enlarged in the figure (c) and (d).

Medium frequency problems

Section 5.3.1 verified the proposed method for problems with a relative small wavenumber ($\bar{k}a = 10$). However, simulations of higher frequency problems are more attractive for engineering applications. The boundary element method is considered as only for low frequency acoustic problems. Statistic methods [143] are mainly used for high frequency problems. However, a number of methods are developed for modelling high-frequency wave propagation, e.g. spectral boundary element method (spectral BEM) [144] and partition of unity boundary element method (PUBEM) [145]. This section will consider the ability of the method to simulate medium frequency ($ka > 20$) acoustic waves scattered by shell structures. Analysing medium to high frequency acoustic problem with the boundary element method always requires a high resolution mesh in order to approximate the fast periodic changes of acoustic pressures along the wave propagating direction. A conventional discretisation commonly use six or more elements per wavelength to analyse the problem [146], which can lead to extremely large systems of equations for complex geometries and high frequency problems. Using higher order box-spline functions as basis functions may reduce the size of the system of equations. The control meshes (c) and (d) for the sphere detailed in Table 4.3, are used to generate the Loop subdivision discretisations for the simulations. Tests with successively increasing normalised wavenumber, $\bar{k}a = 10, 30, 40, 50, 60, 80$ are conducted to determine the upper frequency limit of each discretisation. A set of sample points are defined on the sphere surface aligned with the x - y plane as $S = \{s_1, s_2, \dots, s_{n_{sample}}\}$. The maximum pointwise error in the sample set is defined by

$$\max_{\mathbf{s} \in S} \frac{||p_t^h(\mathbf{s})| - |p_t(\mathbf{s})||}{||p_t(\mathbf{s})||_{\infty}}, \quad (5.19)$$

where p_t^h and p_t represent numerical and analytical total acoustic pressures respectively. These point-wise errors for discretisations generated via control meshes (c) and (d) are shown in Table 5.2 for the different wavenumbers. The approximate number of elements per wavelength is noted in the bracket after each percentage error. Figure 5.7 compares results for both control mesh (c) and (d) to the analytical solution with a normalised wavenumber $\bar{k}a = 10$. Plots of $|p_t|$ against analytical solutions for $\bar{k}a = 30, 40$ with control mesh (c) are shown in Figures 5.11 and

5.12 respectively and for $\bar{k}a = 50, 60, 80$ with control mesh (d) in Figures 5.13, 5.14 and 5.15 respectively.

Table 5.2: Maximum pointwise errors calculated through Equation 5.19 for a set of increasing normalised wavenumbers applied to the coupled sphere problem. The numbers in parentheses indicates the approximate number of elements per wavelength. A dash indicates a result with a large maximum pointwise error that indicates insufficient resolution of mesh for the given wavenumber.

control mesh	$\bar{k}a$					
	10	30	40	50	60	80
(c)	0.0427 (16)	0.0354 (6)	0.0853 (4)	-	-	-
(d)	0.0090 (32)	0.0182 (11)	0.0194 (8)	0.0126 (7)	0.0208 (6)	0.0553 (4)

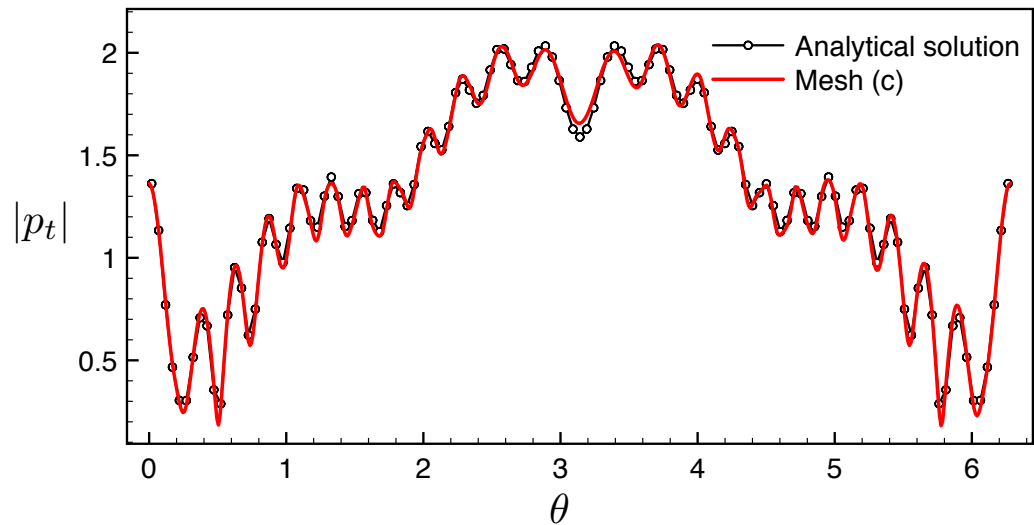


Figure 5.11: Coupled sphere study: surface acoustic potential magnitude profile along x - y plane for $\bar{k}a = 30$, control mesh (c).

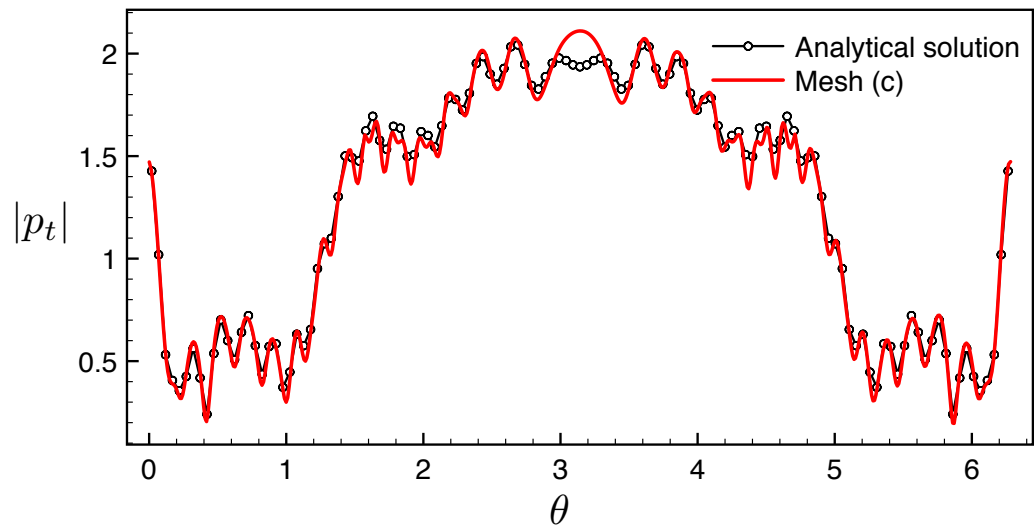


Figure 5.12: Coupled sphere study: surface acoustic potential magnitude along x - y plane for $\bar{k}a = 40$, control mesh (c).

Figure 5.11 illustrate that the numerical results profile of total acoustic pressures for control mesh (c) has a good agreement with the analytical solution when the wavenumber $\bar{k} = 30$, but a discrepancy between the analytical and numerical acoustic pressure magnitude at $\theta = \pi$ is observed which is caused by geometry error. When the wavenumber is increased to $\bar{k}a = 40$, the numerical profile can not match the analytical profile with a maximum point-wise error larger than 8.5% at $\theta = \pi$. The mesh (c) Loop subdivision surface discretisation is insufficiently fine for this frequency.

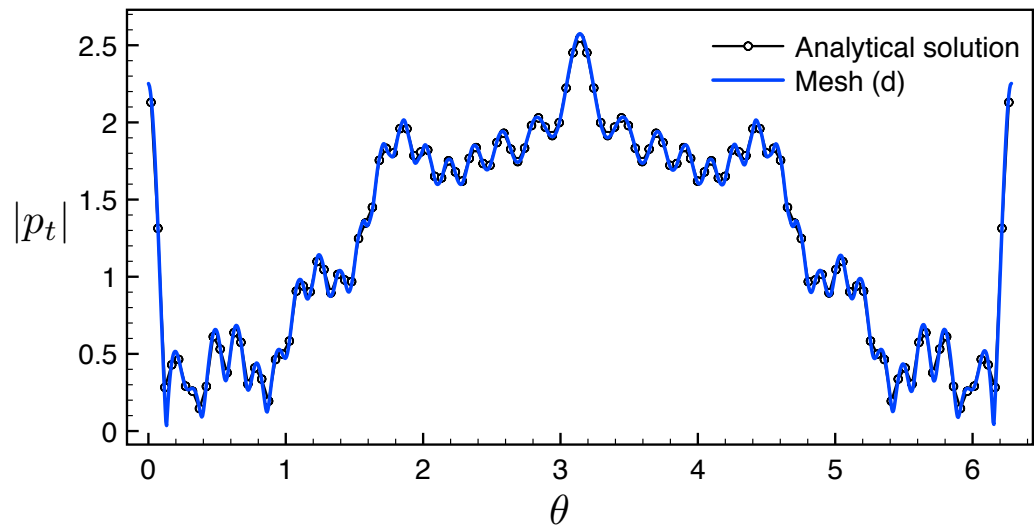


Figure 5.13: Coupled sphere study: surface acoustic potential magnitude along x - y plane for $\bar{k}a = 50$, control mesh (d).

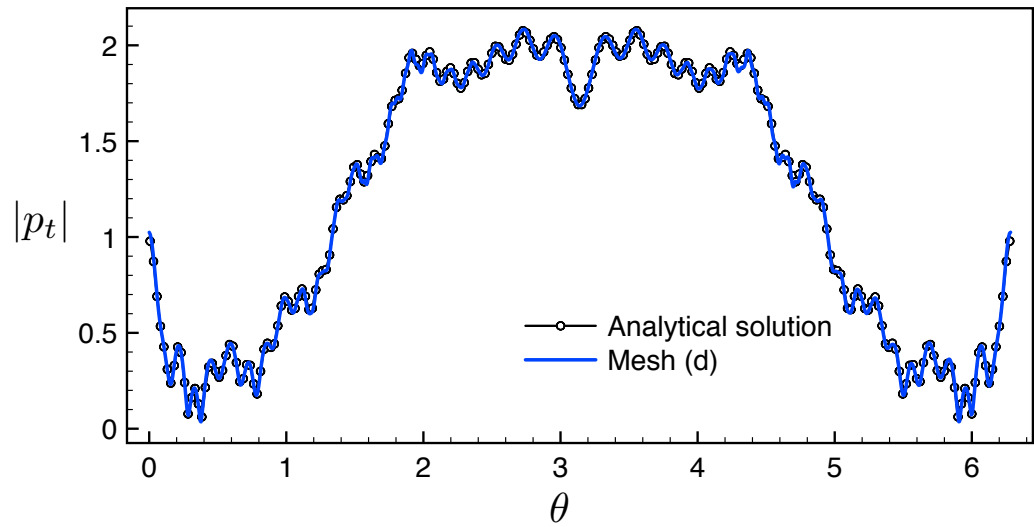


Figure 5.14: Coupled sphere study: surface acoustic potential magnitude along x - y plane for $\bar{k}a = 60$, control mesh (d).

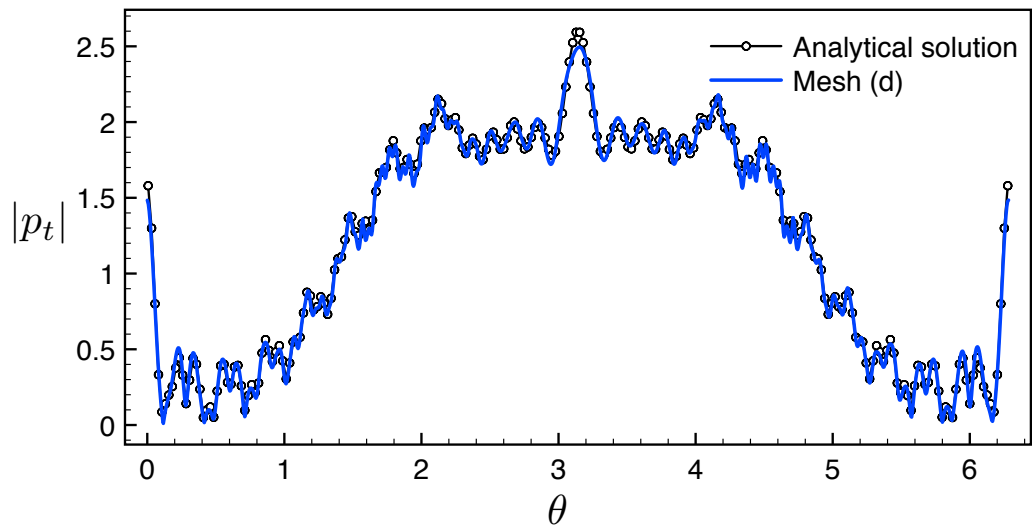


Figure 5.15: Coupled sphere study: surface acoustic potential magnitude along x - y plane for $\bar{k}a = 80$, control mesh (d).

Figures 5.13 to 5.15, for the more refined Loop subdivision surface discretisation generated through control mesh (d) are used in tests with higher wavenumber $\bar{k} = 50, 60$ and 80 , illustrate that for wavenumbers up to $\bar{k}a = 60$, the maximum point-wise error are relatively low (less than 2.1%). When the wavenumber reach a relatively high value $\bar{k}a = 80$, the maximum wavenumber for control mesh (d) is just around 5.5%. Based on the present results, a control mesh with at least six elements per wavelength is recommended when using it to construct a Loop subdivision discretisation to solve medium frequency acoustic problems.

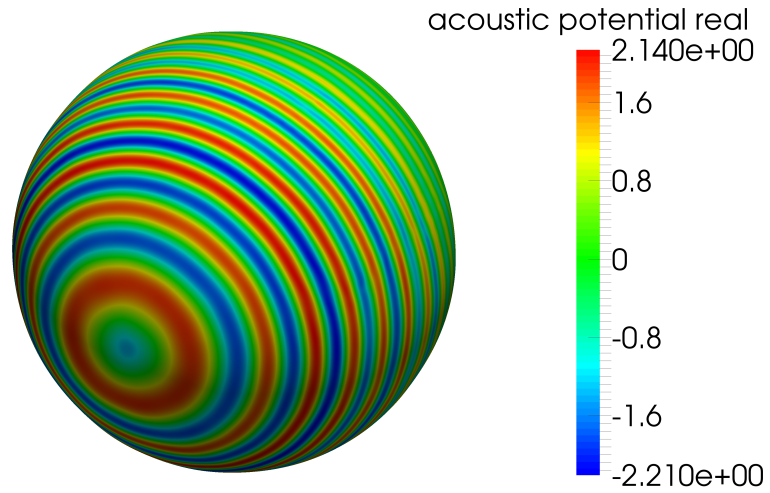


Figure 5.16: Coupled sphere study: $\text{Re}(p)$ (real component of acoustic pressure) for $\bar{k}a = 80$, control mesh (d).

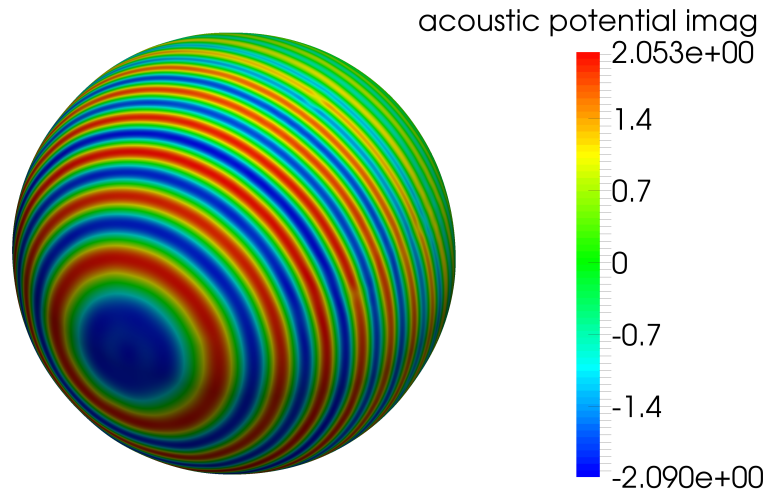


Figure 5.17: Coupled sphere study: $\text{Im}(p)$ (imaginary component of acoustic pressure) for $\bar{k}a = 80$, control mesh (d).

Figure 5.16 and 5.17 illustrates the real and imaginary parts of the total acoustic pressure on the surface on the sphere for $\bar{k}a = 80$ respectively. The previous work by Chen et al. [24] only

use low wavenumber in coupled problem. It shows the ability of using subdivision surfaces to solve structural-acoustic problems with medium frequency.

5.3.2 Acoustic wave scattered by a submarine

The second model we consider is of a submarine with a control mesh illustrated in Figure 5.18 and the limit surface of the subdivision mesh is shown in Figure 5.19. This example is mainly used to demonstrate the method's ability to process complex industrially-relevant models that utilise smooth geometry representations generated by CAD software. The minimum bounding box of this submarine model is defined by $[x_i^{min}, x_i^{max}]^3 = [-51.3, 41.0] \times [-58.4, 17.8] \times [-11.8, 11.8]$ and the model is symmetrical about the x - y plane. The material properties as specified in Table 5.1 are applied with a shell thickness of $h = 0.5m$. A forcing function is constructed through an incident plane wave with unit magnitude propagating in the negative x -direction. The normalised wavenumber for this example is $\bar{k}a = 46.15$.

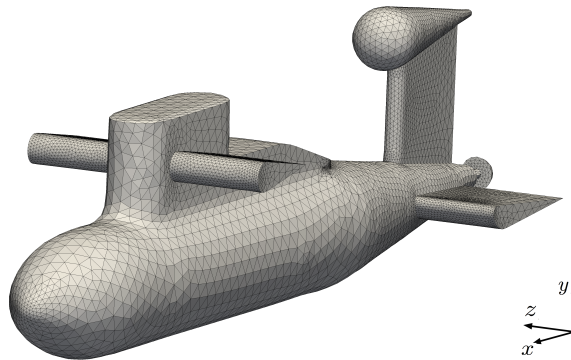


Figure 5.18: Submarine problem: control mesh with 9, 510 vertices.

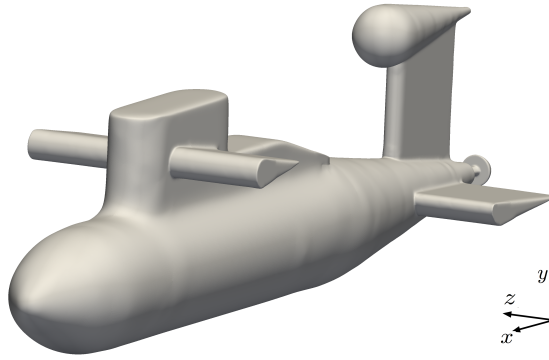
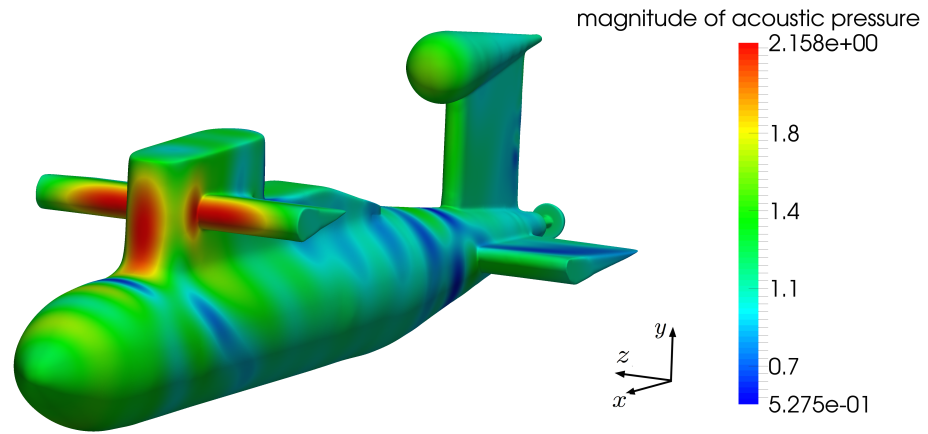
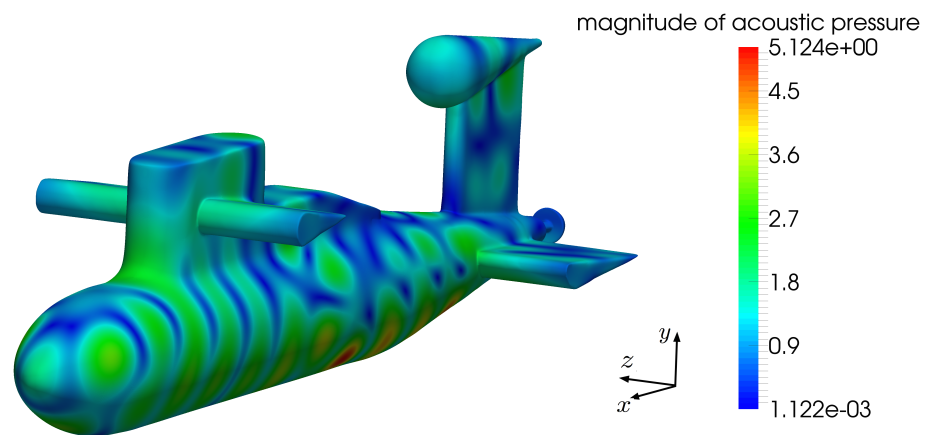


Figure 5.19: The smooth limit surface of the submarine model generated through Loop subdivision.

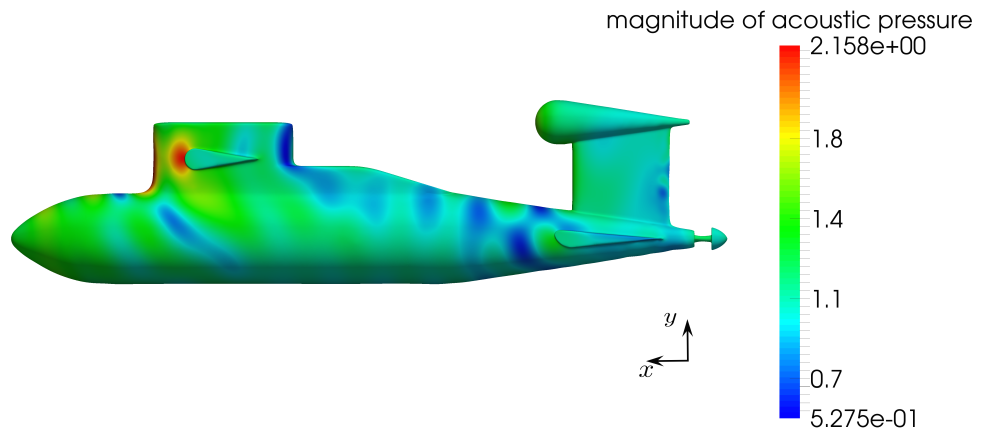


(a) Acoustically hard surface.

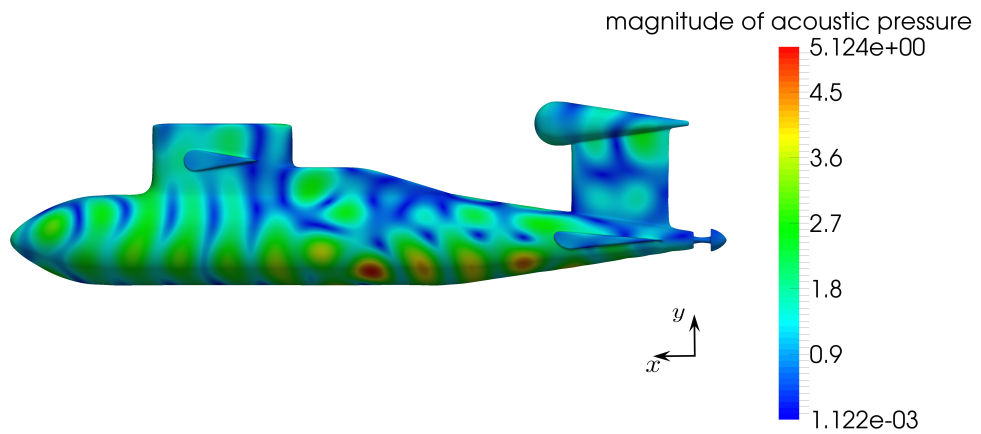


(b) Coupled elastic shell.

Figure 5.20: Submarine model: acoustic pressure magnitude profiles for both an acoustically hard surface and coupled shell formulation with a normalised wavenumber of $\bar{k}a = 46.15$, perspective view.

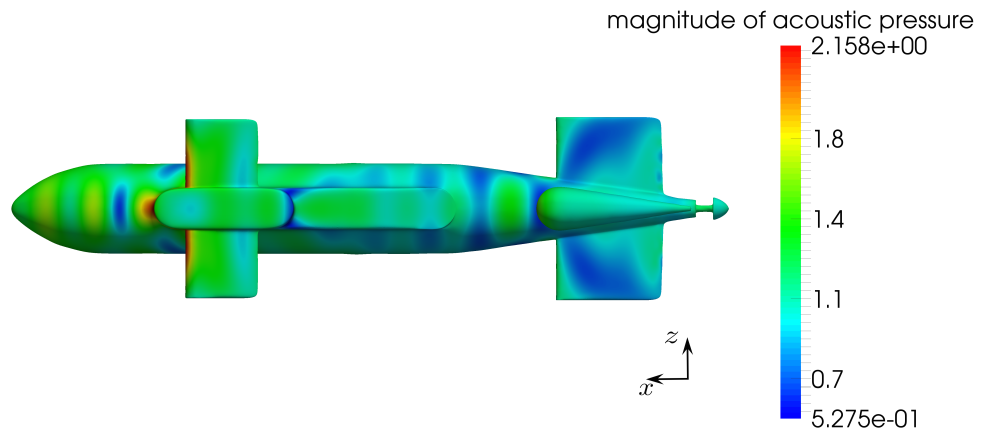


(a) Acoustically hard surface.

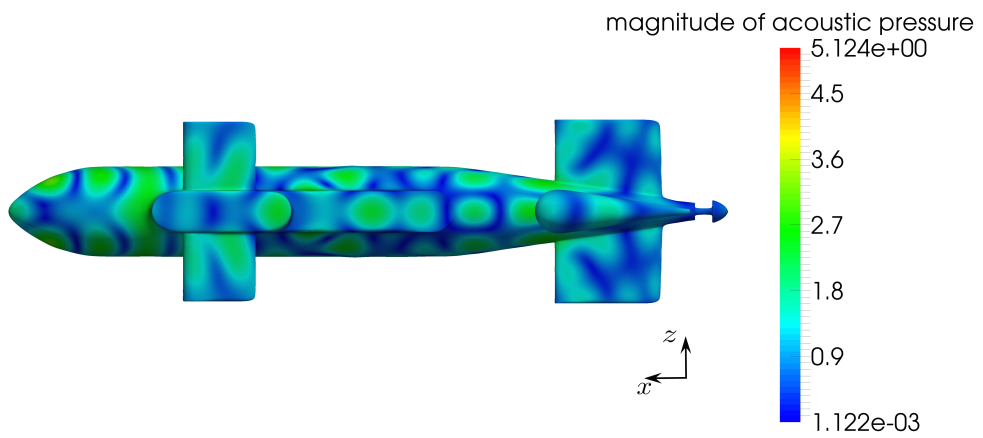


(b) Coupled elastic shell.

Figure 5.21: Submarine model: acoustic pressure magnitude profiles for both an acoustically hard surface and coupled shell formulation with a normalised wavenumber of $\bar{k}a = 46.15$, *x-y* plane.

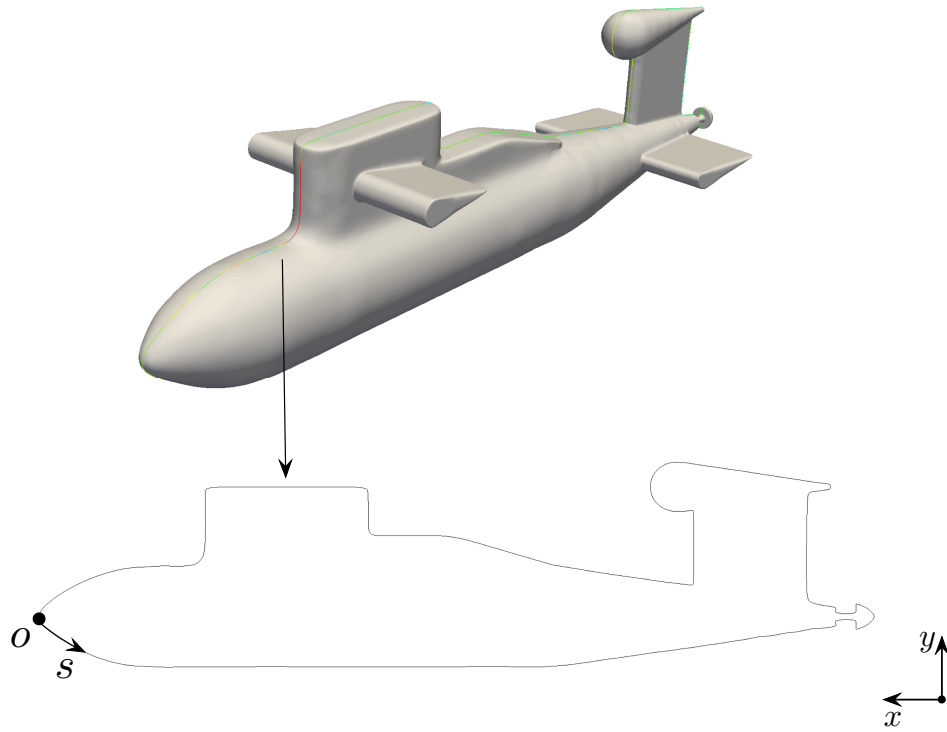
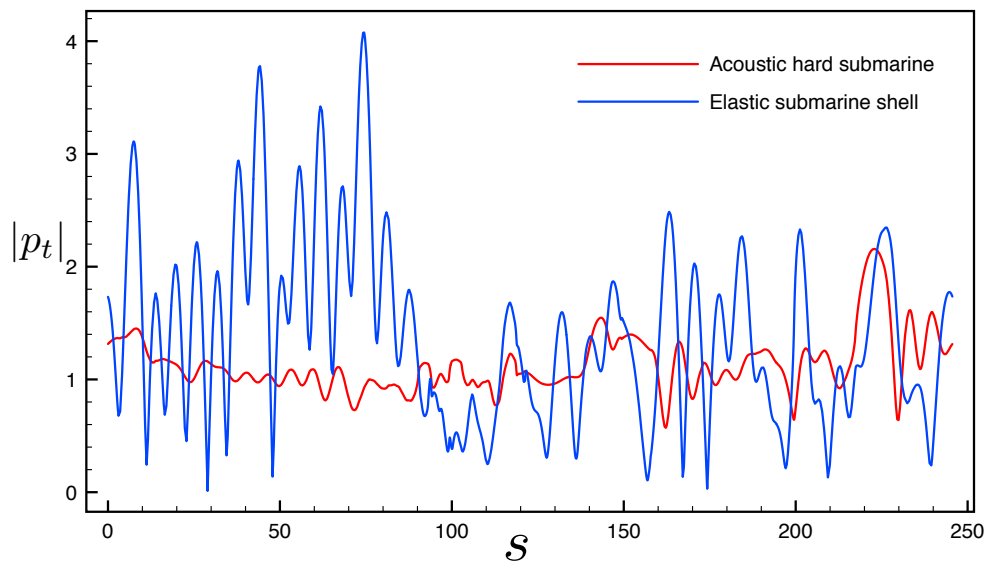


(a) Acoustically hard surface.



(b) Coupled elastic shell.

Figure 5.22: Submarine model: acoustic pressure magnitude profiles for both an acoustically hard surface and coupled shell formulation with a normalised wavenumber of $\bar{k}a = 46.15$, x - z plane.

(a) A x - y slice of the submarine.

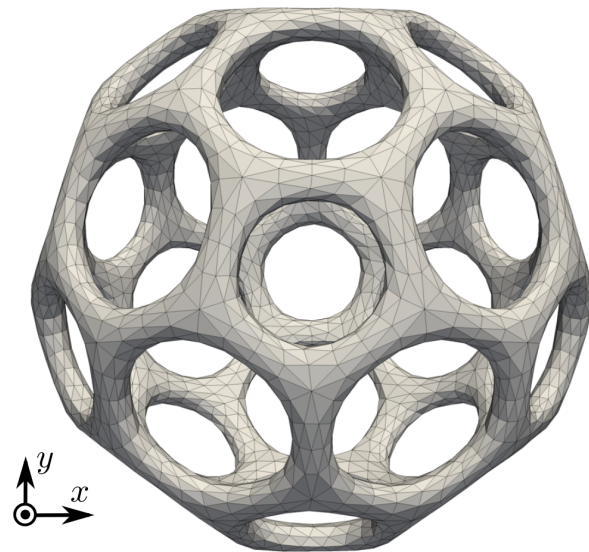
(b) Acoustic pressure magnitude profiles along the sliced curve.

Figure 5.23: Submarine model: acoustic pressure magnitude on a sliced curve for both an acoustically hard surface and coupled shell formulation with a normalised wavenumber of $\bar{k}a = 46.15$, x - y plane.

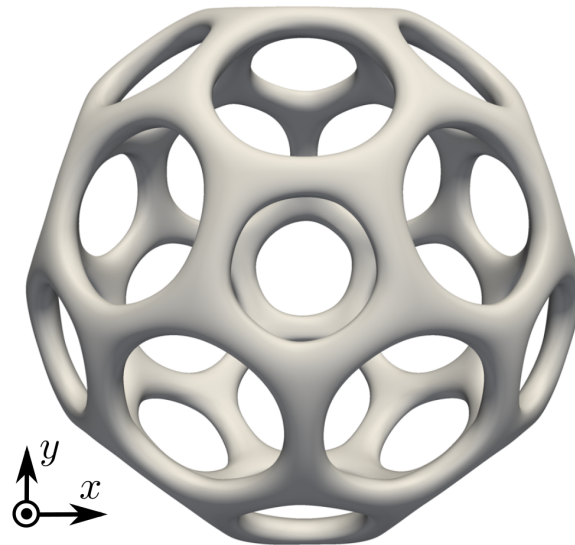
Different views of the acoustic pressure magnitude profiles for both an acoustically hard surface and elastic shell formulation are illustrated in Figures 5.20 to 5.22. Figure 5.23 shows acoustic pressure magnitude profiles on the same sliced curve for both cases. The effect on the radiated acoustic pressure caused by shell vibrations is apparent. The magnitude profile of the elastic shell shows more oscillations with a larger maximum value. The position of the maximum value is also changed from the conning tower to the bottom of the hull due to higher structural displacements. We note that this submarine model contains very thin fins. When formulating the boundary element method, the source point can be very close to the integral element, the distance between the source point and the quadrature point could be very small. This integral difficulty will become apparent if a thinner shell thickness is chosen. This method does not address this problem as it focuses on efficiently coupling the two formulations.

5.3.3 Acoustic wave scattered by a geometry with complex topology

The final example is a Loop subdivision surface with a complex topology, as shown in Figure 5.24. This topology is generally challenging for parametric boundary representing tools based on tensor product formulation (e.g., NURBS), but it is addressed without any problems using subdivision surfaces. A watertight and smooth limit surface is shown in Figure 5.24b. The same structural acoustic analysis is considered with the material properties detailed in Table 5.1 and a plane wave of unit magnitude propagating in the positive x -direction is constructed with a normalised wavenumber of $\bar{k}a = 3$.



(a) Control mesh.



(b) Limit surface.

Figure 5.24: Complex topology example: Loop subdivision discretisation with 3,940 vertices.

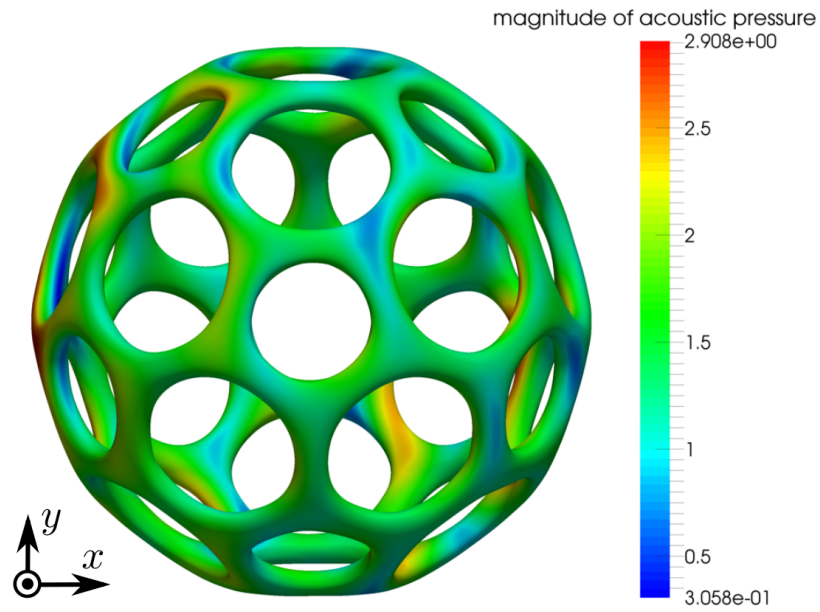
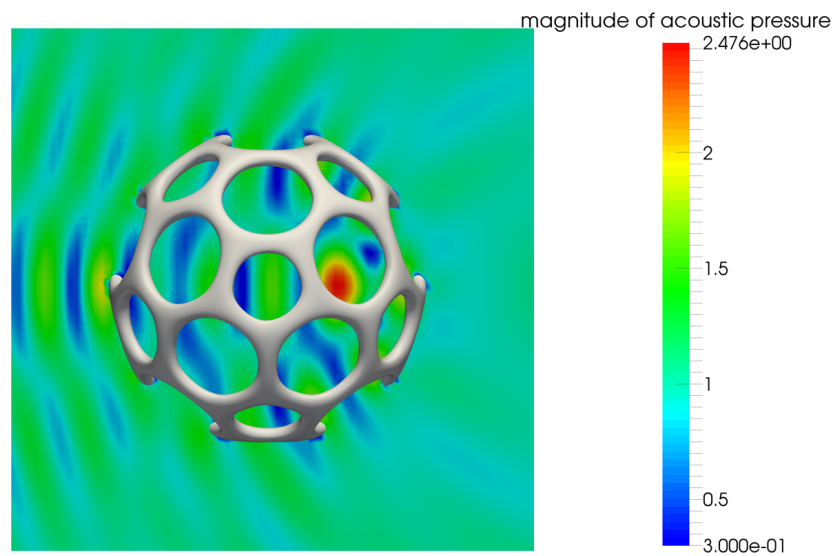
(a) $|p|$ (b) $|p|$ sampled over the x - y plane.

Figure 5.25: Coupled structural-acoustic analysis over a Loop subdivision surface with complex topology: acoustic pressure magnitudes for $\bar{k}a = 3.0$.

The magnitude of the acoustic pressure over the model surface is shown in Figure 5.25a. The magnitude changes smoothly. Plot of acoustic pressure magnitude in the outside acoustic domain are illustrated in Figure 5.25b within a x - y plane. The acoustic wave is scattered by the structure and form a localised region of high acoustic pressure in the interior of the molecule-

like model. The acoustic pressure magnitude in the exterior region stays low. With the ability to analyse complex geometry with arbitrary topology, this method can be used to optimise the microporous structures of acoustic meta-material in order to achieve cloaking.

Chapter 6

Conclusions

6.1 Summary

A novel isogeometric method for analysing underwater structures has been presented. The method adopts a Loop subdivision discretisation to formulate an acoustic boundary element method. The collocation approach is used to generate a system of equations to solve the boundary integral equations stemming from the Helmholtz equation. The method utilises a common geometry discretisation and provides the basis for fully integrated design and analysis framework. The method is verified by an example of acoustic plane scattering by an acoustically hard sphere. The results demonstrate convergence to the analytical solution. The ability of the proposed approach to analyse complex geometry is shown using the problem of a mannequin model. Two meshes with different levels of refinement both representing the same design geometry, show good agreement in the acoustic pressure profiles.

The acoustic collocation boundary element method has then been coupled to a Galerkin Kirchhoff-Love shell finite element method for coupled structural-acoustic analysis, formulated using a common Loop subdivision discretisation. The scattering of sound (acoustic waves) by the shell structure is an exterior problem where the acoustic domain is the region outside the structural domain. The incident acoustic wave induces a surface force on the boundary of the structural domain and produces displacements of the shell which are related to the acoustic velocity. By applying the acoustic pressure of the incident wave and structural force, the nodal

displacements and the acoustic pressures were solved. The implementation has been verified using the example of an elastic spherical shell scattering an acoustic plane wave. A submarine model generated with the Loop subdivision surfaces has been presented as a practical example for the acoustic scattering analysis. The final example is a complex molecule-like geometry with arbitrary topology, which highlighted the advantages of Loop subdivision surfaces to analyse complex geometries with arbitrary topologies than NURBS.

6.2 Key findings

The Loop subdivision discretisation scheme adopts a linear polygonal mesh but uses higher order basis functions which are more accurate for approximation. This gives a higher accuracy per degree of freedom over equivalent quartic Lagrangian discretisations. The Loop subdivision discretisation has advantages for analysing complex geometries with arbitrary topologies while still maintaining high continuity across elements. The ability to solve medium frequency problems using the Loop subdivision discretisation is an outstanding feature. It employs high order elements but only has the number of degrees of freedom as a linear Lagrangian discretisation. Medium frequency coupled acoustic-structural problems (normalised wavenumbers up to $ka = 80$) have been solved using the proposed method with 5.5% maximum point-wise error. Six elements per wavelength is sufficient to obtain adequate accuracy for the acoustic scattering analysis with a Loop subdivision discretisation. The coupling effect has been examined. The acoustic pressure profiles on the shell's surface are significantly different from those on acoustic rigid surfaces. Because of the shell's vibration, the acoustic pressures on the surfaces show increased oscillation. There are large acoustic pressures in the presences of large structural displacements. The implementation of hierarchical matrices to construct efficient low-rank approximations of dense matrices allows for boundary element models generated through Loop subdivision discretisations with over 10,000 vertices. The method is efficient and accurate.

6.3 Future work

Future work will extend the current implementation with Catmull-Clark subdivision surfaces. These are more standard CAD techniques, used widely in industry. A robust integration scheme will be developed for near singular integration. Simulating higher acoustic frequencies is another research direction. The partition of unity BEM (PUBEM) [145] was proposed to solve acoustic problem with high frequencies in a efficient way. It can be implemented into the present work to address high frequency structural-acoustic interactions. Another worthwhile extension is to couple the isogeometric acoustic boundary element method with a three-dimensional acoustic finite element method to simulate acoustic scattering from the fluid domain to the solid domain. This is very important in the application of acoustic imaging techniques.

Future work will also implement the present method into shape optimisation schemes to assist the industrial design of underwater structures. Practical engineering design is often a trial and error procedure. In the conventional shape optimisation process, the designer first generates an initial model for the object with a CAD software. After that, a discretisation (mesh) is generated to approximate the initial CAD model for analysis. Then, the design variables which controlling the geometry will be updated according to the analysis results of the cost functions. The CAD model is recovered for the next iteration of the optimisation process. The proposed method is a step towards developing a fully integrated design methodology. By using the same subdivision surfaces model for both design and analysis, the new workflow can eliminate costly data conversion between the CAD and the mesh. Any adjustments of the CAD will be directly adopted in analysis without the need of mesh regeneration. The optimisation process is simplified and significant gains are made in time and efficiency.

References

- [1] J. A. Cottrell, T. J. R. Hughes, and Y. Bazilevs. *Isogeometric Analysis: toward Integration of CAD and FEA*. John Wiley & Sons, 2009.
- [2] Y. Bazilevs, V. M. Calo, J. A. Cottrell, J. A. Evans, T. J. R. Hughes, S. Lipton, M. A. Scott, and T. W. Sederberg. Isogeometric analysis using T-splines. *Computer Methods in Applied Mechanics and Engineering*, 199(5–8):229–263, 2010.
- [3] A. Vuong, C. Giannelli, B. Jüttler, and B. Simeon. A hierarchical approach to adaptive local refinement in isogeometric analysis. *Computer Methods in Applied Mechanics and Engineering*, 200(49):3554–3567, 2011.
- [4] Y. Zhang, W. Wang, and T. J. R. Hughes. Solid T-spline construction from boundary representations for genus-zero geometry. *Computer Methods in Applied Mechanics and Engineering*, 249:185–197, 2012.
- [5] F. Cirak, M. Ortiz, and P. Schröder. Subdivision surfaces: a new paradigm for thin-shell finite-element analysis. *International Journal for Numerical Methods in Engineering*, 47(12):2039–2072, 2000.
- [6] J. J. Bowman, T. B. Senior, and P. L. Uslenghi. Electromagnetic and acoustic scattering by simple shapes. Technical report, Michigan University Ann Arbor Radiation Lab, 1970.
- [7] R. T. Hoctor and S. A. Kassam. The unifying role of the coarray in aperture synthesis for coherent and incoherent imaging. *Proceedings of the IEEE*, 78(4):735–752, 1990.
- [8] J. J. P. Kastelein and E. de Groot. Ultrasound imaging techniques for the evaluation of cardiovascular therapies. *European Heart Journal*, 29(7):849–858, 2008.

- [9] J. Blitz and G. Simpson. *Ultrasonic methods of non-destructive testing*, volume 2. Springer Science & Business Media, 1995.
- [10] V. M. Malhotra and N. J. Carino. *Handbook on Nondestructive Testing of Concrete Second Edition*. CRC press, 2003.
- [11] W. D. Hackmann. Sonar research and naval warfare 1914-1954: A case study of a twentieth-century establishment science. *Historical Studies in the Physical and Biological Sciences*, 16(1):83–110, 1986.
- [12] M. C. Junger and D. Feit. *Sound, Structures, and Their Interaction*, volume 225. MIT Press Cambridge, MA, 1986.
- [13] A. Sommerfeld. *Partial Differential Equations in Physics*, volume 1. Academic Press, 1949.
- [14] R. P. Shaw. Boundary integral equation methods applied to wave problems. Technical report, State university of New York at Buffulo, 1979.
- [15] R. D. Ciskowski and C. A. Brebbia. *Boundary Element Methods in Acoustics*. Springer, 1991.
- [16] M. R. Bai. Application of BEM (boundary element method)-based acoustic holography to radiation analysis of sound sources with arbitrarily shaped geometries. *The Journal of the Acoustical Society of America*, 92(1):533–549, 1992.
- [17] L. C. Wrobel. *The Boundary Element Method, Applications in Thermo-Fluids and Acoustics*, volume 1. John Wiley & Sons, 2002.
- [18] M. F. Hamilton and D. T. Blackstock. *Nonlinear acoustics*, volume 1. Academic press San Diego, 1998.
- [19] J. C. F. Telles. A self-adaptive co-ordinate transformation for efficient numerical evaluation of general boundary element integrals. *International Journal for Numerical Methods in Engineering*, 24(5):959–973, 1987.

- [20] M. G. Duffy. Quadrature over a pyramid or cube of integrands with a singularity at a vertex. *SIAM Journal on Numerical Analysis*, 19(6):1260–1262, 1982.
- [21] G. C. Everstine and F. M. Henderson. Coupled finite element/boundary element approach for fluid-structure interaction. *The Journal of the Acoustical Society of America*, 87(5):1938–1947, 1990.
- [22] M. Fischer and L. Gaul. Fast BEM-FEM mortar coupling for acoustic-structure interaction. *International Journal for Numerical Methods in Engineering*, 62(12):1677–1690, 2005.
- [23] S. Schneider. FE/FMBE coupling to model fluid-structure interaction. *International Journal for Numerical Methods in Engineering*, 76(13):2137–2156, 2008.
- [24] L. Chen, C. Zheng, and H. Chen. FEM/wideband FMBEM coupling for structural-acoustic design sensitivity analysis. *Computer Methods in Applied Mechanics and Engineering*, 276:1–19, 2014.
- [25] L. Noels and R. Radovitzky. A new discontinuous Galerkin method for Kirchhoff–Love shells. *Computer Methods in Applied Mechanics and Engineering*, 197(33-40):2901–2929, 2008.
- [26] B. Cockburn, G. E. Karniadakis, and C. Shu. The development of discontinuous Galerkin methods. In *Discontinuous Galerkin Methods*, pages 3–50. Springer, 2000.
- [27] P. Krysl and T. Belytschko. Analysis of thin shells by the element-free Galerkin method. *International Journal of Solids and Structures*, 33(20-22):3057–3080, 1996.
- [28] T. Rabczuk, P. M. A. Areias, and T. Belytschko. A meshfree thin shell method for non-linear dynamic fracture. *International Journal for Numerical Methods in Engineering*, 72(5):524–548, 2007.
- [29] T. J. R. Hughes, J. A. Cottrell, and Y. Bazilevs. Isogeometric analysis: CAD, finite elements, NURBS, exact geometry and mesh refinement. *Computer Methods in Applied Mechanics and Engineering*, 194(39):4135–4195, 2005.

- [30] J. A. Cottrell, A. Reali, Y. Bazilevs, and T. J. R. Hughes. Isogeometric analysis of structural vibrations. *Computer Methods in Applied Mechanics and Engineering*, 195(41):5257–5296, 2006.
- [31] T. W. Sederberg, J. Zheng, A. Bakenov, and A. Nasri. T-splines and T-NURCCs. In *ACM Transactions on Graphics (TOG)*, volume 22, pages 477–484. ACM, 2003.
- [32] F. Cirak and M. Ortiz. Fully C^1 -conforming subdivision elements for finite deformation thin-shell analysis. *International Journal for Numerical Methods in Engineering*, 51:813–833, 2001.
- [33] C. Loop. Smooth subdivision surfaces based on triangles. Master’s thesis, Department of Mathematics, The University of Utah, 1987.
- [34] D. Fritze, S. Marburg, and H. Hardtke. FEM-BEM-coupling and structural-acoustic sensitivity analysis for shell geometries. *Computers & Structures*, 83(2):143–154, 2005.
- [35] W. Hackbusch, B. N. Khoromskij, and R. Kriemann. Hierarchical matrices based on a weak admissibility criterion. *Computing*, 73(3):207–243, 2004.
- [36] J. Kiendl, K. U. Bletzinger, J. Linhard, and R. Wüchner. Isogeometric shell analysis with Kirchhoff–Love elements. *Computer Methods in Applied Mechanics and Engineering*, 198(49):3902–3914, 2009.
- [37] A. Buffa, G. Sangalli, and R. Vázquez. Isogeometric methods for computational electromagnetics: B-spline and T-spline discretizations. *Journal of Computational Physics*, 257:1291–1320, 2014.
- [38] A. Reali. An isogeometric analysis approach for the study of structural vibrations. *Journal of Earthquake Engineering*, 10(1):1–30, 2006.
- [39] Y. Bazilevs, V. M. Calo, T. J. R. Hughes, and Y. Zhang. Isogeometric fluid-structure interaction: theory, algorithms, and computations. *Computational Mechanics*, 43(1):3–37, 2008.

- [40] Y. D. Seo, H. J. Kim, and S. K. Youn. Isogeometric topology optimization using trimmed spline surfaces. *Computer Methods in Applied Mechanics and Engineering*, 199(49):3270–3296, 2010.
- [41] A. I. Ginnis, K. V. Kostas, C. Feurer, K. A. Belibassakis, T. P. Gerostathis, C. G. Politis, and P.D. Kaklis. A CATIA® ship-parametric model for isogeometric hull optimization with respect to wave resistance. In *ICCAS 2011 Trieste 20-22 September proceedings, Italy*, 2011.
- [42] K. Li and X. Qian. Isogeometric analysis and shape optimization via boundary integral. *Computer Aided Design*, 43(11):1427–1437, 2011.
- [43] M. J. Borden, M. A. Scott, J. A. Evans, and T. J. R. Hughes. Isogeometric finite element data structures based on Bézier extraction of NURBS. *International Journal for Numerical Methods in Engineering*, 87(1-5):15–47, 2011.
- [44] D. R. Forsey and R. H. Bartels. Hierarchical B-spline refinement. *ACM Siggraph Computer Graphics*, 22(4):205–212, 1988.
- [45] J. Deng, F. Chen, X. Li, C. Hu, W. Tong, Z. Yang, and Y. Feng. Polynomial splines over hierarchical T-meshes. *Graphical models*, 70(4):76–86, 2008.
- [46] N. Nguyen-Thanh, J. Kiendl, H. Nguyen-Xuan, R. Wüchner, K. U. Bletzinger, Y. Bazilevs, and T. Rabczuk. Rotation free isogeometric thin shell analysis using PHT-splines. *Computer Methods in Applied Mechanics and Engineering*, 200(47):3410–3424, 2011.
- [47] T. Dokken, T. Lyche, and K. F. Pettersen. Polynomial splines over locally refined box-partitions. *Computer Aided Geometric Design*, 30(3):331–356, 2013.
- [48] K. A. Johannessen, T. Kvamsdal, and T. Dokken. Isogeometric analysis using LR B-splines. *Computer Methods in Applied Mechanics and Engineering*, 269:471–514, 2014.

- [49] M. Aigner, C. Heinrich, B. Jüttler, E. Pilgerstorfer, B. Simeon, and A. V. Vuong. Swept volume parameterization for isogeometric analysis. In *IMA Conference on the Mathematics of Surfaces*, pages 19–44. Springer, 2009.
- [50] J. M. Escobar, J. M. Cascón, E. Rodríguez, and R. Montenegro. A new approach to solid modeling with trivariate T-splines based on mesh optimization. *Computer Methods in Applied Mechanics and Engineering*, 200(45):3210–3222, 2011.
- [51] G. Xu, B. Mourrain, R. Duvigneau, and A. Galligo. Parameterization of computational domain in isogeometric analysis: methods and comparison. *Computer Methods in Applied Mechanics and Engineering*, 200(23):2021–2031, 2011.
- [52] W. Dornisch, G. Vitucci, and S. Klinkel. The weak substitution method—an application of the mortar method for patch coupling in NURBS-based isogeometric analysis. *International Journal for Numerical Methods in Engineering*, 103(3):205–234, 2015.
- [53] Z. Lei, F. Gillot, and L. Jezequel. A C_0/G_1 multiple patches connection method in isogeometric analysis. *Applied Mathematical Modelling*, 39(15):4405 – 4420, 2015.
- [54] M. Breitenberger, A. Apostolatos, B. Philipp, R. Wüchner, and K. U. Bletzinger. Analysis in computer aided design: Nonlinear isogeometric b-rep analysis of shell structures. *Computer Methods in Applied Mechanics and Engineering*, 284(Supplement C):401 – 457, 2015. Isogeometric Analysis Special Issue.
- [55] X. Du, G. Zhao, and W. Wang. Nitsche method for isogeometric analysis of Reissner–Mindlin plate with non-conforming multi-patches. *Computer Aided Geometric Design*, 35-36(Supplement C):121 – 136, 2015. Geometric Modeling and Processing 2015.
- [56] L. Coox, F. Greco, O. Atak, D. Vandepitte, and W. Desmet. A robust patch coupling method for NURBS-based isogeometric analysis of non-conforming multipatch surfaces. *Computer Methods in Applied Mechanics and Engineering*, 316:235–260, 2017.
- [57] M. Ruess, D. Schillinger, A. I. Ozcan, and E. Rank. Weak coupling for isogeometric

- analysis of non-matching and trimmed multi-patch geometries. *Computer Methods in Applied Mechanics and Engineering*, 269(Supplement C):46 – 71, 2014.
- [58] J. A. Cottrell, T. J. R. Hughes, and A. Reali. Studies of refinement and continuity in isogeometric structural analysis. *Computer Methods in Applied Mechanics and Engineering*, 196(41):4160 – 4183, 2007.
- [59] J. Kiendl, Y. Bazilevs, M. C. Hsu, R. Wüchner, and K. U. Bletzinger. The bending strip method for isogeometric analysis of Kirchhoff–Love shell structures comprised of multiple patches. *Computer Methods in Applied Mechanics and Engineering*, 199(37):2403 – 2416, 2010.
- [60] R. Schmidt, R. Wüchner, and K. U. Bletzinger. Isogeometric analysis of trimmed nurbs geometries. *Computer Methods in Applied Mechanics and Engineering*, 241:93–111, 2012.
- [61] H. J. Kim, Y. D. Seo, and S. K. Youn. Isogeometric analysis for trimmed CAD surfaces. *Computer Methods in Applied Mechanics and Engineering*, 198(37):2982–2995, 2009.
- [62] H. J. Kim, Y. D. Seo, and S. K. Youn. Isogeometric analysis with trimming technique for problems of arbitrary complex topology. *Computer Methods in Applied Mechanics and Engineering*, 199(45):2796–2812, 2010.
- [63] G. Beer, B. Marussig, and J. Zechner. A simple approach to the numerical simulation with trimmed CAD surfaces. *Computer Methods in Applied Mechanics and Engineering*, 285:776–790, 2015.
- [64] D. Schillinger, L. Dede, M. A. Scott, J. A. Evans, M. J. Borden, E. Rank, and T. J. R. Hughes. An isogeometric design-through-analysis methodology based on adaptive hierarchical refinement of NURBS, immersed boundary methods, and T-spline CAD surfaces. *Computer Methods in Applied Mechanics and Engineering*, 249:116–150, 2012.
- [65] C. Giannelli, B. Jüttler, and H. Speleers. THB-splines: The truncated basis for hierarchical splines. *Computer Aided Geometric Design*, 29(7):485–498, 2012.

- [66] D. Zorin and P. Schröder. Subdivision for modeling and animation. SIGGRAPH 2000 Course Notes, 2000.
- [67] J. Peters and U. Reif. *Subdivision Surfaces*. Springer Series in Geometry and Computing. Springer, 2008.
- [68] A. Czaja, A. Grabowska, T. Kocejko, and E. Kozłowska. Introduction to Autodesk Fusion 360.
- [69] PTC Creo 5.0. URL <https://www.ptc.com/en/products/cad/creo>, 2018.
- [70] CATiA V6. URL <http://www.3ds.com/products-services/catia>, 2013.
- [71] K. Bandara, F. Cirak, G. Of, O. Steinbach, and J. Zapletal. Boundary element based multiresolution shape optimisation in electrostatics. *Journal of Computational Physics*, 297:584–598, 2015.
- [72] F. Cirak and Q. Long. Subdivision shells with exact boundary control and non-manifold geometry. *International Journal for Numerical Methods in Engineering*, 88(9):897–923, 2011.
- [73] Q. Long, P. B. Bornemann, and F. Cirak. Shear-flexible subdivision shells. *International Journal for Numerical Methods in Engineering*, 90:1549–1577, 2012.
- [74] J. Hua, Y. He, and H. Qin. Multiresolution heterogeneous solid modeling and visualization using trivariate simplex splines. In *Proceedings of the Ninth ACM Symposium on Solid Modeling and Applications*, pages 47–58. Eurographics Association, 2004.
- [75] X. Li, X. Guo, H. Wang, Y. He, X. Gu, and H. Qin. Harmonic volumetric mapping for solid modeling applications. In *Proceedings of the 2007 ACM Symposium on Solid and Physical Modeling*, pages 109–120. ACM, 2007.
- [76] T. Martin, E. Cohen, and M. Kirby. Volumetric parameterization and trivariate B-spline fitting using harmonic functions. In *Proceedings of the 2008 ACM Symposium on Solid and Physical Modeling*, pages 269–280. ACM, 2008.

- [77] W. Wang, Y. Zhang, L. Liu, and T. J. R. Hughes. Trivariate solid T-spline construction from boundary triangulations with arbitrary genus topology. *Computer-Aided Design*, 45(2):351–360, 2013.
- [78] Y. Zhang, W. Wang, and T. J. R. Hughes. Conformal solid T-spline construction from boundary T-spline representations. *Computational Mechanics*, pages 1–9, 2013.
- [79] D. J. Benson, Y. Bazilevs, M. C. Hsu, and T. J. R. Hughes. Isogeometric shell analysis: the Reissner–Mindlin shell. *Computer Methods in Applied Mechanics and Engineering*, 199(5):276–289, 2010.
- [80] D. J. Benson, Y. Bazilevs, M. C. Hsu, and T. J. R. Hughes. A large deformation, rotation-free, isogeometric shell. *Computer Methods in Applied Mechanics and Engineering*, 200(13):1367–1378, 2011.
- [81] T. K. Uhm and S. K. Youn. T-spline finite element method for the analysis of shell structures. *International Journal for Numerical Methods in Engineering*, 80(4):507–536, 2009.
- [82] N. Nguyen-Thanh, H. Nguyen-Xuan, S. P. A. Bordas, and T. Rabczuk. Isogeometric analysis using polynomial splines over hierarchical T-meshes for two-dimensional elastic solids. *Computer Methods in Applied Mechanics and Engineering*, 200(21):1892–1908, 2011.
- [83] R. N. Simpson, S. P. A. Bordas, J. Trevelyan, and T. Rabczuk. A two-dimensional isogeometric boundary element method for elastostatic analysis. *Computer Methods in Applied Mechanics and Engineering*, 209-212:87–100, 2012.
- [84] T. Takahashi and T. Matsumoto. An application of fast multipole method to isogeometric boundary element method for laplace equation in two dimensions. *Engineering Analysis with Boundary Elements*, 36(12):1766–1775, 2012.
- [85] M. A. Scott, R. N. Simpson, J. A. Evans, S. Lipton, S. P. A. Bordas, T. J. R. Hughes, and

- T. W. Sederberg. Isogeometric boundary element analysis using unstructured T-splines. *Computer Methods in Applied Mechanics and Engineering*, 254:197–221, 2013.
- [86] M. J. Peake, J. Trevelyan, and G. Coates. Extended isogeometric boundary element method (XIBEM) for two-dimensional Helmholtz problems. *Computer Methods in Applied Mechanics and Engineering*, 259:93–102, 2013.
- [87] R. N. Simpson, M. A. Scott, M. Taus, D. C. Thomas, and H. Lian. Acoustic isogeometric boundary element analysis. *Computer Methods in Applied Mechanics and Engineering*, 269:265–290, 2014.
- [88] L. Heltai, J. Kiendl, A. DeSimone, and A. Reali. A natural framework for isogeometric fluid-structure interaction based on BEM-shell coupling. *Computer Methods in Applied Mechanics and Engineering*, 316:522–546, 2017.
- [89] A. J. Burton and G. F. Miller. The application of integral equation methods to the numerical solution of some exterior boundary-value problems. *Proceedings of the Royal Society: A*, 323:201–210, 1971.
- [90] Y. Liu. *Fast Multipole Boundary Element Method: Theory and Applications in Engineering*. Cambridge University Press, 2009.
- [91] M. Bebendorf. *Hierarchical Matrices*. Springer, 2008.
- [92] A. Brancati, M. H. Aliabadi, and I. Benedetti. Hierarchical adaptive cross approximation GMRES technique for solution of acoustic problems using the boundary element method. *Computer Modelling in Engineering and Sciences*, 43(2):149–172, 2009.
- [93] M. G. Cox. The numerical evaluation of B-splines. *IMA Journal of Applied Mathematics*, 10(2):134–149, 1972.
- [94] C. De Boor. On calculating with B-splines. *Journal of Approximation theory*, 6(1):50–62, 1972.

- [95] R. F. Riesenfeld. On Chaikin's algorithm. *Computer Graphics and Image Processing*, 4(3):304–310, 1975.
- [96] E. Catmull and J. Clark. Recursively generated B-spline surfaces on arbitrary topological meshes. *Computer-Aided Design*, 10(6):350–355, 1978.
- [97] R. Qu. *Recursive subdivision algorithms for curve and surface design*. PhD thesis, Brunel University, School of Information Systems, Computing and Mathematics, 1990.
- [98] D. Doo and M. Sabin. A subdivision algorithm for smoothing down irregularly shaped polyhedrons. In *Proceedings on interactive techniques in computer aided design*, volume 157, page 165. Bologna, 1978.
- [99] J. Peters and U. Reif. *Subdivision Surfaces*, volume 3. Springer Science & Business Media, 2008.
- [100] J. Warren and H. Weimer. *Subdivision Methods for Geometric Design: A Constructive Approach*. Morgan Kaufmann, 2001.
- [101] J. Stam. Exact evaluation of Loop subdivision surfaces at arbitrary parameter values. *SIGGRAPH Course Note*, pages 111–124, 1998.
- [102] M. Lai. Fortran subroutines for b-nets of box splines on three-and four-directional meshes. *Numerical Algorithms*, 2(1):33–38, 1992.
- [103] I. Fredholm. Sur une classe d'équations fonctionnelles. *Acta Mathematica*, 27:365–390, 1903.
- [104] C. Massonnet. Solution générale du problème aux tensions de l'élasticité tridimensionnelle. *9th International Congress in Applied Mechanics*, 1956.
- [105] M. A. Jaswon. Integral equation methods in potential theory. I. In *Proceedings of the Royal Society of London A: Mathematical, Physical and Engineering Sciences*, volume 275, pages 23–32. The Royal Society, 1963.

- [106] G. T. Symm. Integral equation methods in potential theory. II. In *Proceedings of the Royal Society of London A: Mathematical, Physical and Engineering Sciences*, volume 275, pages 33–46. The Royal Society, 1963.
- [107] J. C. Lachat and J. O. Watson. Effective numerical treatment of boundary integral equations: a formulation for three-dimensional elastostatics. *International Journal for Numerical Methods in Engineering*, 10(5):991–1005, 1976.
- [108] C. A. Brebbia. *The Boundary Elements Method for Engineers*. Pentech Press, 1978.
- [109] G. E. Blandford, A. R. Ingraffea, and J. A. Liggett. Two-dimensional stress intensity factor computations using the boundary element method. *International Journal for Numerical Methods in Engineering*, 17(3):387–404, 1981.
- [110] Y. Mi and M. H. Aliabadi. Dual boundary element method for three-dimensional fracture mechanics analysis. *Engineering Analysis with Boundary Elements*, 10(2):161–171, 1992.
- [111] M. H. Aliabadi. Boundary element formulations in fracture mechanics. *Applied Mechanics Reviews*, 50(2):83–96, 1997.
- [112] P. K. Banerjee and R. Butterfield. *Boundary Element Methods in Engineering Science*, volume 17. McGraw-Hill London, 1981.
- [113] S. Sirtori, G. Maier, G. Novati, and S. Miccoli. A Galerkin symmetric boundary-element method in elasticity: formulation and implementation. *International Journal for Numerical Methods in Engineering*, 35(2):255–282, 1992.
- [114] N. Ghosh, H. Rajiyah, S. Ghosh, and S. Mukherjee. A new boundary element method formulation for linear elasticity. *Journal of Applied Mechanics*, 53(1):69–76, 1986.
- [115] M. H. Aliabadi. *The Boundary Element Method, Applications in Solids and Structure*, volume 2. John Wiley & Sons, 2002.

- [116] S. Kagami and I. Fukai. Application of boundary element method to electromagnetic field problems (short papers). *Microwave Theory and Techniques, IEEE Transactions on*, 32(4):455–461, 1984.
- [117] R. Djellouli, C. Farhat, A. Macedo, and R. Tezaur. Finite element solution of two-dimensional acoustic scattering problems using arbitrarily shaped convex artificial boundaries. *Journal of Computational Acoustics*, 8(01):81–99, 2000.
- [118] F. Ihlenburg. *Finite Element Analysis of Acoustic Scattering*, volume 132. Springer Science & Business Media, 2006.
- [119] D. Schillinger, J. A. Evans, A. Reali, M. A. Scott, and T. J. R. Hughes. Isogeometric collocation: Cost comparison with Galerkin methods and extension to adaptive hierarchical NURBS discretizations. *Computer Methods in Applied Mechanics and Engineering*, 267:170–232, 2013.
- [120] L. Greengard and V. Rokhlin. A fast algorithm for particle simulations. *Journal of computational physics*, 73(2):325–348, 1987.
- [121] J. Carrier, L. Greengard, and V. Rokhlin. A fast adaptive multipole algorithm for particle simulations. *SIAM Journal of Scientific and Statistical Computing*, 9(4):669–686, 1988.
- [122] H. Cheng, L. Greengard, and V. Rokhlin. A fast adaptive multipole algorithm in three dimensions. *Journal of Computational Physics*, 155:468–498, 1999.
- [123] W. Hackbusch. A sparse matrix arithmetic based on H-matrices. Part I: Introduction to H-matrices. *Computing*, 62(2):89–108, 1999.
- [124] W. Hackbusch and B. N. Khoromskij. A sparse H-matrix arithmetic. *Computing*, 64(1):21–47, 2000.
- [125] R. Kriemann. HLIBpro user manual. *Max-Planck-Institute for Mathematics in the Sciences, Leipzig*, 2008.

- [126] L. G. Copley. Integral equation method for radiation from vibrating bodies. *The journal of the acoustical society of America*, 41(4A):807–816, 1967.
- [127] A. J. Burton and G. F. Miller. The application of integral equation methods to the numerical solution of some exterior boundary-value problems. In *Proceedings of the Royal Society of London A: Mathematical, Physical and Engineering Sciences*, volume 323, pages 201–210. The Royal Society, 1971.
- [128] M. Guiggiani and A. Gigante. A general algorithm for multidimensional cauchy principal value integrals in the boundary element method. *Journal of Applied Mechanics*, 57(4):906–915, 1990.
- [129] Y. Liu and T. J. Rudolphi. Some identities for fundamental-solutions and their applications to weakly-singular boundary element formulations. *Engineering Analysis with Boundary Elements*, 8(6):301–311, 1991.
- [130] Y. Liu and F. J. Rizzo. A weakly singular form of the hypersingular boundary integral equation applied to 3-D acoustic wave problems. *Computer Methods in Applied Mechanics and Engineering*, 96(2):271–287, 1992.
- [131] V. Sladek, J. Sladek, and M. Tanaka. Regularization of hypersingular and nearly singular integrals in the potential theory and elasticity. *International Journal for Numerical Methods in Engineering*, 36(10):1609–1628, 1993.
- [132] A. F. Seybert, B. Soenarko, F. J. Rizzo, and D. J. Shippy. An advanced computational method for radiation and scattering of acoustic waves in three dimensions. *The journal of the acoustical society of America*, 77(2):362–368, 1985.
- [133] P. Geng, J. T. Oden, and L. Demkowicz. Numerical solution and a posteriori error estimation of exterior acoustics problems by a boundary element method at high wave numbers. *The Journal of the Acoustical Society of America*, 100(1):335–345, 1996.
- [134] C. Geuzaine and J. Remacle. Gmsh: A 3-D finite element mesh generator with build-

- in pre- and post-processing facilities. *International Journal for Numerical Methods in Engineering*, 79(11):1309–1331, 2009.
- [135] B. F. G. Katz. Boundary element method calculation of individual head-related transfer function. I. rigid model calculation. *The Journal of the Acoustical Society of America*, 110(5):2440–2448, 2001.
- [136] Z. Liu, M. Majeed, F. Cirak, and R. N. Simpson. Isogeometric FEM-BEM coupled structural-acoustic analysis of shells using subdivision surfaces. *International Journal for Numerical Methods in Engineering*, 113(9):1507–1530, 2018.
- [137] R. Courant. Variational methods for the solution of problems of equilibrium and vibrations. *Lecture Notes in Pure and Applied Mathematics*, pages 1–1, 1994.
- [138] J. C. Simo and D. D. Fox. On a stress resultant geometrically exact shell model. Part I: Formulation and optimal parametrization. *Computer Methods in Applied Mechanics and Engineering*, 72(3):267–304, 1989.
- [139] J. C. Simo, D. D. Fox, and M. S. Rifai. On a stress resultant geometrically exact shell model. Part II: The linear theory; computational aspects. *Computer Methods in Applied Mechanics and Engineering*, 73(1):53–92, 1989.
- [140] J. C. Simo, D. D. Fox, and M. S. Rifai. On a stress resultant geometrically exact shell model. Part III: Computational aspects of the nonlinear theory. *Computer Methods in Applied Mechanics and Engineering*, 79(1):21–70, 1990.
- [141] J. C. Simo, M. S. Rifai, and D. D. Fox. On a stress resultant geometrically exact shell model. Part IV: Variable thickness shells with through-the-thickness stretching. *Computer methods in applied mechanics and engineering*, 81(1):91–126, 1990.
- [142] P. G. Ciarlet. *An Introduction to Differential Geometry with Applications to Elasticity*. Springer, 2005.
- [143] J. D. Scargle. Studies in astronomical time series analysis. ii-statistical aspects of spectral analysis of unevenly spaced data. *The Astrophysical Journal*, 263:835–853, 1982.

- [144] J. Li, Z. S. Khodaei, and M. H. Aliabadi. Spectral bem for the analysis of wave propagation and fracture mechanics. *Journal of Multiscale Modelling*, 8(03n04):1740007, 2017.
- [145] P. Emmanuel, J. Trevelyan, and P. Bettess. Wave boundary elements: a theoretical overview presenting applications in scattering of short waves. *Engineering Analysis with Boundary Elements*, 28(2):131–141, 2004.
- [146] S. Marburg. Six boundary elements per wavelength: is that enough? *Journal of Computational Acoustics*, 10(01):25–51, 2002.